Measurement of the transverse momentum distribution of Z bosons in proton-proton collisions at $\sqrt{s} = 7\,\text{TeV}$ using the ATLAS detector

Dissertation
zur
Erlangung des Doktorgrades (Dr. rer. nat.)
der
Mathematisch-Naturwissenschaftlichen Fakultät
der
Rheinischen Friedrich-Wilhelms-Universität Bonn

von
Karl Klemens Müller
aus
Potsdam

Bonn, June 2013

Dieser Forschungsbericht wurde als Dissertation von der
Mathematisch-Naturwissenschaftlichen Fakultät der Universität Bonn angenommen und ist
auf dem Hochschulschriftenserver der ULB Bonn
`http://hss.ulb.uni-bonn.de/diss_online` elektronisch publiziert.

1. Gutachter:	Prof. Dr. Norbert Wermes
2. Gutachter:	Prof. Dr. Ian C. Brock
Tag der Promotion:	15.07.2013
Erscheinungsjahr:	2013

Contents

Chapter 1

Introduction

The current understanding of matter at the fundamental level, that is of the elementary particles and their interactions, is based on the Standard Model of particle physics (SM) which has its origins in the 1960s and 70s and has since been experimentally tested and verified. The SM has been very successful in describing experimental data and has correctly predicted the existence of several particles, like the gluon, the charm quark, the W and Z bosons and the top quark. The recent discovery of a boson consistent with the Standard Model Higgs boson completes the boson content of the SM. However, some important questions in physics are not answered by the Standard Model. What is the nature of dark matter and dark energy? What is the explanation for the so called hierarchy problem, which has to with the huge difference in fundamental mass scale of gravity and the electroweak interaction leading to a serious fine tuning problem? These questions have inspired various theoretical extensions of the SM, most prominent among them Super Symmetry which predicts many new particles with masses in the TeV range.

The historical progress in particle physics was achieved mainly through the study of high energy particle collisions using accelerators. The Large Hadron Collider, the most powerful accelerator to date, was built to discover and study the Higgs boson, to explore possible extensions to the SM which predict new particles at the TeV scale, and to perform precision measurements of Standard Model processes. A Higgs-like particle has been discovered by the two large experiments at the LHC, ATLAS and CMS, but no other signs for physics beyond the SM have been found so far.

At the LHC, W and Z bosons are produced with high rates. Since their properties are well established, precision measurements allow comparisons with the theory, in particular with higher order perturbative predictions of the cross sections. Differential cross section measurements provide a more complete understanding not only of the final state, but also of the production dynamics, including non-perturbative effects, and allow to constrain the parton distribution functions of the proton, which are needed to predict the production rates at the LHC. A strong test of the consistency of the SM will be possible from a precise measurement of the W mass combined with other electroweak measurements as well as the Higgs boson mass.

In this thesis, the Z boson transverse momentum distribution is measured with the Z bosons decaying into muon pairs. Apart from testing higher order QCD predictions, the precise theoretical modelling of differential boson cross sections is an important requirement for the Higgs measurements, as well as the W mass measurement at the LHC. Initially, the measurement was performed with data taken in 2010 corresponding to an integrated luminosity of $40\,\mathrm{pb}^{-1}$. Contributions from this thesis went into a first measurement of the transverse momentum distribution of Z bosons by the ATLAS collaboration, published in Ref. [1]. The measurement is finalised in this thesis using the full 2011 data set corresponding to an integrated luminosity of $4.7\,\mathrm{fb}^{-1}$. The results presented provide a more stringent test of QCD predictions compared to [1] because the transverse momentum distribution is sampled in finer bins - with smaller statistical and systematic uncertainties, where the improvements on the systematic uncertainty are due to the use of more advanced unfolding methods and improved measurements of the muon efficiency. The measurement reaches up to a transverse momentum of the produced Z boson of 800 GeV and has an expected precision of $< 1\%$ for $p_{\mathrm{T}} < 150\,\mathrm{GeV}$. Furthermore, the measurement range is extended to the differential cross section both as a function of the Z bosons transverse momentum and its rapidity y.

This thesis is organised as follows. Chapter 2 gives a brief introduction to the Standard Model and an overview of predictions for Z boson production. The experimental setup at the Large Hadron Collider and the ATLAS experiment are described in Chapter 3. This is followed by a description of the event reconstruction algorithms concentrating on the muon reconstruction in Chapter 4. The next chapters describe in detail all steps towards the cross section measurement. First, the selection of a Z boson sample in data and simulation is presented in Chapter 5. Next, Chapter 6 describes the extraction of the differential cross section. The systematic uncertainties are discussed in Chapter 7 and Chapter 8 summarises the results. Conclusions of this work are presented in Chapter 9.

Chapter 2

Theoretical background

The topic of this thesis is the production of Z bosons in proton-proton collisions at the LHC. The general framework for describing the physics of elementary particle interactions is given by the Standard Model of particle physics (SM) of which a very brief summary is given here. The second part of this chapter deals with the aspects of the SM that are relevant to describe proton-proton collisions, the proton structure, Z production, as well as the most important predictions for the transverse momentum distribution of Z bosons.

2.1 The Standard Model

The Standard Model describes the elementary particles and their interaction via the strong, electromagnetic and weak interactions. There are two categories of fundamental particles: fermions (spin 1/2), which make up all visible matter of the universe, and bosons (integer spin) which act as the force carriers. The particles and their properties are summarised in Figure 2.1.

The fermions come in two groups, quarks and leptons. There are six types of leptons and 6 flavours of quarks, that can be arranged in 3 generations. In addition each quark and lepton has its antiparticle. Each lepton generation consists of a charged lepton, the electron, e, the muon, μ, or the tau, τ, and a neutral lepton called neutrino, ν_e, ν_μ, ν_τ. The neutrinos interact only via the weak force, while e, μ and τ interact via the weak and electromagnetic forces. The quark generations are made up from u, d, c, s, t and b with fractional charges -1/3 and 2/3. Quarks also interact via the weak and electromagnetic forces. In addition, they carry colour charge and interact via the strong force. In contrast to leptons, which exist as free particles, quarks can only be observed in bound states, called hadrons. Hadrons contain either a quark and an antiquark (mesons), or three quarks (baryons), and carry no net colour charge. In addition to these so-called valence quarks, which define the quantum numbers of the hadron, part of a hadron's momentum is carried by virtual quark-antiquark pairs, called sea quarks, and gluons. In so called hard inelastic collisions the interaction of all partons (valence and sea quarks, gluons) occur.

The interactions between the particles are mediated by the exchange of gauge bosons with spin 1. The electromagnetic force is mediated by the massless photon, γ. The weak force is mediated by the massive weak bosons $W^\pm$ and Z. The strong force is mediated by the gluon, g, which is also massless.

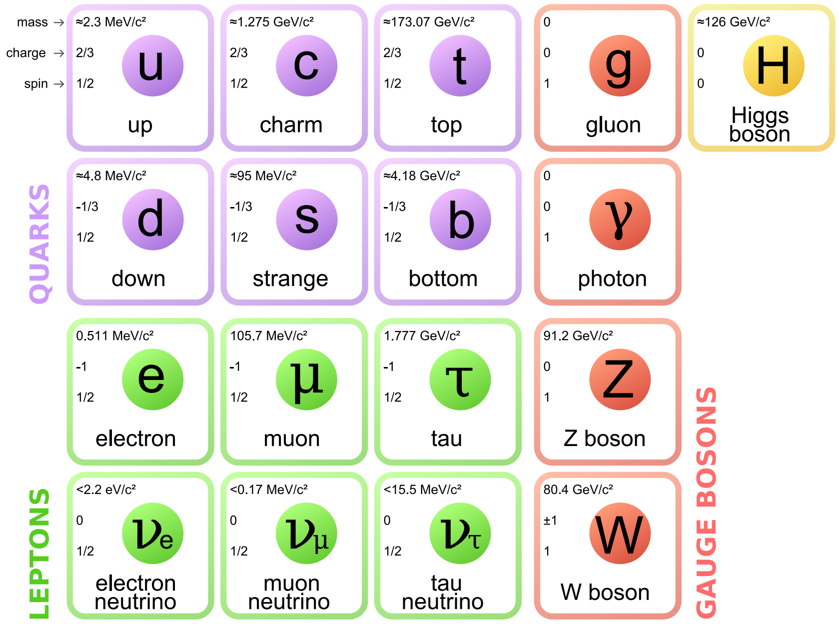

Figure 2.1: The fundamental particles of the Standard Model [2].

The Standard Model is formulated as a relativistic quantum field theory where the interactions follow from local gauge invariance. The gauge group governing the SM of strong and electroweak interactions is

$$G = SU(3) \times SU(2) \times U(1).$$

The strong interaction is described by the $SU(3)$ part of this group structure by a theory called Quantum Chromodynamics (QCD). Its gauge bosons, the gluons, carry colour charge, and couple to quarks and to themselves. This leads to the confinement property of QCD, that all colour charged objects are found in colour singlet bound objects. Thus quarks and gluons can not be observed as free particles. The electromagnetic and weak interactions are unified in the gauge group $SU(2)_L \times U(1)_Y$. The electromagnetic interaction is contained in this group and is described by the Abelian gauge theory Quantum Electrodynamics (QED). The gauge bosons $W^{\pm}$, Z of the electroweak gauge group have self-couplings, while the photon does not couple to itself.

In the basic electroweak model all gauge bosons are required to be massless. Since the weak bosons are observed to have a mass, the electroweak symmetry must be broken. This happens through the introduction of an additional scalar field with non-zero vacuum expectation value [3–6]. The Higgs mechanism predicts the existence of at least one additional boson with spin 0, while the mass of this so-called Higgs boson is not predicted. Direct searches at LEP could establish a lower bound of 114.4 GeV on its mass at 95% confidence level (CL) [7]. An indirect upper limit on m_H of 158 GeV at 95% CL was set by global fits to electroweak precision measurements [8]. In the mass region around 125 GeV, the Higgs boson has prominent decays into $\gamma\gamma$ and ZZ (with subsequent decay of each Z

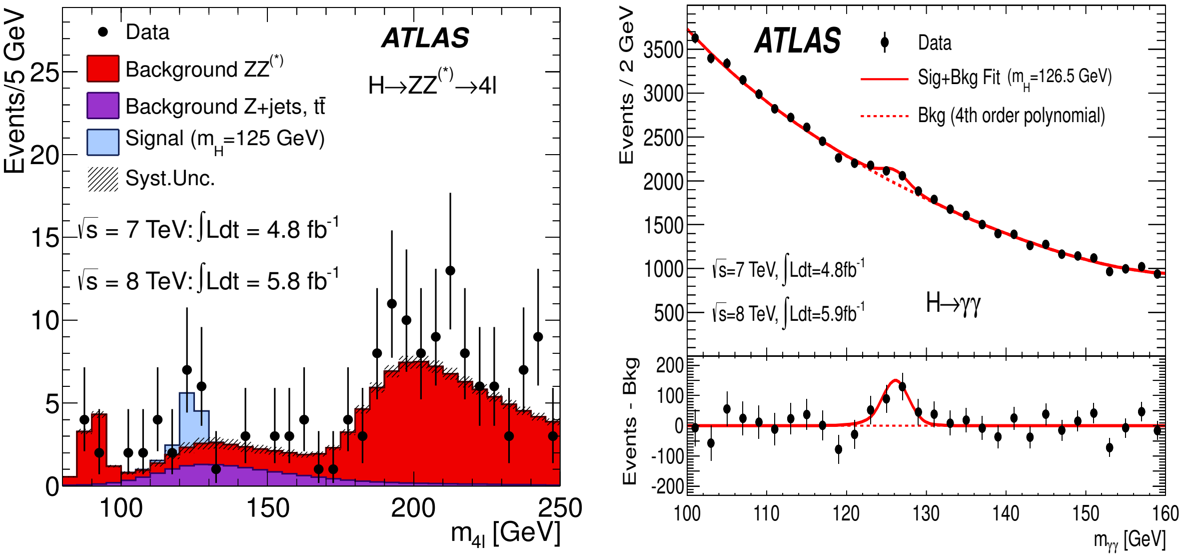

(a) (b)

Figure 2.2: Invariant mass distributions of the search for the Standard Model Higgs boson from the combination of the ATLAS data at $\sqrt{s} = 7\,\text{TeV}$ and $\sqrt{s} = 8\,\text{TeV}$. a) Distribution of the four-lepton invariant mass for the selected candidates compared to the background expectation in the 80 to 250 GeV mass range and the signal expectation for a SM Higgs with $m_H = 125\,\text{GeV}$. b) Distribution of the invariant mass of diphoton candidates after all selections. The result of a fit to the data of the sum of a signal component fixed to $m_H = 126.5\,\text{GeV}$ and a background component described by a fourth-order Bernstein polynomial is superimposed. The residuals of the data with respect to the fitted background component are displayed in the lower plot. [9]

into 2 leptons), where it appears as a localised excess in the invariant mass distributions of the decay products. The ATLAS and CMS collaborations have first observed a new particle with a mass of about 126 GeV in the decays into $\gamma\gamma$ and ZZ in data collected in 2011 and 2012 at the LHC [9, 10]. The $\gamma\gamma$ and 4-lepton invariant mass distributions of the ATLAS searches are shown in Fig. 2.2, together with the distributions of the expected background and the expected Higgs signal. From current observations the new particle is consistent with a SM Higgs boson. It has been observed with about the expected signal strength in the decay channels into $\gamma\gamma$, ZZ and WW. Measurements in the fermion decay channels, $b\bar{b}$ and $\tau\tau$ are not yet sensitive enough to make an observation, but are consistent with the Standard Model Higgs prediction [11, 12]. The measured signal strength for the different decay channels is shown in Fig. 2.3. Regarding the properties other than the mass, so far it is known to be a neutral particle and the spin 1 hypothesis is ruled out, according to the Landau-Yang theorem which states that a spin 1 particle can not decay into 2 photons [13, 14]. More precise measurements of the coupling strength to fermions, as well as its spin and parity, are needed to determine if the found particle is identical to the SM Higgs boson.

Assuming that the Higgs boson has been found in [9, 10], the Standard Model is now complete. However, it is likely not a complete theory of particle physics, as it provides no candidate for dark matter and gives no explanation for the accelerated expansion of the

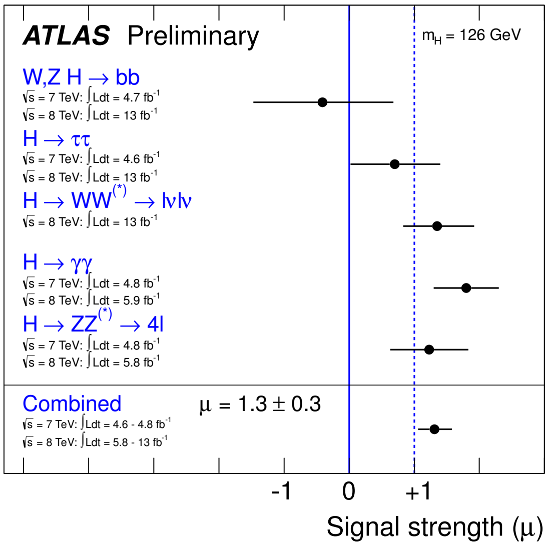

Figure 2.3: Measurements of the signal strength parameter μ for $m_H = 126\,\text{GeV}$ for the Higgs decay channels studied by ATLAS and their combination [11].

universe (dark energy) among other issues. Extensions to the SM that offer explanations for these problems mostly predict a range of new particles at energies accessible by the LHC. Direct searches for these particles have not found anything beyond SM expectations. At the same time, any new theories are constrained by precision measurements of the SM parameters. The precision of many measurements and corresponding theoretical predictions inside the Standard Model can still be improved, at the LHC for example with measurements involving top quarks and $W^{\pm}$, Z bosons.

2.2 QCD and Z production at hadron colliders

In proton-proton collisions at hadron colliders, like the LHC, quantum chromodynamics (QCD) forms the basis of the underlying physics. Due to the large value of strong coupling compared with the electroweak couplings, all processes are dominated by QCD effects. The most important aspects of QCD regarding high energy pp collisions are described in the following. The description is based on [15, 16].

2.2.1 Running of the strong coupling constant

One fundamental property of QCD is the running of the strong coupling, that is the fact that the coupling strength of QCD decreases as quarks and gluons come closer together. At the lowest order approximation, the running of the strong coupling constant α_S with a momentum transfer scale q^2 of the interaction is

$$\alpha_S(|q^2|) = \frac{12\pi}{(11n - 2f)\ln(|q^2|/\Lambda^2_{QCD})} \qquad (|q^2| \gg \Lambda^2_{QCD})), \tag{2.1}$$

where $n = 3$ is the number colours, $f = 6$ is the number of quark flavours, and $\Lambda_{QCD} \sim 100\,\mathrm{MeV}$ is the QCD scale [17]. The numerical value of the strong coupling changes from 0.119 at $q^2 = M_Z^2$ to values larger than 1 as $q^2 \to \Lambda^2_{QCD}$. According to the size of the coupling constant at the relevant energy scale, collision processes in QCD are grouped into soft and hard interactions. Soft processes, where α_S is large, cannot be calculated perturbatively.

Hard processes on the other hand, which are characterised by large momentum transfer, can be calculated using perturbation theory because α_S is small. The cross sections for hard quark and gluon interactions can be calculated using the Feynman rules derived from the QCD Lagrangian with the fundamental interactions given by the quark-gluon vertex and the gluon-gluon vertex. The running of the strong coupling constant can be derived from perturbation theory itself. Higher order corrections in the form of (virtual) loops introduce diverging contributions because the loop momenta are not constrained. For the gluon propagator, loop corrections have to be considered from virtual quarks as well as virtual gluons. Renormalisation allows to absorb these divergences into the strong coupling constant α_S. As a consequence of this procedure α_S becomes a function of the renormalisation scale μ_r.

2.2.2 Proton structure

In order to calculate cross sections for proton-proton collisions one must consider that protons are bound states, composed of the valence quarks, uud, and of virtual quark-antiquark pairs and virtual gluons. A consequence of the renormalised coupling in QCD is asymptotic freedom, which means that in high energy collisions with large momentum transfer $|q^2| \gg \Lambda^2_{QCD}$, quarks and gluons inside a proton can be treated as essentially free particles. The high momentum transfer can be translated to short length scales to which the proton structure will be resolved. The structure of the proton is described by the parton distribution functions (PDFs), $f_q(x, q^2)$, which give the probability to extract a parton of a given flavor with a fraction x of the proton momentum in a hard interaction. The dependence on the momentum transfer q^2 indicates that the structure changes depending on the length scales with which the proton is probed. The PDFs can not be calculated from QCD perturbation theory, but instead are determined from fits to experimental data obtained from fixed target and electron-proton deep inelastic scattering experiments, as well as proton-antiproton cross sections. Several collaborations perform these fits to global data [18, 19], the results of the MSTW fit [20] is shown in Fig. 2.4. As a general feature of the distribution functions the valence quarks u, d carry roughly one third of the momentum, while gluons dominate the region of small x. With increasing q^2 more of the virtual gluon pairs are resolved and the gluon contribution becomes more important.

With the help of the process independent PDFs, perturbation theory can be used to calculate cross sections for proton collisions. According to the QCD factorisation theorem,

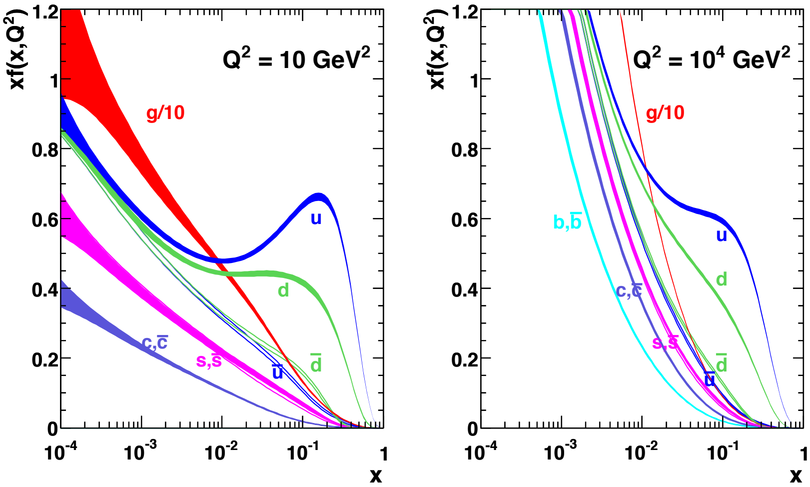

Figure 2.4: MSTW 2008 NLO parton distribution functions at $q^2 = 10\,\mathrm{GeV}^2$ (left) and $q^2 = 10^4\,\mathrm{GeV}^2$ (right). The x axis shows the fraction of the proton momentum, x, carried by the parton, and the y axis shows x times the probability, $f(x)$, to find a parton of a given type with that momentum [20].

the cross section for any hard scattering process $pp \to X$ with $|q^2| \gg \Lambda^2_{QCD}$ can be written as:

$$\sigma_{pp\to X} = \sum_{a,b} \int dx_1 dx_2 f_a(x_1, q^2) f_b(x_2, q^2)\, \hat{\sigma}_{ab\to X}(q^2) \quad , \tag{2.2}$$

where $f_{a/b}(x_{1/2}, q^2)$ $(a/b = q, \bar{q}, g)$ are the PDFs of the colliding protons, $\hat{\sigma}_{ab\to X}$ is the partonic cross section calculable with perturbative QCD and the sum runs over parton flavors [21]. The scale q^2 introduced here is called the factorisation scale (in the following μ_F). It divides between contributions from hard radiative corrections included in the perturbative calculation and the soft gluon emissions which are absorbed in the PDF. In this way the soft QCD describing the internal structure of the proton is separated from the perturbative part describing the hard scattering of quarks and gluons.

2.2.3 Z production at hadron colliders

The theoretical description of Z production in hadron collisions is based on the Drell-Yan process, which is the application of the factorisation theorem to massive lepton pair production in hadron-hadron collisions [22]. The term Drell-Yan originally meant the production of lepton pairs through photon exchange. Since the same process can take place with Z boson exchange according to the electroweak theory, the meaning of the term is expanded to include to the interference of γ and Z exchange. By restricting the lepton pair invariant mass to a region around the Z mass, the cross section is dominated by Z exchange.

To obtain the cross section for $pp \to Z \to \mu^+\mu^-$ using the factorisation theorem, the partonic cross section $\sigma_{q\bar{q}\to\mu^+\mu^-}$ (and higher order contributions) has to be calculated. Since the initial state is dominated by QCD effects and the final state does not interact strongly,

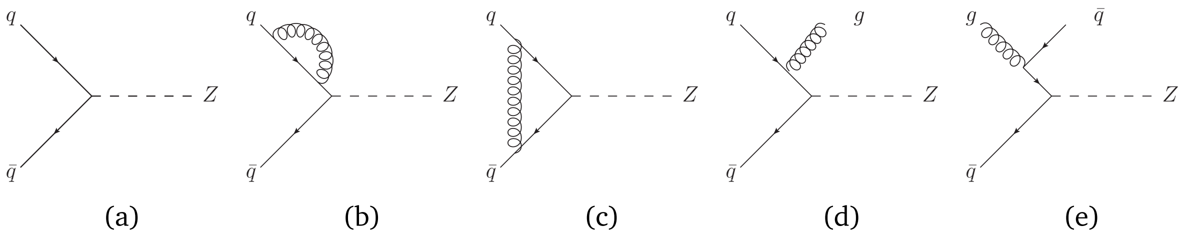

Figure 2.5: Feynman diagrams for Z production. (a) The leading order Drell-Yan diagram. (b)-(e) Next-to-leading order corrections to the Drell-Yan process.

the calculation can be simplified by separating production and decay. In the context of this thesis the production process is relevant.

The leading order production process for Z bosons is quark-antiquark annihilation. At the next higher order, the Z can be radiated by a quark that has been excited by a gluon. The real and virtual corrections to the Drell-Yan process of order α_S are shown in Fig. 2.5. At leading order, Z bosons are produced with zero transverse momentum due to momentum conservation since the initial state partons carry only momentum along the beam axis. The higher order processes with real emission of gluons, and of quark-gluon scattering introduce a boost of the Z boson.

The differential cross section as a function of p_T has been calculated including higher order corrections up to second order in α_S [23]. However, the perturbative expansion of the cross section includes terms proportional to $\alpha_S^n \ln^m(M^2/p_\mathrm{T}^2)$ (with $m \leq 2n-1$) at each order n [24]. For $p_\mathrm{T}^Z \ll M$ these higher order terms are not small, in fact each terms by itself diverges for $p_\mathrm{T} \to 0$. The correct sum of the corrections of all orders would provide a finite cross section but a truncated perturbation series does not provide a valid prediction for low p_T.

Transverse momentum resummation

The largest part of the Z boson production cross section occurs with small values of transverse momentum ($p_\mathrm{T} \ll M$) where the fixed order predictions are not valid. The diverging terms can be identified with large contributions to the cross section from the emission of soft and collinear gluons. Considering only the leading contributions at each order of α_S, the cross section is:

$$\frac{1}{\sigma}\frac{d\sigma}{dp_T^2} \simeq \frac{1}{p_T^2}\left[A_1\alpha_S \ln(M^2/p_T^2) + A_2\alpha_S^2 \ln^3(M^2/p_T^2) + \ldots + A_n\alpha_S^n \ln^{2n-1}(M^2/p_T^2) + \ldots\right] \quad ,$$

where the A_i are calculable coefficients of order unity [15]. When taking into account the size of the coefficients A_i and α_S, the limit below which the higher order terms can not be neglected is $10-15\,\mathrm{GeV}$. Even though it is not possible to calculate all higher order corrections, the form of the leading logarithmic terms $\alpha_S^n \ln^{2n-1}(M^2/p_T^2)$ can be extracted. The solution that allows to calculate predictions for $p_\mathrm{T} \ll M$ is to summarise these leading logarithmic terms from all orders in α_S [25]. A resummation formalism has been developed

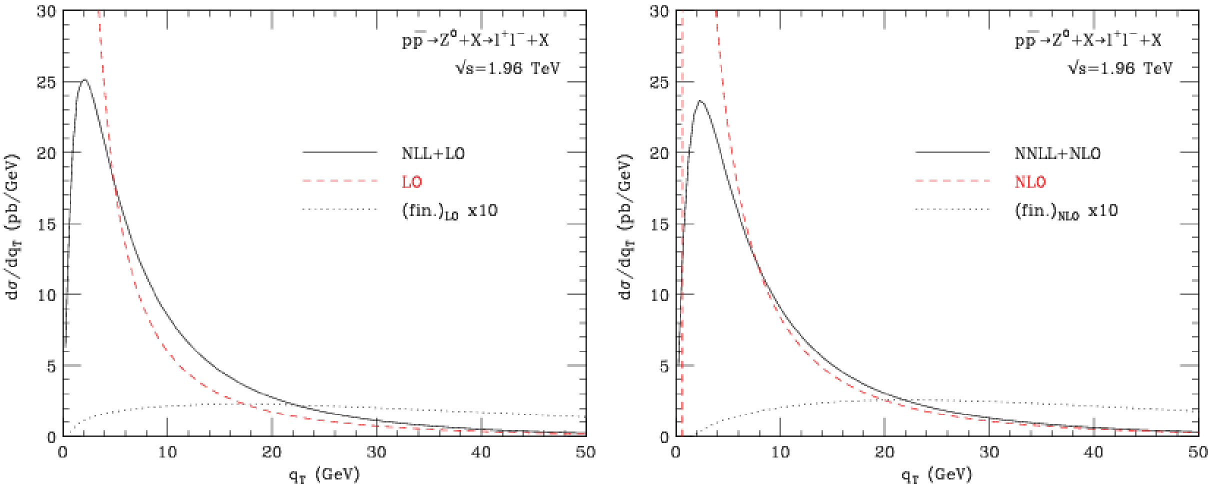

(a) (b)

Figure 2.6: Predictions for the p_T spectrum of Z bosons using transverse momentum resummation. (a) results at NLL+LO (b) and NNLL+NLO accuracy. The full result is compared to the corresponding fixed-order result (dashed line) and to the finite difference between the fixed order result and the expanded resummed result (dotted line) in each case [27].

to include all contributions up to next-to-next-to-leading logarithmic (NNLL) accuracy [26]. To get a consistent result for small and large values of p_T the resummed cross section has to be matched with fixed order predictions at NLO:

$$\left(\frac{d\sigma}{dp_T}\right)_{\text{NNLL+NLO}} = \left(\frac{d\sigma}{dp_T}\right)_{\text{NNLL}} + \left(\frac{d\sigma}{dp_T}\right)_{\text{NLO}} - \left(\frac{d\sigma}{dp_T}\right)_{\text{NNLL expanded to NLO}} ,$$

where the last term is the expansion of the resummed result up to the same order as the fixed order calculation thus avoiding double counting [27]. Figure 2.6 show the NLL+LO as well as the NNLL+NLO predictions for the p_T distribution at the Tevatron using this procedure. In addition the (diverging) fixed order results for LO and NLO are shown by themselves as well as the finite difference obtained after subtracting the expanded NLL/NNLL cross section from the LO/NLO cross sections. Numerical predictions for the resummation at low pt matched to next-to-leading-order (NLO) calculation can also be produced with the RESBOS generator.

Theoretical predictions are limited in precision due to the unknown contributions of higher order terms that are not included in the calculation. The size of the effects is best estimated by varying the scale factors used to separate perturbative and non-perturbative effects. The choice of these unphysical scale factors is somewhat arbitrary, and different choices can be argued for. For Z production the mass of the Z boson is the characteristic energy scale of the event, it is therefore chosen for the renormalisation and factorisation scales. Scales are varied by a factor 2 to estimate the effect of leaving out the higher order terms. The resulting theoretical uncertainties for the predictions from resummed calculations are shown in Fig. 2.7 [27]. As can be seen, the uncertainties are substantially

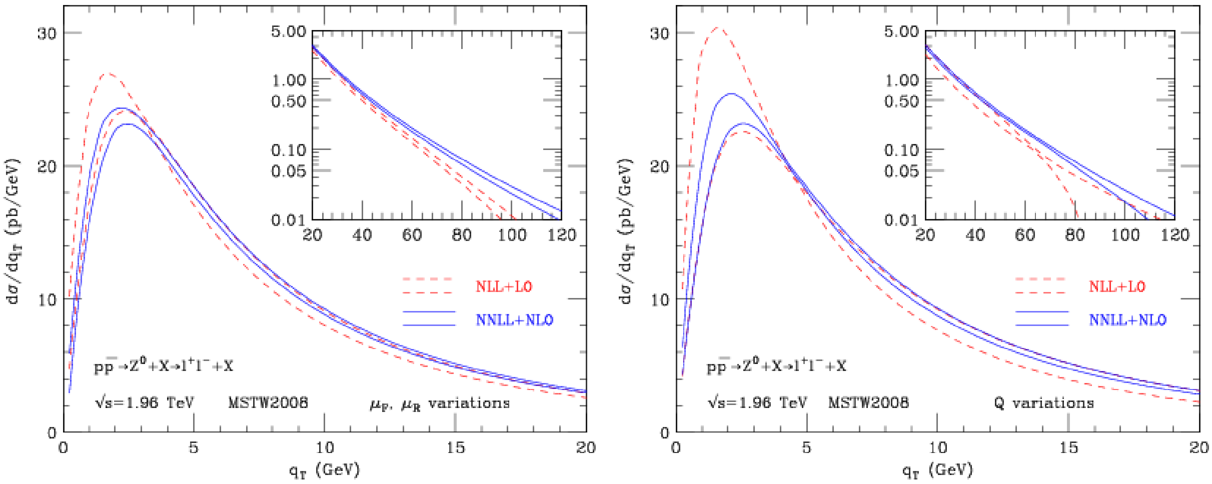

(a) (b)

Figure 2.7: Theoretical uncertainty of the p_T spectrum of Z bosons due to scale variations. The bands are obtained (a) by varying μ_F and μ_R and (b) by varying the resummation scale [27].

reduced when using the higher order calculations.

2.2.4 Parton showers

A practical approach to calculate higher order effects is given by the parton shower technique [28]. Starting from the initial and final state quarks and gluons produced in a hard process, it describes the successive radiation of gluons and gluon splitting into quark-antiquark pairs.

The parton shower technique uses the approximation of repeated independent emissions or splittings of the kind $q \to qg$, $q \to gq$, $g \to gg$, $g \to qq$, where the splitting probability is described by a set of splitting functions P_{qq}, P_{gq}, P_{gg} and P_{qg}. The phase space for the splitting $a \to bc$ can be parameterised by the momentum fraction z taken by b, with $1-z$ taken by c, the opening angle θ between b and c, and the azimuth angle ϕ. Each function $P_{ij}(z,\phi)$ describes the emission of a parton with particular flavour j and momentum fraction z from a parton of flavour i. With this notation the emission probability is

$$d\mathscr{P}_i = \frac{\alpha_S}{2\pi}\frac{d\theta^2}{\theta^2}\int dz P_{ij}(z). \tag{2.3}$$

The probability diverges for $\theta \to 0$, that means when to two outgoing partons are collinear. The collinear divergence of the splitting probability can be treated by introducing a cutoff value for θ. This can be seen as a limit on the resolution since a measurement cannot differentiate between one parton and two exactly collinear partons with the same total momentum. The value for this limit can be better expressed when using an alternative paramerisation of the phase space in terms of the virtuality of the quark $q^2 = z(1-z)\theta^2 E^2$, where E is its energy, or the transverse momentum of the gluon with respect to the parent quark $k_{\mathrm{T}}^2 = z(1-z)^2\theta^2 E^2$. In terms of the virtuality the limit is usually set to a value of 1 GeV, below which confinement sets in.

In order to obtain the exclusive one gluon emission probability an ordering of the emissions by θ or alternatively of the virtuality q^2 or transverse momentum k_{T} has to be introduced, where ordering means that the first branching is the hardest of all branchings. The probability that no branching occurs at a value larger than q^2, given a maximum possible virtuality Q^2, defines the function $\Delta_i(Q^2, q^2)$. It follows the differential equation

$$\frac{d\Delta_i(Q^2,q^2)}{dq^2} = \Delta_i(Q^2,q^2)\frac{d\mathscr{P}_i}{dq^2} \tag{2.4}$$

with the solution

$$\Delta_i(Q^2,q^2) = \exp\left(-\int_{q^2}^{Q^2}\frac{dk^2}{k^2}\frac{\alpha_S}{2\pi}\int_{Q_0^2/k^2}^{1-Q_0^2/k^2} dz P_{ij}(z)\right). \tag{2.5}$$

The value of the maximum virtuality Q^2 needs to be fixed. In order to avoid double counting, it should be ensured that parton shower emissions should be softer than the partons coming out of the matrix element, for example by setting the Q^2 to the momentum transfer scale of the hard process.

The non-branching probability can be used to construct the parton shower. In an iterative procedure, the parton shower evolves quarks and gluons downwards in virtuality q^2, starting from the maximum virtuality Q^2, down to a scale Q_0^2, typically $\approx$ 1GeV at which partons start to be confined into hadrons. For each parton at a given virtuality Q^2, the probability not to radiate a soft or collinear gluon, or for a gluon to split into a quark-antiquark pair at a lower scale q^2, is given by the Sudakov form factors $\Delta_i(Q^2,q^2)$ which can be derived from the collinear splitting functions $P_{ij}(z)$ as described above. The q^2 at which a branching occurs is obtained by generating a flat random number ρ between 0 and 1 and solving the equation $\Delta_i(Q^2,q^2) = \rho$ for q^2. A branching is generated at q^2 if the solution is $q^2 > Q_0^2$. The procedure is repeated for each produced parton until $q^2 < Q_0^2$ [28].

Implementations of the parton shower are provided for example by the PYTHIA, HERWIG and SHERPA programs. In the case of PYTHIA, the evolution is performed in order of decreasing virtuality as described above, while HERWIG uses angular ordering. The evolution can alternatively be formulated as emissions from colour dipoles, which is implemented in PYTHIA 8 and SHERPA. These parton shower programs can be used in combination with other programs providing the hard scattering matrix element. Parton shower algorithms are constructed using soft and collinear approximations to the full cross section. Processes with hard wide angle emissions, like Z production with large transverse momentum, can only be described accurately using higher order matrix elements. The parton shower formalism can also be applied to the final states of higher order predictions, if care is taken to avoid double counting of phase space. The correct matching of NLO matrix element and parton shower is implemented in the POWHEG and MC@NLO event generators.

Hadronisation

It has been stated so far, that the parton shower evolution has to be cut off at some scale at which the effects of confinement set in. This must happen at an energy scale close to the hadron masses, which means non-perturbative models to group final state partons into hadrons must be used. The two main models for hadronisation are the string and cluster models. In the Lund string model, implemented in PYTHIA, separating partons stretch between them a colour string which breaks up after pumping sufficient energy into the system, that is by separating the quarks over a distance quark-antiquark pairs are produced. Hadrons are then formed by the combination of adjacent quarks. The cluster model, implemented in HERWIG, takes a different approach. Gluons are are split into quark-antiquark pairs, and all quarks are grouped into colour singlet clusters. The transition from clusters to hadrons is done via decays. Both models need tuning to experimental data to correctly describe hadron formation.

Chapter 3

LHC and ATLAS

3.1 The Large Hadron Collider

The Large Hadron Collider (LHC) [29] is a proton-proton accelerator designed for a beam energy of 7 TeV and a peak luminosity of $10^{34}\mathrm{cm}^{-2}\mathrm{s}^{-1}$, with the option to accelerate and collide heavy ion (lead) beams with an energy of up to 2.76 TeV per nucleon and a luminosity of $10^{27}\mathrm{cm}^{-2}\mathrm{s}^{-1}$. The LHC was installed in the tunnel of the LEP accelerator at CERN and makes use of the existing accelerator chain to supply it with 450 GeV proton beams.

Four large detectors have been built around the four interaction points of the LHC. The ATLAS [30] and CMS [31] experiments are designed to make use of the highest luminosity and to study a broad physics program. The LHCb experiment [32] intends to measure precisely CP violation and rare decays of B hadrons at a lower peak luminosity of $10^{32}\mathrm{cm}^{-2}\mathrm{s}^{-1}$. The ALICE experiment [33] specifically studies heavy ion collisions and the properties of quark-gluon plasma in special ion runs.

The main performance goals in the design and construction of the LHC were high energy and high luminosity. Unlike in e^+e^- colliders the beam energy at LHC is not limited by synchrotron radiation. In the accelerating phase, the protons gain 485 keV per turn inside the radio frequency cavities, compared with 7 keV energy loss due to synchrotron radiation (at 7 TeV). The beam energy limitation comes from the magnetic field strength needed to bend the beams around the radius of the ring. The LHC uses superconducting dipole magnets, cooled with liquid helium to 1.9 K, which can produce the magnetic field of 8.33 T needed for 7 TeV beams. At such high magnetic fields the temperature margins of the superconducting magnets are very small and therefore the heat load on the magnets, for example through beam losses, needs to be carefully controlled. Stable LHC operation has been achieved so far with energies up to 4 TeV per beam. The peak luminosity can be achieved by circulating 2808 proton bunches with 1.15×10^{11} protons each inside the LHC. At these values each bunch crossing is expected to produce on average 23 inelastic proton-proton collisions.

After a commissioning phase at lower beam energies and intensities in 2009, the physics program started with collisions at 7 TeV center-of-mass energy in 2010 and 2011. The LHC accelerator delivered high energy proton-proton collisions to ATLAS and CMS with an integrated luminosity of about 50 pb^{-1} in 2010 and 5.5 fb^{-1} in 2011. For 2012 the beam energy was raised to 4 TeV. A longer technical stop in 2013 and 2014 will be used to prepare the LHC to operate at the design energy of 7 TeV per beam.

3.2 The ATLAS experiment

The ATLAS experiment [30] is a general purpose detector designed to study new physics phenomena at the TeV scale and to perform precision measurements of the Standard Model. The signatures of the interesting processes involve photons, electrons, muons, taus, as well as high energy (b-)jets, and neutrinos. Efficient and precise measurements of position and energy of these objects are needed. The presence of neutrinos needs to be inferred from the undetected energy they carry away, requiring hermetic detectors and excellent energy resolution. At the LHC the cross section for QCD jet production dominates all the interesting new physics phenomena, which means excellent particle identification is needed. Further, the event recording needs efficient triggers on the interesting physics signatures, to keep the rates at a level that can be read out, stored and processed offline. The high luminosity also leads to a very high total rate of inelastic proton-proton collisions such that each bunch crossing will produce on average 23 inelastic collisions. These ’pileup’ events produce additional signals in any studied event, against which the event reconstruction needs to be robust. ATLAS has been designed to cope with the experimental conditions at the LHC, which means radiation resistant detectors, fast readout and high granularity.

The ATLAS detector is constructed of several subdetectors with specific purpose and technology that form layers around the nominal interaction point. The main features will be reported in the following based on the detailed description given in Ref. [30]. Closest to the interaction point are the inner tracking detectors (silicon pixel, silicon strip, straw tube tracker) which are contained inside a solenoid magnet with 2 T, to allow efficient tracking. These are surrounded by an electromagnetic calorimeter for electron and photon identification and a hadron calorimeter for jet and missing transverse energy measurement. Outside the calorimeter is the muon spectrometer, with a toroid magnet with 1-2 T, to allow muon identification, and muon momentum and charge measurement at the highest energies. The layout of ATLAS showing these detector components is shown in Fig. 3.1.

The coordinate system used in ATLAS is defined in the following. The nominal pp interaction point at the centre of the detector is defined as the origin of the coordinate system. The z-axis is defined by the beam direction. The positive x-axis is defined by the direction from the interaction point to the centre of the LHC ring, with the positive y-axis pointing upwards. The azimuth angle ϕ is measured around the beam axis and the polar angle θ is the angle from the z-axis. The pseudorapidity $\eta = -\ln \tan(\theta/2)$ (or for massive objects the rapidity $y = 1/2 \ln[(E + p_z)/(E - p_z)]$) is used in place of the polar angle in most cases, because differences of it are invariant under Lorentz boosts along the z axis. The transverse momentum p_{T}, the transverse energy E_{T}, and the missing transverse energy $E_{\mathrm{T}}^{\mathrm{miss}}$ are defined in the $x - y$ plane. The commonly used distance ΔR in the pseudorapidity-azimuth angle space is defined as $\Delta R = \sqrt{\Delta\eta^2 + \Delta\phi^2}$.

3.2.1 Inner tracking detectors

The task of the inner detector (ID) is the reconstruction of tracks of charged particles in a high track density environment. This task is performed by the silicon pixel (Pixel) and strip

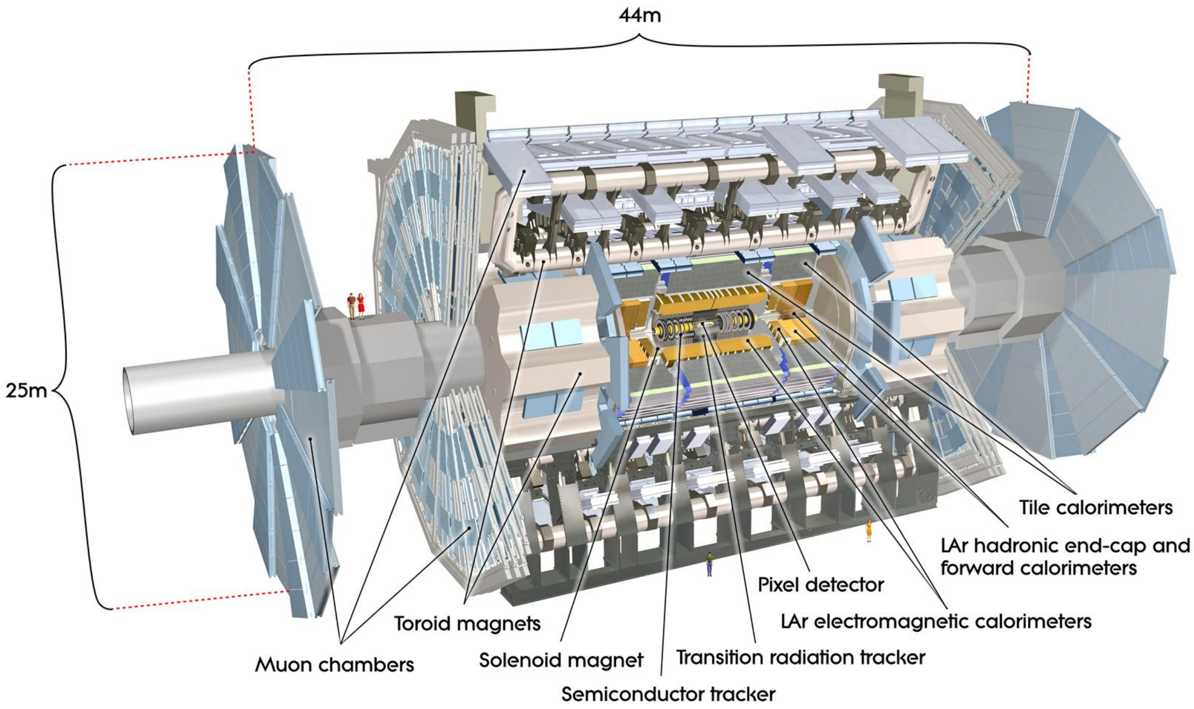

Figure 3.1: A cutout view of the ATLAS detector showing the main detector components [30]

(SCT) detectors and the straw tube transition radiation tracker (TRT). The ID is contained inside the central solenoid magnet which generates a 2 T magnetic field. The coverage of the silicon tracking detectors extends to $|\eta| = 2.5$, and that of the TRT to $|\eta| = 2.0$. The detectors are arranged on concentric shells around the beam axis in the barrel region and on disks perpendicular to the beam axis in the two endcaps. A computer image of a charge particle traversing the ID barrel region is shown in Fig. 3.2.

The pixel detector forms the three layers closest to the collision region, where the fine segmentation is needed due to the high track density and for precise reconstruction of primary and secondary vertex positions. The normal pixel size in $R-\phi \times z$ is $50 \times 400\,\mu\text{m}^2$, which allows intrinsic accuracies of $10\,\mu$m in $R-\phi$ and $115\,\mu$m in z/R for the barrel/endcaps.

The semiconductor tracker (SCT) consists of four double layers of silicon strip sensors with strip pitch of $10\,\mu$m and strip length of 6.4 cm. Each double layer is made of two sensors mounted at a small angle of 40 mrad, allowing to measure both coordinates. The SCT provides a precision measurement in $R-\phi$ with an accuracy of $10\,\mu$m in $R-\phi$ and $580\,\mu$m in z/R for the barrel/endcaps.

The TRT at largest radii adds up to 36 measurements of the $R-\phi$ coordinate per track with a precision of $130\,\mu$m. The straw tubes which form the TRT have a diameter of 4 mm and are oriented in z direction in the barrel and radially in the disks. The TRT also provides electron identification by measuring transition-radiation photons.

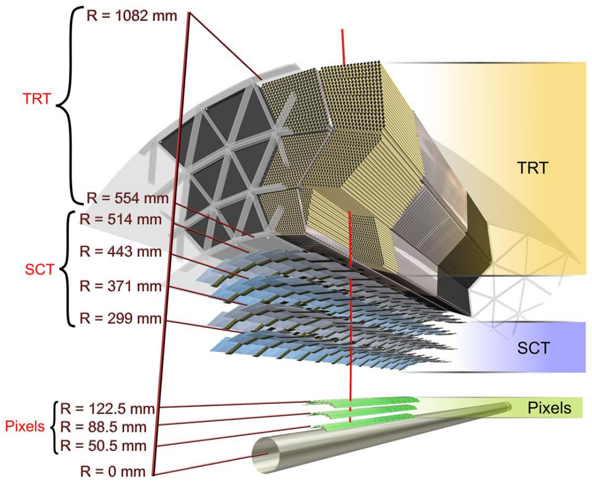

Figure 3.2: Computer image of a charged particle of $p_{\mathrm{T}} = 10\,\mathrm{GeV}$ traversing the inner tracking detectors. Shown is a section of the ID barrel and the beam pipe. [30]

3.2.2 Calorimeters

Sampling calorimeters covering the range up to $|\eta| = 4.9$ are used to measure the total energy of electrons, photons and hadronic jets. Calorimeters with several technologies are used, depending on the physics requirements and on the radiation levels in the detector region. The liquid argon electromagnetic calorimeter, covering a range up to $|\eta| = 3.2$, is finely segmented in $\eta - \phi$ with 3 segmentations in depth for precision measurements of electromagnetic showers. Hadronic calorimetry in the central region up to $|\eta| = 1.7$ is performed by the tile calorimeter, which uses steel as absorber and scintillating tiles as active material. The more forward regions are covered again by liquid argon calorimeters. In order to provide good energy resolution and also to shield the muon system, electromagnetic and hadronic showers need to be contained by the calorimeters. The electromagnetic calorimeter has a total thickness of > 22 radiation lengths. The total thickness of the active calorimeter is about 10 in terms of interactions lengths (λ). Together with inactive material from support structures, the total thickness is about $11\,\lambda$, enough so that hadronic punch-through is limited to rates lower then those of prompt and decay muons.

3.2.3 Muon spectrometer

Forming the outer part of ATLAS, the muon system is designed to detect charged particles which pass through the calorimeters and measure momenta up to $|\eta| < 2.7$. The muon system also provides trigger capability for the region $|\eta| < 2.4$. The muon system was designed with the performance goal of 10% momentum resolution for 1 TeV tracks. The low momentum limit for muons to reach the muon system is $\sim 3\,\mathrm{GeV}$, due to energy loss in

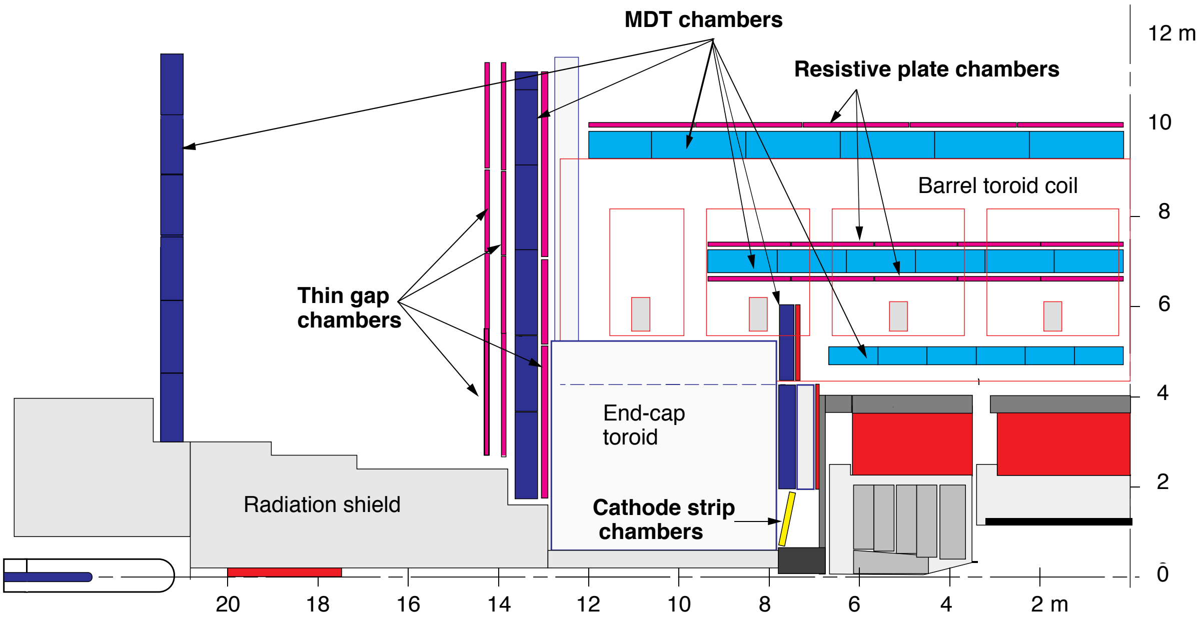

Figure 3.3: Cross section of the muon system in an $R-z$ plane [30].

the calorimeter. In the muon system high precision tracking chambers are combined with separate fast readout trigger chambers.

The principle of the momentum measurement in the muon system is to measure the deflection of charged tracks in the magnetic field using precision measurements at three stations along the track. The magnetic field is produced by three superconducting air core toroid magnets. The barrel toroid covers the region $|\eta| < 1.4$ and the two endcap toroids cover the region $1.6 < |\eta| < 2.7$, the magnetic field in between is produced by the overlap of barrel and endcap toroid fields. The advantage of using toroid magnets is that the magnetic field created by them is orthogonal to the muon tracks in most regions. At the same time, the toroid design uses relatively little material thereby minimising multiple scattering. For high energy tracks the performance is determined by the bending power of the magnets, given by the integrated magnetic field strength along the tracks, which ranges from $1-7.5$ Tm.

A cross section of the muon system is shown in Fig. 3.3. The tracking chambers are mounted between and on the coils of the barrel toroid, and in front and behind the two endcap toroids. In the barrel they are grouped in three concentric cylinders around the beam axis at radii of approximately 5 m, 7.5 m and 10 m. In the end cap regions the chambers are mounted on wheels perpendicular to the beam axis at distances of 7.4 m, 10.8 m, 14 m and 21.5 m. The chambers are installed with some overlap, allowing alignment between chambers. In the centre of the detector, around $\eta = 0$ there is a gap that is needed to pass the services of the solenoid magnet, the calorimeters and the inner detector. The size of the gap is up to 2 m changing around ϕ. The large detector support structures under the detector cause acceptance gaps in the barrel region at $\phi = 240°$ and $300°$.

The precision measurement in the bending plane is performed by monitored drift tubes (MDT) chambers, which equip the 3 barrel layers at $|\eta| < 2.0$, and the 2 outer layers at

$2.0 < |\eta| < 2.7$. The MDT chambers consist of 3 to 8 layers of drift tubes, each drift tube with a diameter of 29.97 mm, operating with Ar/CO_2 gas at 3 bar. The MDT resolution is about 80 μm for individual tubes and 35 μm per chamber. The innermost precision measurement in the forward regions comes from cathode-strip chambers (CSC) that are able to deal with the higher rates and have better time resolution. These are multiwire proportional chambers with readout over segmented cathodes. The CSC measure both track coordinates, in the bending plane the resolution is 40 μm and 5 mm in the transverse plane.

Trigger capability in the barrel region ($|\eta| < 1.05$) is added by resistive plate chambers (RPC), and in the endcap region ($1.05 < |\eta| < 2.4$) by thin-gap chambers (TGC). Both chamber types deliver signals with a spread of 15-25 ns, thus can be used to identify the correct bunch crossing. The trigger chambers measure both coordinates of the track, with precision sufficient to set momentum thresholds for the trigger.

The stated accuracies of the deflection measurement of the precision chambers can only be reached, if the positions of the MDT wires and the CSC strips are known with a precision better then 30 μm. To accomplish this, the tubes were mounted with high mechanical precision in the chambers, and the chamber positions and deformations are monitored with an optical alignment system. In addition, muon tracks are used to align the chambers with respect to each other. The amount of material traversed by muons in the muon system is about 1.3 radiation lengths, resulting in multiple scattering effects being the dominating resolution degrading factor for muon momenta between 30 GeV and 200 GeV. The measurement of higher momenta is limited by the intrinsic and alignment precision.

3.2.4 Trigger system

The task of the trigger system is to reduce the event rate from the 40 MHz bunch crossing rate ($\sim$1 GHz event rate at design luminosity) down to 200 Hz which is the limit of the data recording rate of ATLAS. It is implemented in three levels, each refining the decision made by the previous level and reducing the rate.

The first level (L1) trigger is based on custom electronics and uses fast algorithms on a subset of the detector information enabling it to reach a trigger decision in 2.5 µs and an output rate of 75 kHz. The L1 trigger reconstructs muons using only the measurements of the RPC and TGC in the muon spectrometer. Electromagnetic clusters, jets, $\tau-$leptons and large missing or total transverse energy are reconstructed from readout of all calorimeters at reduced granularity.

The level-2 (L2) and event filter (EF), together referred to as high-level trigger (HLT), are implemented in software and use full-granularity readout to allow reconstruction close to the offline reconstruction. To limit the amount of data to be transferred, the L2 trigger is seeded by regions-of-interest (RoI's) information supplied by the L1 trigger. The RoI information contains the region in $\eta-\phi$ where a trigger object was found, together with information about the type of signature and its energy. The output rate after the L2 trigger is reduced to below 3.5 kHz, taking on average 40 ms to process one event. The further reduction of the rate down to 200 Hz is performed by the event filter. With access to the full event data and calibration databases, the event filter reconstructs the entire event and applies offline analysis procedures.

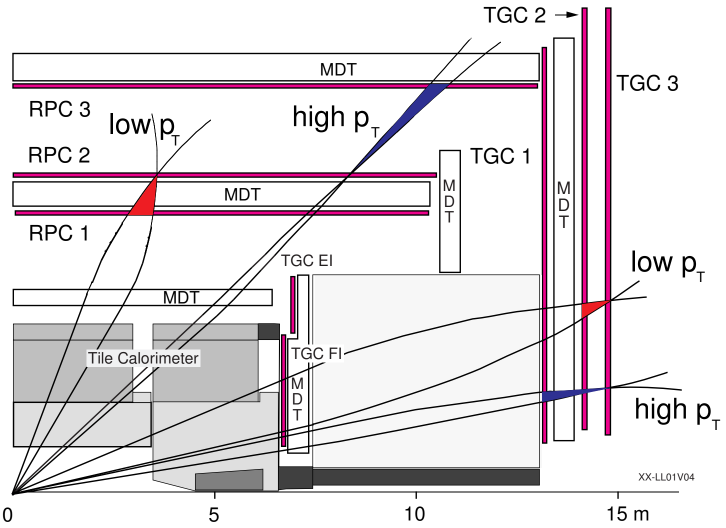

Figure 3.4: Illustration of the muon trigger roads in a cross section of the muon system in the $R-z$ plane. The trigger roads for low and high p_T muons in the barrel and endcap regions are shown in blue and red [34].

The L1 muon trigger is based on the RPC in the barrel ($|\eta| < 1.05$) and the TGC in the endcap ($1.05 < |\eta| < 2.4$), which are fast enough to identify the correct bunch crossing. The basic idea of the muon trigger in both the endcap and barrel regions is to search for a coincidence of hits in the three trigger stations within a projective region. The centre of the region is defined by the path of an infinite momentum muon from the vertex to the muon system. The width of the region defines a threshold for the transverse momentum of muons, where a smaller region corresponds to higher p_T. An illustration of the trigger algorithm is shown in Fig. 3.4. In the barrel region, each of the three RPC stations consist of a double layer of detectors, each one measuring the η and ϕ coordinates. The trigger algorithm is started by a hit in the central layer. This defines the centre of the road within which hits in the other layers are searched. For low p_T threshold a coincidence of 3-out-of-4 hits in the inner two layers is required. The high p_T threshold requires in addition a 1-out-of-2 coincidence with the outer station. In the endcap region the principle is the same, but there the outermost station starts the trigger and the coincidence is checked in R and ϕ. The geometrical coverage of the L1 muon trigger is about 99% in the endcap region and about 80% in the barrel region.

The L2 muon trigger is passed the RoI from the L1 trigger and first performs a pattern recognition on the hits in this region, including the precision MDT hits. Then a fast track fit is performed using these hits and the MDT drift times, from which the p_T is determined. At L2 a combination of the track reconstructed in the muon system with a track in the inner detector is formed, which improves resolution and helps to reject muons from decays of light mesons created in the calorimeter. At the EF trigger stage the full muon reconstruction starting with the input of L1 and L2 is performed.

Chapter 4

Event reconstruction

This chapter describes the reconstruction of the physics objects which are needed for the analysis of the $Z \to \mu^+\mu^-$ process. This analysis needs charged particle tracks reconstructed in the inner detector (ID) and in the muon spectrometer (MS), which are used to reconstruct and identify muons. Moreover the tracks of charged particles are used for the primary vertex reconstruction. Information about the primary vertex is used to reject non-primary collision backgrounds and can be used to estimate the amount of pileup. For all used physics objects the reconstruction is provided by the standard ATLAS reconstruction software.

The reconstruction of charged particle tracks is described in the following section for the inner detector, and in Section 4.3 for the muon spectrometer, after the description of the primary vertex reconstruction in Section 4.2. The reconstruction and identification of muons is summarised in Section 4.4. The performance of the muon measurement relating to the reconstruction efficiency and the momentum resolution is described in Section 4.5.

4.1 Track reconstruction in the inner detector

The tracks of charged particles with transverse momentum $p_{\mathrm{T}} > 0.5\,\mathrm{GeV}$ and $|\eta| < 2.5$ are reconstructed from the ID measurements [30]. The ATLAS track reconstruction algorithm [35] incorporates several pattern recognition and track fitting methods, as well as track extrapolation which uses accurate models of the active and passive material of the ATLAS detector. The track reconstruction uses as input calibrated hit clusters from the pixel and SCT detectors and calibrated drift circles, which are obtained from the TRT drift time measurement.

The primary track reconstruction strategy is to first build tracks for prompt particles, by seeding the track reconstruction from the measurements of the innermost detector layers. In a preparation step, the pixel detector (Pixel) and semiconductor tracker (SCT) hit clusters are converted into three dimensional space points, where the SCT clusters from two layers of the stereo modules are combined. The space points from the pixel layers and the first SCT layer are then used to build track seeds. The directional information of the track seeds can then be used to extrapolate the tracks into the SCT. The extension is performed using a Kalman-filter approach, where the track is successively extrapolated to the next detector layer. If a hit is found on this layer within a search window defined by the track covariance matrix, it is added to the track and the track fit is updated. Otherwise the track extrapolation continues to the next active layer, to account for the possibility of a missing measurement. After the track has been extrapolated to the outermost active layer, outlier hits which degrade the quality of the track fit are removed from the track. When the track building from all track seeds is completed, there are often ambiguities from hits that are shared by tracks. In addition many fake and incomplete tracks are present. These issues are resolved by ranking the tracks according to a score calculated from the fit quality and the types of hits associated to the track. Shared hits are mostly assigned to the higher ranked track and the lower ranked tracks are refit without the shared hits. Fake and incomplete tracks with low score are rejected at this stage. Finally, the TRT drift-circle information is added to the tracks and a refit using the full information is performed. Hits and drift circles that degrade the fit quality are classified as outliers and are not included in the final fit.

A second tracking method is used to recover tracks not found by the inside-out tracking, for instance secondary tracks from photon conversions or decays of long lived particles. This method starts by searching for unassociated track segments in the TRT which are then extrapolated back into the SCT and pixel detectors.

4.2 Vertex reconstruction

The primary vertices are reconstructed from the inner detector tracks using a two step iterative procedure [36]. A preselection of tracks compatible with originating from the interaction region is performed in order to remove tracks originating from secondary interactions. First, a vertex candidate is identified by finding the global maximum in the distribution of z-position of the tracks, computed at the point of closest approach to the beam spot. The beam spot is defined as the centre of the interaction region, as determined from a fit to an unconstrained vertex distribution collected over some time. The vertex position is then determined with an adaptive fitting algorithm that uses the vertex candidate and tracks around it, down-weighting tracks less compatible with the vertex. Tracks that are incompatible with the already found vertex are disassociated from the vertex. This procedure is repeated with all tracks which are not yet associated to a primary vertex and additional primary vertices are constructed until no compatible tracks remain.

4.3 Muon reconstruction

The muon reconstruction is based on the measurement of the muon system and the inner detector. Different reconstruction strategies lead to the main types of muons [37]: Standalone muons are reconstructed from the muon spectrometer measurements only. Combined muons are obtained by building combinations of standalone muon tracks with inner detector tracks. Segment tagged muons are inner detector tracks that could be matched to a muon spectrometer track segment or to hits, which are not part of any standalone muon spectrometer track. A fourth strategy identifies muons based on the energy deposition in the calorimeters, without using muon spectrometer information. The different strategies are illustrated in Fig. 4.1 and described in more detail in the following. In addition to the existence of different strategies, the muon reconstruction is implemented

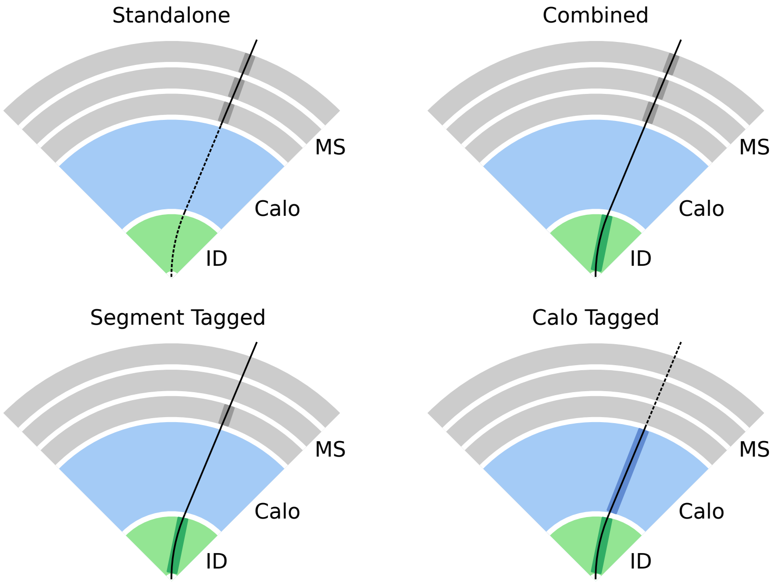

Figure 4.1: The four muon reconstruction strategies used in ATLAS: standalone, combined, segment tagged, calorimeter tagged. The muon is represented by a line from the interaction point outwards to the muon spectrometer. The line is dashed where the muon track is extrapolated outside the region it is measured. The detector regions whose measurement define the track parameters or are used to identify the muon are shown in a darker colour. The dark grey boxes indicate the measured track segments in the muon spectrometer layers.

in multiple reconstruction software packages, where each strategy exists in at least two software implementations. The implementations are divided into two families, each with a complete set of algorithms for each strategy. Both families produce separate muon collections, which are referred to by the name of the combination package - Staco and Muid. The two collections are very similar, in the sense that a muon reconstructed by an algorithm from the Staco family is also reconstructed by the corresponding algorithm in the Muid family as well as in the sense that the track parameters for reconstructed muons are compatible between the collections. Even though some different approaches where used in the Staco/Muid algorithms, the differences between the families are mainly due to the different treatment of special cases in the reconstruction, that are too intricate to detail here. Therefore the difference between Staco and Muid is mentioned only where a clear difference in design is used. This analysis uses muons from the Muid collection.

Standalone muons The track reconstruction in the muon spectrometer is based on the drift-time measurement in the monitored drift tubes (MDT) and the hit clusters in the cathode-strip chambers (CSC), resistive plate chambers (RPC) and thin-gap chambers (TGC). In a first step, straight line track segments are formed in single muon stations. Next, full tracks are built by associating segments that are on an extrapolated trajectory from the interaction region starting from segments in the outer stations. The final track

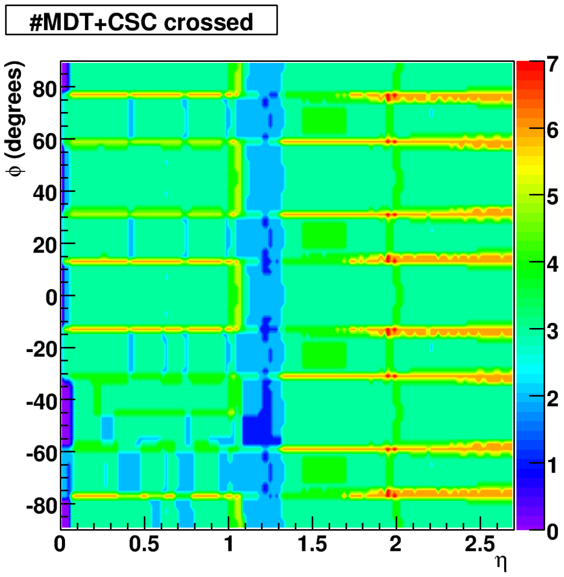

Figure 4.2: Number of muon spectrometer stations passed by muons as function of η and ϕ [37].

parameters are found by fitting all measurements of connected track segments taking into account the detailed geometrical description of the traversed material and the magnetic field along the track. The track parameters at the interaction point are found by extrapolation, taking into account multiple scattering and correcting the momentum for energy loss in the calorimeter. The energy loss in the calorimeter is estimated using a parameterization of the expected energy loss (most-probable value of a Landau distribution) or the measured calorimeter energy in case it exceeds significantly the most probable energy loss. The measured calorimeter energy is however only used if it is not increased by additional energy depositions of close by particles which would bias the muon momentum measurement. The standalone reconstruction allows efficient muon reconstruction up to $|\eta| = 2.7$, except in those detector regions where the muon passes less than 2 detector stations (mostly around $|\eta| = 0$ and $|\eta| = 1.2$, see Fig. 4.2 for the number of stations passed as function of $\eta - \phi$).

Combined muons The standalone muon tracks can be combined with tracks reconstructed in the inner detector. This significantly improves the momentum resolution for tracks with momenta below 100 GeV. The decision which tracks to combine is based on the match chi-square, defined as the difference between muon standalone and inner detector track vectors weighted by their covariance matrix. The track parameters for the combined track are determined either by statistical combination, taking into account the covariances, or by a refit of the track. Both choices are realised in two different implementations of the muon reconstruction algorithms. Combined muons have very similar reconstruction efficiency as standalone muons up to $\eta = 2.5$.

Segment tagged muons Segment tagged muons provide a way to identify inner detector tracks as muons even if the standalone muon could not be reconstructed, for instance in regions of reduced MS coverage. Tracks are extrapolated to the muon spectrometer and close by MS track segments or drift circles and clusters are searched. If they are found to be compatible with the track, the inner detector track is tagged as a muon. In cases where sufficient information is added by the associated track segments, a refit of the track taking these measurements into account is attempted. Otherwise, tagged muons keep the track parameters of the inner detector track.

Calorimeter tagged muons Calorimeter tagged muons are reconstructed without information from the muon system. The aim is mainly to recover efficiency in the regions without detector coverage by the MS, mostly around $\eta = 0$ (see Fig. 4.2), and to allow reconstruction of low energy muons. Inner detector tracks are tagged as muons if the energy depositions in the calorimeter along their trajectories is compatible with a minimum ionising signal. Calorimeter tagged muons allow to recover the efficiency loss from the acceptance hole at $|\eta| < 0.1$ which represents about 4% of the acceptance region of the combined reconstruction ($|\eta| < 2.5$). The fake rate of calorimeter tagged muons is however about 100 times higher compared with the other reconstruction methods.

4.4 Muon collections

For the study of the $Z \to \mu^+\mu^-$ process, the muon reconstruction needs to be efficient, have good momentum resolution and a low fake rate. The muon reconstruction efficiency as a function of η and p_T for standalone muons, combined muons and a combination of these with segment tagged muons is shown in Fig. 4.3. The segment tag algorithm allows to recover inefficiencies in the standalone reconstruction, mainly in the barrel-endcap transition region and the region of the detector feet. The fake rate for muons with $p_\mathrm{T} > 10\,\mathrm{GeV}$ is of the order of a few 10^-3 per event for these three muon types.

The relative momentum resolution for standalone and combined muons as a function of $|\eta|$ and p_T is shown in Fig. 4.4. Combined muons improve the momentum resolution significantly, especially in the region $1.1 < |\eta| = 1.7$. In this region, the standalone momentum measurement is degraded because muons traverse only two muon stations and because the magnetic field strength is reduced.

For physics analysis the standard approach is to use combined muons wherever possible, and adding additional muons from the standalone and tagged reconstruction to recover efficiency. A potential overlap between the different algorithms is avoided by ensuring that muon spectrometer segments or inner detector tracks are only used for exactly one muon candidate [37].

To ensure that the various ATLAS analyses are consistent in their use of muons, quality definitions for muons are introduced, classifying muons as *loose*, *medium* and *tight*. The quality definitions are listed in Table 4.1. The recommendation of the muon combined performance group in ATLAS is to use *tight* muons, since they provide the best momentum resolution [38].

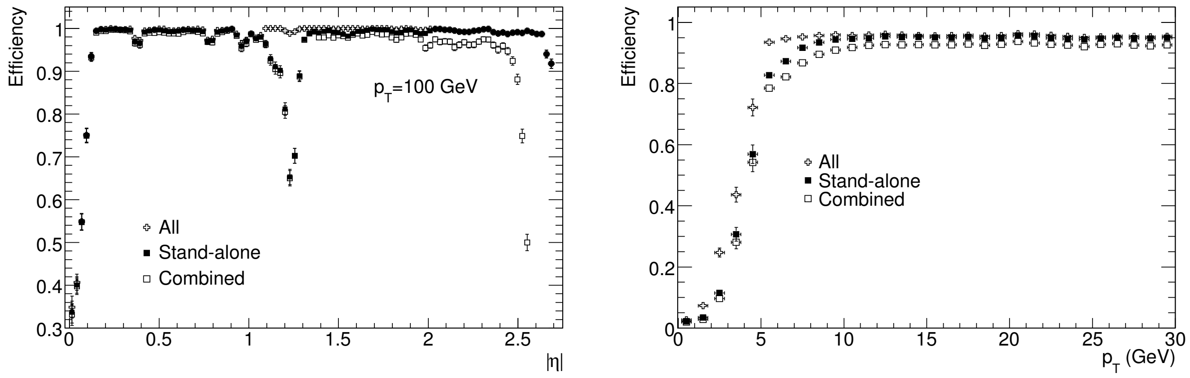

Figure 4.3: Muon reconstruction efficiency for muons with $p_T = 100\,\text{GeV}$ as a function of $|\eta|$ (left) and as a function ofp_T (right). The efficiency is shown for standalone muons (solid squares), combined muons (open squares) and the combination with segment tagged muons(open crosses) [30].

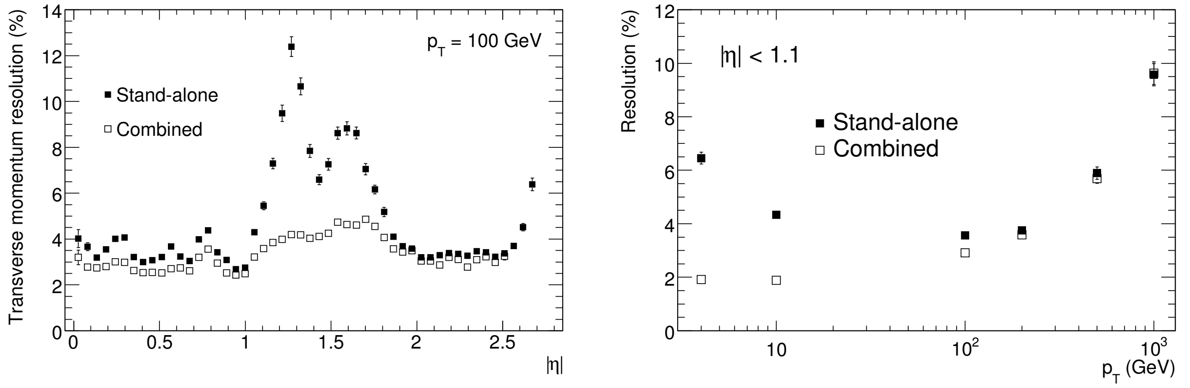

Figure 4.4: Relative momentum resolution as a function of $|\eta|$ (left) and p_T (right) for standalone muons (solid squares) and combined muons (open squares) [30].

Table 4.1: Definition of the muon quality classes for the Muid collection [39].

Quality class	Reconstruction method		
	Combined (Muid)	Standalone (Moore)	Segment tagged (MuGirl+MuTagIMO)
tight	yes	for $|\eta| > 2.5$	yes (with extended track)
medium	yes	for $|\eta| > 2.5$	yes (with extended track, *or* $|\eta| < 0.2$, *or* ≥ 2 track segments)
loose	yes	yes	yes

4.5 Muon performance measurements in data

4.5.1 Momentum resolution

The momentum resolution of muon tracks is limited by several factors. Chamber misalignment and intrinsic resolution of the detectors limit the precision with which the track curvature can be measured, resulting in a p_{T} uncertainty proportional to p_{T}^2. The effect of multiple scattering in material leads to an uncertainty on the muon direction and therefore the curvature measurement proportional to $1/p_{\mathrm{T}}$, which can be translated to a p_{T} uncertainty proportional to p_{T}. In addition, muons lose part of their energy in the calorimeter and passive material before reaching the muon system. For muon energies of $E < 100\,\mathrm{GeV}$ the predominant energy loss mechanism is ionisation. Only at energies of 300 GeV and higher, pair creation, bremsstrahlung, and nuclear interactions become important energy loss mechanisms [40]. In ionisation processes, muons can lose almost all their energy to one δ-electron, however the most probable energy loss in the calorimeter is a few GeV. As confirmed by the simulation of the energy loss using GEANT4, which implements the cross sections for the different energy loss processes correctly, the energy loss distribution follows an approximate Landau distribution [37]. The most probable energy loss and the width of the distribution depend on the momentum and the amount of material traversed. In the region of muon energies from 10 GeV to 100 GeV the energy dependence is weak, at $|\eta| < 0.15$ the most probable energy loss is 3 GeV and the width is about 0.3 GeV. The maximum energy loss for muon with energy 30 GeV is 22 GeV. The muon reconstruction corrects for this energy loss as described in Section 4.3 using a parameterization of the most probable energy loss or the measured energy loss in the calorimeter in case it exceed significantly the most probable value. The second option is however not available if additional particles have deposited energy in the calorimeter close or overlapping with the muon. As a result the energy loss fluctuations introduce uncertainty that is constant with p_{T}.

For the momentum measurement in the MS, fluctuations in the energy loss in material before entering the MS dominate at low p_{T}, while multiple scattering is the leading effect at medium p_{T}. For very high $p_{\mathrm{T}} > 300\,\mathrm{GeV}$ the chamber alignment and the intrinsic resolution of the detectors are the dominant effects [37]. The individual contributions to the momentum resolution and their p_{T}-dependence is illustrated in Fig. 4.5. The overall resolution can be parameterized with

$$\frac{\sigma(p_{\mathrm{T}})}{p_{\mathrm{T}}} = \frac{p_0^{\mathrm{MS}}}{p_{\mathrm{T}}} + p_1^{\mathrm{MS}} + p_2^{\mathrm{MS}} \cdot p_{\mathrm{T}}. \tag{4.1}$$

The momentum resolution in the ID can expressed in the same way, but there is no significant contribution from energy loss fluctuations:

$$\frac{\sigma(p_{\mathrm{T}})}{p_{\mathrm{T}}} = p_1^{\mathrm{ID}} + p_2^{\mathrm{ID}} \cdot p_{\mathrm{T}}. \tag{4.2}$$

For combined muons, the resolution is optimised over the entire p_{T} range due to complementary measurements in the inner detector and muon spectrometer. For low $p_{\mathrm{T}} < 30\,\mathrm{GeV}$

the resolution of the ID is better, because of the missing energy loss term, and smaller influence of multiple scattering. At very high $p_{\mathrm{T}} > 300\,\mathrm{GeV}$ the MS measurement is more precise, because of the much longer lever arm. For the intermediate region of p_{T} the resolution of both detectors is comparable [37].

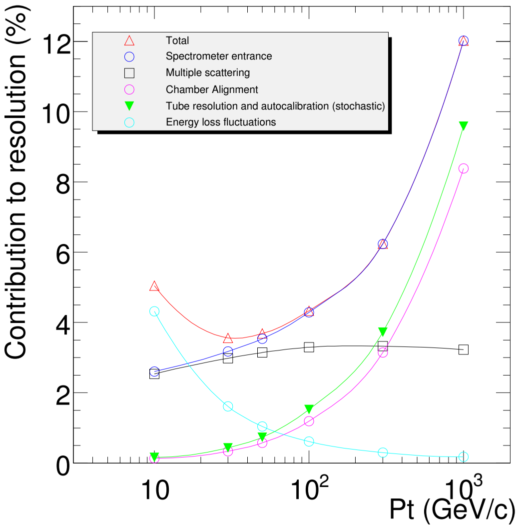

Figure 4.5: Momentum resolution for muons reconstructed in the MS as a function of p_{T} for $\eta < 2.5$. The individual contributions from energy loss fluctuations, multiple scattering, chamber alignment and intrinsic tube/hit resolution are shown [37].

The muon momentum resolution can be extracted from the measured resolution of the Z boson resonance, and from the difference between the independent MS and ID momentum measurements for combined muons from Z boson decays, as described in Ref. [41]. The method first modifies the resolution in the simulation to fit the data, and then the resolution parameters of Equations 4.1, 4.2 are taken from the corrected simulation. The procedure uses template fits to the invariant mass distribution and to the charge weighted momentum difference, $q/p_{\mathrm{T}}^{\mathrm{ID}} - q/p_{\mathrm{T}}^{\mathrm{MS}}$. The templates are taken from simulation with additional smearing of the form

$$p'_{\mathrm{T}} = p_{\mathrm{T}}(1 + g_1 \Delta p_1^{\mathrm{ID,MS}} + g_2 \Delta p_2^{\mathrm{ID,MS}} p_{\mathrm{T}}), \tag{4.3}$$

where $\Delta p_1^{\mathrm{ID,MS}}$ and $\Delta p_2^{\mathrm{ID,MS}}$ are the fit parameters related to the multiple scattering and intrinsic resolution terms, and $g_{1,2}$ is a random number from a Gauss distribution with mean 0 and width 1. The energy loss term is not included in the fit, because they it is well known from simulation and its contribution is secondary to the other effects for muon momenta above $20\,\mathrm{GeV}$. External constraints are applied on the parameters from the size of multiple scattering in the ID and alignment accuracy of the MS. The fitted parameters are shown in Table 4.2. Four regions in η with different momentum resolution are treated separately: barrel $0 < |\eta| < 1.05$; transition region $1.05 < |\eta| < 1.7$; end-caps $1.7 < |\eta| < 2.0$ and CSC/no TRT $2.0 < |\eta| < 2.5$. The determined parameters are in the following used to correct the simulation to reproduce the momentum resolution observed

	MS		ID	
η region	Δp_1^{MS}(%)	Δp_2^{MS}(TeV^{-}1)	Δp_1^{ID}(%)	Δp_2^{ID}(TeV^{-}1)
barrel	1.8 ± 0.05	0.095 ± 0.016	0	0.238 ± 0.011
transition	$3.17 \pm 0.15 \pm 0.22$	$0.25 \pm 0.026 \pm 0.067$	0	$0.736 \pm 0.022 \pm 0.567$
end-caps	1.23 ± 0.11	0.169 ± 0.069	0	0.871 ± 0.017
CSC/no TRT	0.52 ± 0.58	0.453 ± 0.028	0	0.050 ± 0.001

Table 4.2: Correction parameters for muon momentum resolution [41].

in data. The p_{T} dependence of the momentum resolution for the MS and ID measurements is shown in Fig. 4.6.

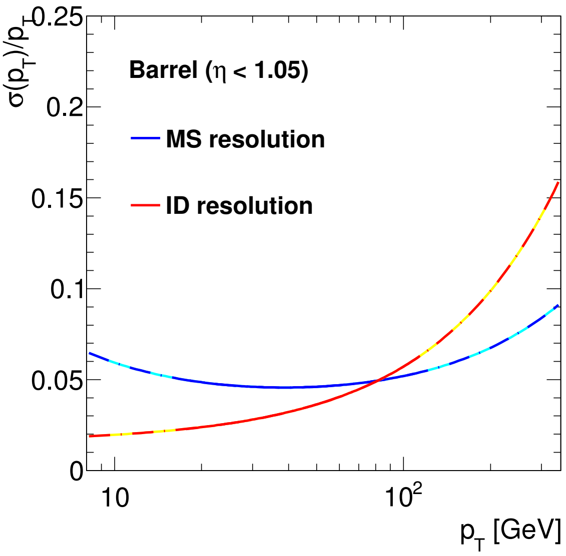

Figure 4.6: Muon momentum resolution as a function of p_{T} from the fitted resolution parameters obtained in [41]. The solid lines shows the region covered by the fit to data, the dashed lines show the extrapolation outside this region.

4.5.2 Reconstruction efficiency

The muon reconstruction efficiency is measured in data, using the muons from $Z \rightarrow \mu^+\mu^-$ events with the tag-and-probe technique [42, 43]. The measured efficiency for Muid *tight* muons as a function of $|\eta|$ and p_{T} is shown in Fig. 4.7. The efficiency is about 95% and nearly constant for $p_{\mathrm{T}} > 15\,\mathrm{GeV}$. The efficiency has a hole around $|\eta| = 0$ where no muon chambers are installed to allow services for the calorimeter and inner detector to pass. The efficiency is reduced by about 5% at $|\eta| = 1.1$, because in this region the MS coverage is reduced as well, and by 5% for $|\eta| > 2.4$ because the tracks do not pass all ID layers. The

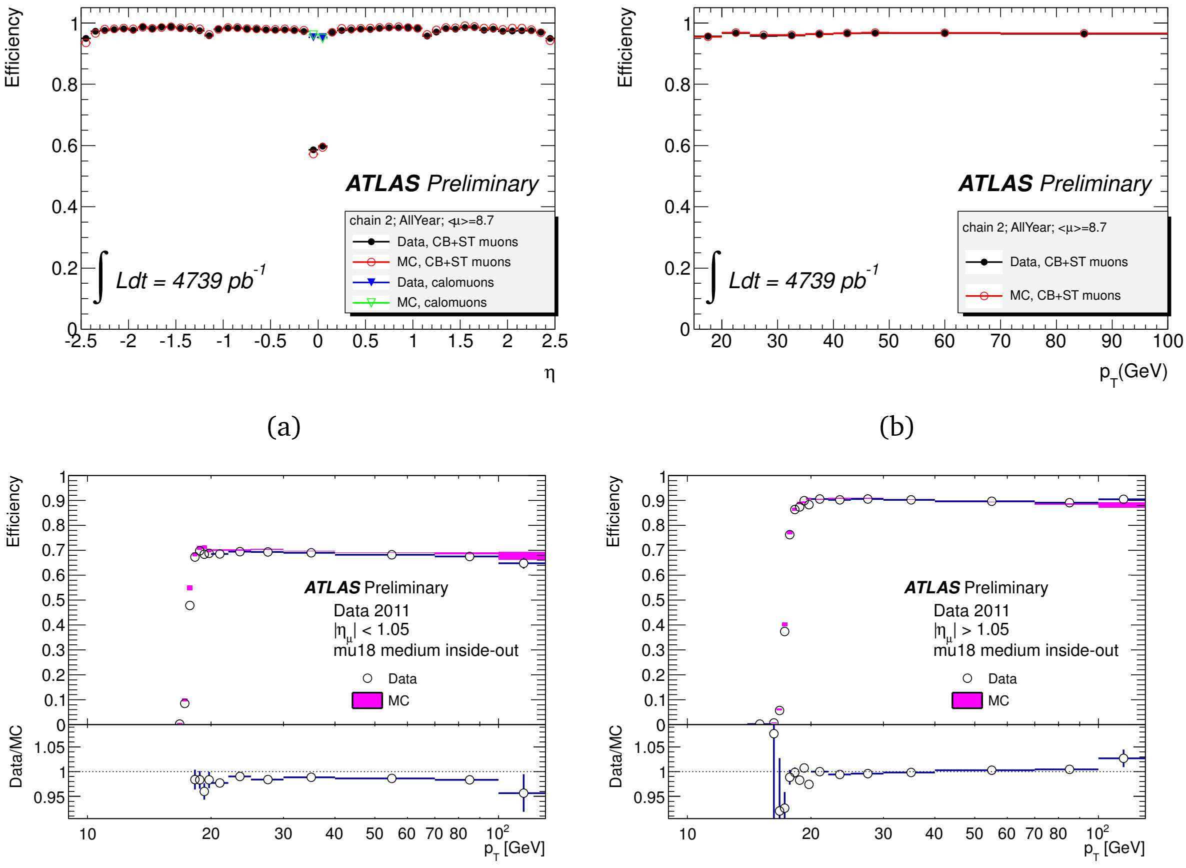

(a) (b)

(c) (d)

Figure 4.7: Top row: Muon reconstruction efficiency as a function of (a) $|\eta|$ and (b) p_{T} for Muid *tight* muons. The efficiency measured in data is shown and compared with the simulation [43]. Bottom row: Event filter muon trigger efficiency with respect to isolated offline muons measured in data and compared with the simulation. For muons in the (c) barrel region, $|\eta| < 1.05$, and (d) end cap region, $|\eta| > 1.05$ [43].

inefficiency is well modelled by the simulation, with relative difference to the data of less then 2%.

4.5.3 Trigger efficiency

The muon trigger efficiency is also measured in data with a tag-and-probe method using $Z \to \mu^+\mu^-$ decays. The efficiency of the event filter trigger with respect to isolated offline muons is about 70% in the barrel region and 90% in the forward region, for muons with p_{T} above 18.5 GeV [34]. The lower efficiency in the barrel is mostly a consequence of reduced coverage of the trigger chambers. The event filter trigger efficiency as a function of p_{T} for muons in the barrel region and in the end cap region is shown in Fig. 4.7. The trigger efficiency is flat for $p_{\mathrm{T}} > 20\,\mathrm{GeV}$ and an efficiency of 95% of the plateau efficiency is reached at $p_{\mathrm{T}} = 18.1\,\mathrm{GeV}$ in both the barrel and endcap regions. The trigger efficiency is well modelled by the simulation, with a relative difference to the data of less then 2%.

Chapter 5

Data set, simulated event samples and event selection

The selection of $Z \to \mu^+\mu^-$ events is based on the measurement of two high p_T muons, with the data recording being triggered by the presence of at least one high p_T muon. This chapter presents first the data set and simulated signal and background samples and then the selection criteria. In the following the background estimation and corrections applied to MC samples are discussed.

5.1 Data set

The LHC has delivered proton-proton collisions at $\sqrt{s} = 7\,\mathrm{TeV}$ starting in March 2010. In 2011 the instantaneous luminosity was increased, and during that year the LHC delivered an integrated luminosity of $5.6\,\mathrm{fb}^{-1}$ [44], compared with $48\,\mathrm{pb}^{-1}$ in 2010. The measurement of this thesis uses the data set collected with the ATLAS detector in 2011. The earlier data from 2010 are not included for more consistent treatment of the data due to changing detector conditions and pileup from 2010 to 2011.

Further, only data are used that were taken during stable beam conditions, and with fully operating magnet system and tracking and calorimeter subdetectors as defined by the ATLAS data quality group. These conditions allow good quality track and muon reconstruction that is necessary for this measurement. In addition, quality requirements for electron, jet and missing transverse energy reconstruction are applied in order to define a common data set for all measurements of W and Z production with ATLAS. The luminosity of the data sample taking into account these requirements is $4.7\,\mathrm{fb}^{-1}$ [45].

5.2 Simulated samples

Simulated event samples are used to estimate the acceptance, selection efficiency, resolution effects and to estimate the backgrounds. Moreover the measured differential cross-section is compared to the predictions from simulations. The main $Z \to \mu^+\mu^-$ signal sample is simulated using the POWHEG event generator [46] in combination with the PYTHIA parton shower [47] and using the CT10 parton distributions [18]. Further signal samples, simulated with PYTHIA using the MRST LO* PDF set [47, 48] and MC@NLO [49] in combination with the parton shower from HERWIG [50], are used to study systematic uncertainties.

Simulated samples are also used to study the background contributions. Events from the following processes contribute as background to the $Z \to \mu^+\mu^-$ selection [51]:

- $W \to \mu\nu$: a small contribution is expected from this process from events with associated jet production, where the other reconstructed muon originates from a jet.
- $Z \to \tau^+\tau^-$: this process contributes as background when both taus decay into muons.
- $t\bar{t}$ production: this process contributes through final states containing two muons, where the muons result from the W decays or semi leptonic charm or bottom decays.
- WW and WZ production: decays into muons contribute as background, where muons originate directly from W or Z decays but also from semi leptonic charm or bottom decays.
- ZZ production: these events are also considered as background since the transverse momentum is mostly not due to the dynamics of QCD.
- $W \to \tau\nu$: similar to the $W \to \mu\nu$ process a small contribution is expected from this process from events with associated jet production, where a muon is reconstructed originating from the jet and the tau decays into a muon.
- QCD: processes with semi-leptonic decays of heavy quarks and hadrons misidentified as leptons contribute as background. Simulated for this are samples of $c\bar{c}$ and $b\bar{b}$ production.

The $W \to \mu\nu$, $Z \to \tau^+\tau^-$, $c\bar{c}$ and $b\bar{b}$ background processes are simulated using the PYTHIA generator. The $t\bar{t}$ process is simulated with MC@NLO [52], and the WW, WZ, ZZ processes are simulated with HERWIG [53]. The $W \to \tau\nu$ background process is simulated with ALPGEN [54].

A summary of all samples used is listed in Table 5.1. The $Z \to \ell^+\ell^-$, $W \to \ell\nu$, $t\bar{t}$, WW, WZ, ZZ samples are normalised to their respective cross sections calculated at NLO and NNLO following the procedure given in [51] and [55, 56]. The $Z \to \ell^+\ell^-$, $W \to \ell\nu$ samples are normalised to the cross sections calculated at NNLO with the FEWZ program [57, 58] with MSTW 2008 NNLO PDFs [20]. A total uncertainty of 5% is assigned on the cross section, coming from the choice of PDF set (3%) and from factorisation and renormalization scale dependence. The cross section for $t\bar{t}$ production, calculated at approximated NNLO, is assigned a 6% uncertainty. The cross sections for the WW, WZ, ZZ processes were calculated with FEWZ at NLO. They have about 7% uncertainty.

To simulate the effect of QED final state radiation all generators are interfaced to PHOTOS [59]. The interaction of the generated particles with the sensitive and insensitive parts of the ATLAS detector is simulated using a detailed detector model implemented in GEANT 4 [60, 61].

Depending on the instantaneous luminosity each bunch crossing causes on average up to 17 inelastic pp interactions (pileup). To include this effect, simulated minimum bias events are overlayed with the signal and background events in the simulated samples. These minimum bias events are simulated with PYTHIA.

Table 5.1: MC samples used in the analysis for estimating the background and to correct data for detector effects.

Process	Generator	Dataset ID	Reco ID	Events	$\sigma \times BR\ [nb]$
$Z \to \mu^+\mu^-$	Pythia	106047	r3043	$10 \cdot 10^6$	0.99 ± 0.05
$Z \to \mu^+\mu^-$	Powheg +Pythia	108304	r3043	$20 \cdot 10^6$	1.02 ± 0.05
$Z \to \mu^+\mu^-$	Mc@nlo	106088	r3043	$5 \cdot 10^6$	0.99 ± 0.05
$W \to \mu\nu$	Pythia	106044	r3043	$7 \cdot 10^6$	10.46 ± 0.52
$Z \to \tau^+\tau^-$	Pythia	106052	r3060	$1 \cdot 10^6$	0.99 ± 0.05
$t\bar{t}$	Mc@nlo	105200	r3043	$15 \cdot 10^6$	0.16 ± 0.01
WW	Herwig	105985	r3043	$2.5 \cdot 10^6$	$(44.9 \pm 0.3) \times 10^{-3}$
WZ	Herwig	105987	r3043	$1 \cdot 10^6$	$(18.5 \pm 0.1) \times 10^{-3}$
ZZ	Herwig	105986	r3043	$0.25 \cdot 10^6$	$(6.0 \pm 0.04) \times 10^{-3}$
$W \to \tau\nu$	Alpgen	107700-05	r3043	$12.3 \cdot 10^6$	10.5
$b\bar{b}, \geq 1\mu, p_\mu > 15\,\mathrm{GeV}$	Pythia	108405	r3043	$4.5 \cdot 10^6$	73.9
$c\bar{c}, \geq 1\mu, p_\mu > 15\,\mathrm{GeV}$	Pythia	106059	r3043	$1.5 \cdot 10^6$	28.4

5.2.1 Corrections to the simulation

Despite the great level of detail of the simulation it suffers from certain shortcomings. For one, the knowledge of the event generation process is not perfect, for instance due to non perturbative effects. On the other hand, the detector model is not perfect. Temporary detector malfunctions are not simulated correctly. The relative positions of the detector elements (alignment) are known within some uncertainty, and ground movement might cause a change in them. All these effects may lead to differences between the simulation and data. These differences can be minimised by applying weights to simulated events to correct for individual uncorrelated effects.

Z boson p_T reweighting

The p_T spectrum of the Z boson in the default signal MC sample Powheg shows a systematic shift to higher p_T values compared with the data in the region around 10 GeV where the peak of the cross section is. A much better agreement is found with the Pythia generator in the MC10 tune. Therefore, the events in the signal sample are reweighted in order to recover the Z boson p_T spectrum of Pythia MC10. A comparison of detector level shapes for data, original MC and weighted MC is shown in Fig. 5.1. The original distribution shows a disagreement with respect to data of up to ~20% in the first 2 bins, which is reduced to ~10% after reweighting to the p_T distribution of Pythia MC10.

Pileup reweighting

The data taking periods of 2011 feature different instantaneous luminosity profiles and different detector conditions. The different detector and pileup conditions are simulated, but not for the correct integrated luminosity. Therefore the simulated samples are reweighted to match the integrated luminosity per period of identical detector conditions and to match

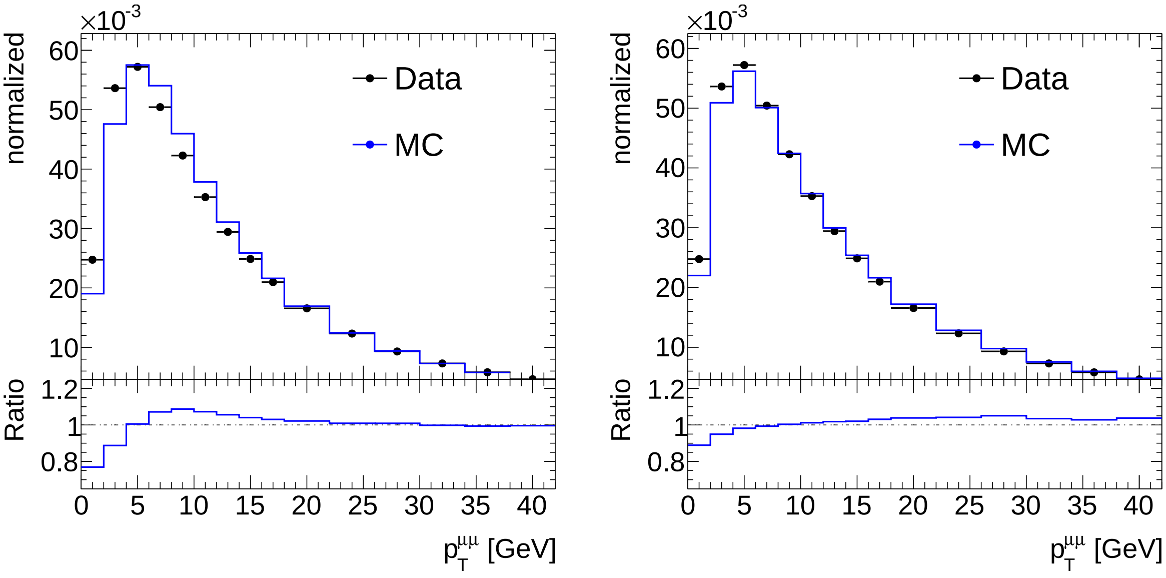

(a) (b)

Figure 5.1: Comparison of the Z boson transverse momentum distribution for data and the signal sample (a) standard POWHEG, and (b) POWHEG after reweighting to the p_{T} distribution predicted by PYTHIA MC10. Both distributions are normalised to one.

the average number of simultaneous interactions, $<\mu>$, observed in data.

Muon momentum scale and resolution correction

The modelling of the detector resolution is central to this measurement. Any remaining misalignment of the tracking detectors leads to a degradation of the muon momentum resolution and can introduce a shift of the momentum scale. Correction values as a function of muon η and p_{T} are determined from a measurement of the muon momentum resolution and scale in data, as described in Section 4.5.1. To correct for scale differences, $1/p_{\mathrm{T}}$ is shifted; to correct for resolution differences $1/p_{\mathrm{T}}$ is altered by a Gaussian distributed random value. Since the resolution and scale differences are not the same for the ID and MS measurement these corrections are applied differently for the two components. The final correction is a statistical combination of the two, where the components are weighted according to their relative resolution. Moreover, different corrections are applied to negatively and positively charged muons. The effect of the scale and resolution corrections on the invariant mass distribution is shown in Fig. 5.2. The correction leads to much improved agreement of the line shape. The effect of the correction on the Z boson transverse momentum distribution is about 5% as shown in Fig. 5.3.

Muon efficiency correction

Inefficiencies in the muon reconstruction are due to the combination of detector coverage, hit efficiencies, hit resolution and the combination of the measurement of different

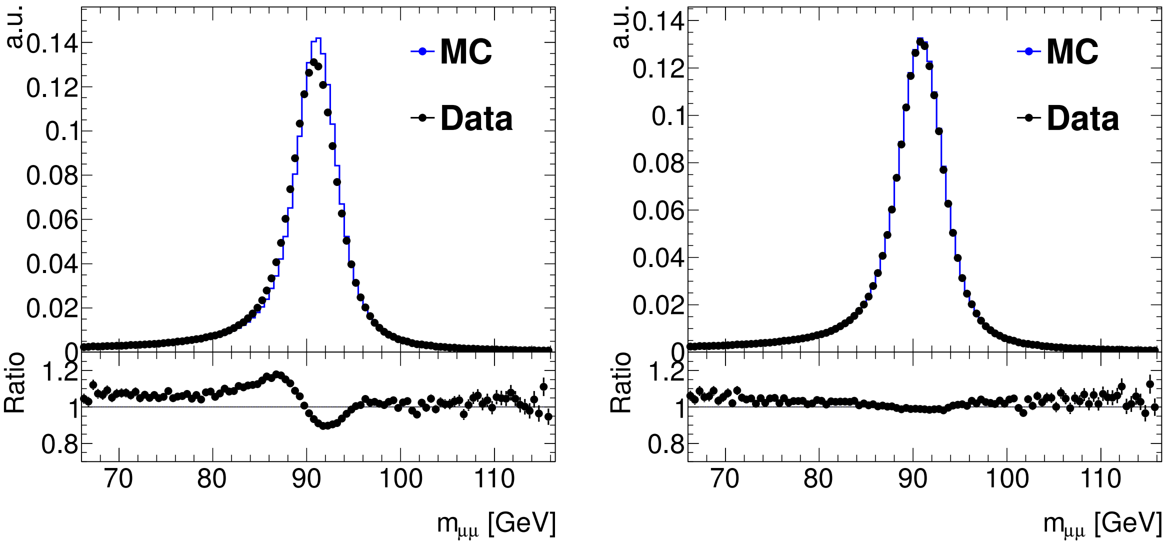

(a)

(b)

Figure 5.2: Comparison of the Z boson line shape for data and signal MC. Both distributions are normalised to unity, in order to compare shapes. (a) Comparison without applying the scale and resolution corrections. (b) Comparison with the corrections applied.

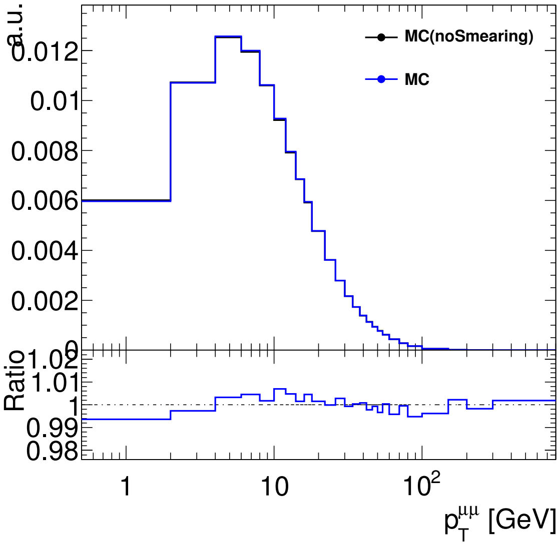

Figure 5.3: Effect of the muon momentum scale and resolution correction on the Z boson p_{T} distribution.

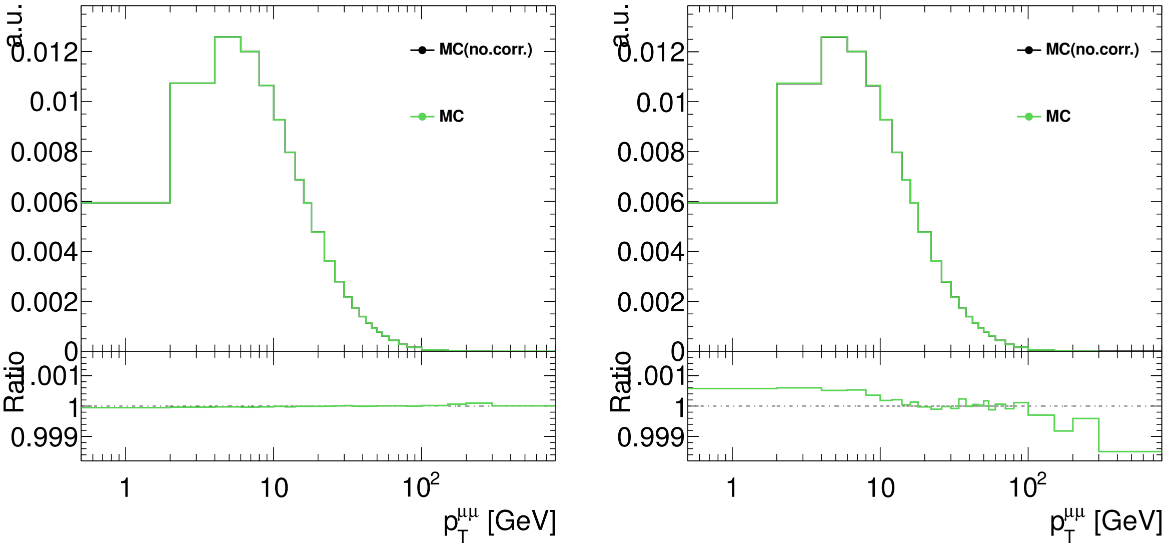

(a) (b)

Figure 5.4: Effect of applying efficiency correction to the simulation on the Z boson p_{T} distribution when applying (a) the muon reconstruction efficiency weights and (b) the trigger efficiency weights. Each time, only one type of weight is applied.

subdetectors. The offline muon reconstruction efficiency and trigger efficiency have been measured in data, as described in Section 4.5.2. The measured muon efficiencies are well modelled by simulation. Nevertheless, small differences of order 1% remain. They are corrected by applying event weights for each muon as a function of its reconstructed η and ϕ. The effect of the corrections on the Z boson p_{T} distribution is smaller than 0.1%, as shown in Fig. 5.4.

5.3 $Z \rightarrow \mu^+\mu^-$ event selection

The selection of $Z \rightarrow \mu^+\mu^-$ events is based on the measurement of two high p_{T} muons. To trigger the data recording the presence of at least one high p_{T} muon is sufficient. The event selection criteria follow those used for previous measurements of the Z boson cross section at ATLAS [1, 51], with small changes to adapt for the increased p_{T} thresholds of the single muon triggers and the increased instantaneous luminosity.

5.3.1 Trigger selection

The trigger required is the single muon trigger with the lowest p_{T} threshold for which all events could be recorded for the run period. Two different triggers are used, both with a threshold of $p_{\mathrm{T}} = 18\,\mathrm{GeV}$. The trigger for data periods B to I is `EF_mu18_MG`; for data periods J to M it is `EF_mu18_MG_medium`. Both triggers are based on muons reconstructed with the MuGirl algorithm, requiring a track in the inner detector matching a track segment

Table 5.2: Summary of event selection criteria.

Trigger	`EF_mu18_MG`(Periods B-I) `EF_mu18_MG_medium`(Periods J-M)
Event cleaning	One primary vertex with ≥ 3 tracks $\lvert z_{\mathrm{vtx}} \rvert < 200\,\mathrm{mm}$
Muon selection	Combined plus segment tagged muons (Muid tight) $p_{\mathrm{T}} > 20\,\mathrm{GeV}$ $\eta < 2.4$ Track based isolation $\sum p_{\mathrm{T}}/p_{\mathrm{T}}^{\mu} < 0.1$ in cone of $\Delta R < 0.2$ Track quality cuts
$Z \to \mu^+\mu^-$ selection	Exactly two muons Muons oppositely charged $66\,\mathrm{GeV} < m_{\mu\mu} < 116\,\mathrm{GeV}$

in the internal muon trigger chambers. They differ only in the seeding L1 trigger, `L1_MU10` for `EF_mu18_MG` and `L1_MU11` for `EF_mu18_MG_medium`, with thresholds of $p_{\mathrm{T}} = 10\,\mathrm{GeV}$ and $p_{\mathrm{T}} = 11\,\mathrm{GeV}$. Apart from the different p_{T} thresholds the first L1 trigger is based on a two station coincidence, while the second is based on a three station coincidence [34]. The trigger efficiency with respect to isolated offline muons is measured in data to be about 70% in the barrel region and 90% in the forward region in the plateau $p_{\mathrm{T}} > 20\,\mathrm{GeV}$ (see Section 4.5.2). Being able to use a single muon trigger is of advantage, because the efficiency to trigger events with 2 offline muons is close to 100%.

5.3.2 Event selection

For this analysis, only events with a reconstructed primary vertex with at least three associated tracks are considered in order to reject pure cosmic-ray and beam halo background. The vertex position is required to be close in z to the nominal interaction region, $\lvert z_{\mathrm{vtx}} \rvert < 200\,\mathrm{mm}$. $Z \to \mu^+\mu^-$ events are selected by requiring two oppositely charged muons with an invariant mass close to the Z boson mass: $66\,\mathrm{GeV} < m_{\mu\mu} < 116\,\mathrm{GeV}$. The muon acceptance is limited to $p_{\mathrm{T}} > 20\,\mathrm{GeV}$ in order to match the threshold of the trigger, and to $\lvert\eta\rvert < 2.4$ which is given by coverage of the trigger chambers. The muons are reconstructed from matching tracks in the inner detector and the muon system (Muid *tight*, see Section 4.3) and have to pass some additional quality requirements that ensure good momentum measurement which are described in Section 5.3.3. Further, the muons are required to be isolated in order to suppress background from pion, kaon and heavy flavor decays [62]. The isolation requirement uses the sum of transverse momenta of tracks with $p_{\mathrm{T}} > 1\,\mathrm{GeV}$ within a cone of size $\Delta R = 0.2$ around the muon track. Requirements on the muons' impact parameters d_0, z_0 and their difference $\Delta d_0, \Delta z_0$ further ensure that both muons originate from the same hard interaction. Events with more than two selected muons are vetoed. All selection criteria are summarised in Table 5.2.

5.3.3 Muon track quality requirements

In order to ensure an accurate momentum measurement, the following properties are required of the inner detector track of all muons [38]:

- A pixel B-layer hit on the track, *except* the extrapolated muon track passes an uninstrumented or dead area of the B-layer
- Number of pixel hits+number of crossed dead pixel sensors > 1.
- Number of SCT hits+number of crossed dead SCT sensors > 5.
- Number of pixel holes + number of SCT holes < 3.
- A successful TRT extrapolation where expected in the η acceptance of the TRT. An extrapolation is classified as unsuccessful, if either no TRT hits can be associated with the track, or the associated TRT hits are classified as outliers by the track fit. The technical definition is the following:
- Let nTRThits denote the number of TRT hits on the muon track, nTRToutliers the number of TRT outliers on the muon track, and n = nTRThits + nTRToutliers
  - Case 1:$|\eta| < 1.9$. Require $n > 5$ and nTRToutliers $< 0.9n$.
  - Case 2: $|\eta| \geq 1.9$. If $n > 5$, then require nTRToutliers $< 0.9n$.

5.3.4 Result of the selection

A total of 1.8 million $Z \rightarrow \mu^+\mu^-$ candidate events are selected in data. The number of events passing the selection cuts is listed in Table 5.3. The distributions of p_T, η, ϕ of muons as well as the isolation variable in the selected events are shown in Figure 5.5. The figure also contains the background expectation, even though it is so small as to be barely visible. The background estimation will be described in the next section. The agreement between data and simulation is very good. The same holds for the distributions of the transverse and longitudinal impact parameters which are shown in Figure 5.6. The raw transverse momentum distribution of the selected Z boson candidates and the invariant mass distribution are shown in Figure 5.7.

5.4 Backgrounds

The event selection presented in Section 5.3 leads to a very pure Z boson sample. It contains a background contribution of less then 0.5%, which is composed of $t\bar{t}$, $Z \rightarrow \tau^+\tau^-$, WW, WZ, ZZ, $W \rightarrow \tau\nu$, $W \rightarrow \mu\nu$ and QCD processes. The contribution from QCD events is estimated from data, as described in the following section. The number of background events after selections is listed in Table 5.4.

Table 5.3: Number of events in 2011 data passing the event selection cuts. The first entry refers to the size of the data sample used for the study. The data sample contains only events with at least two 17 GeV muons, or a pair of a 17 GeV muon and a 17 GeV charged particle track measured by the inner detector, or a W boson candidate event. The definition of the cuts is given in Section 5.3.

Cut name	Number of events
Skim	80957248
Trigger	71034584
Vertex	70933696
Muid Tight	13401361
Track Quality	11321909
d_0	10926810
z_0	9487652
p_T	2388251
η	2265385
Isolation	1950033
Opposite charge	1948688
Invariant mass	1817107
Δd_0	1817107
Δz_0	1817050
veto extra muons	1816817
Trigger match	1816784

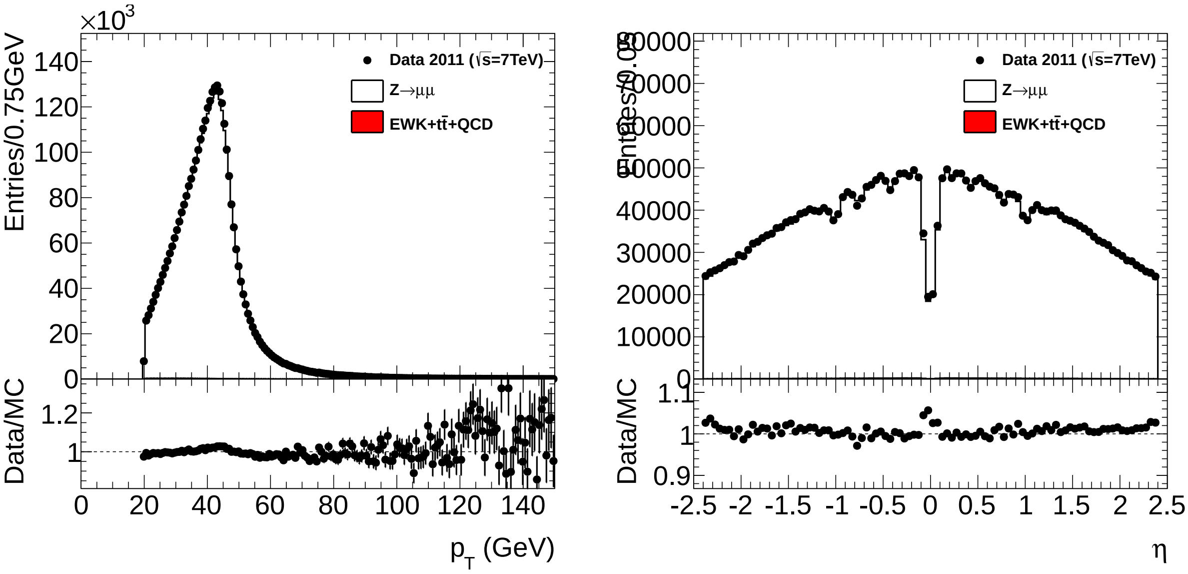

(a) p_{T} of muons

(b) η of muons

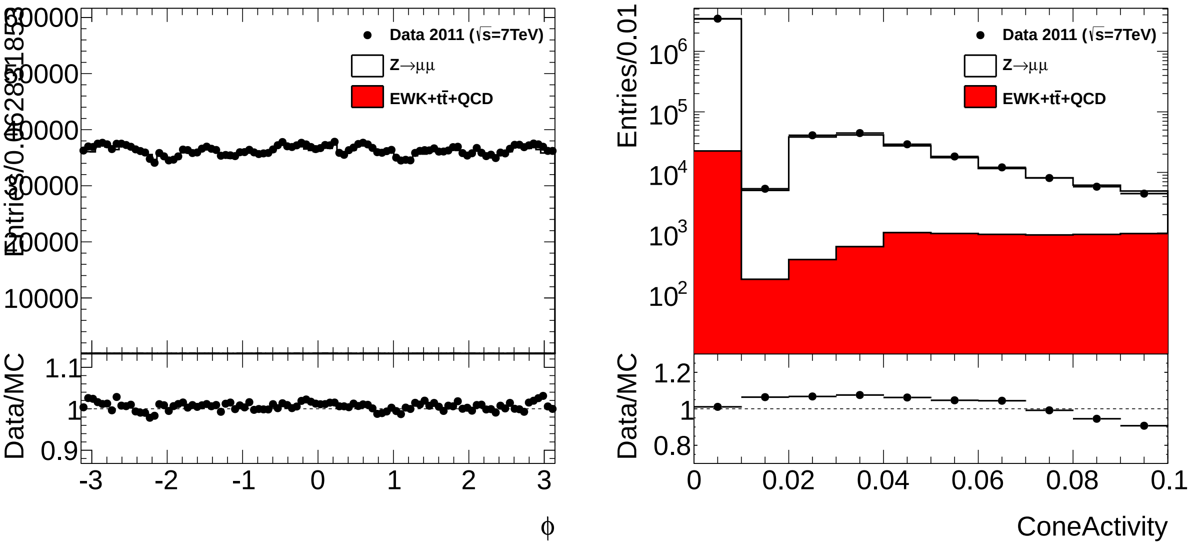

(c) ϕ of muons

(d) Isolation $\sum p_{\mathrm{T}}/p_{\mathrm{T}}^{\mu}$ in cone of $\Delta R < 0.2$

Figure 5.5: Kinematic distributions of the muons in the selected $Z \to \mu^+\mu^-$ events. The background from electroweak processes ($W \to \mu\nu$, $W \to \tau\nu$, $Z \to \tau^+\tau^-$, WW, WZ, ZZ), $t\bar{t}$ production and QCD production are contained in the figures.

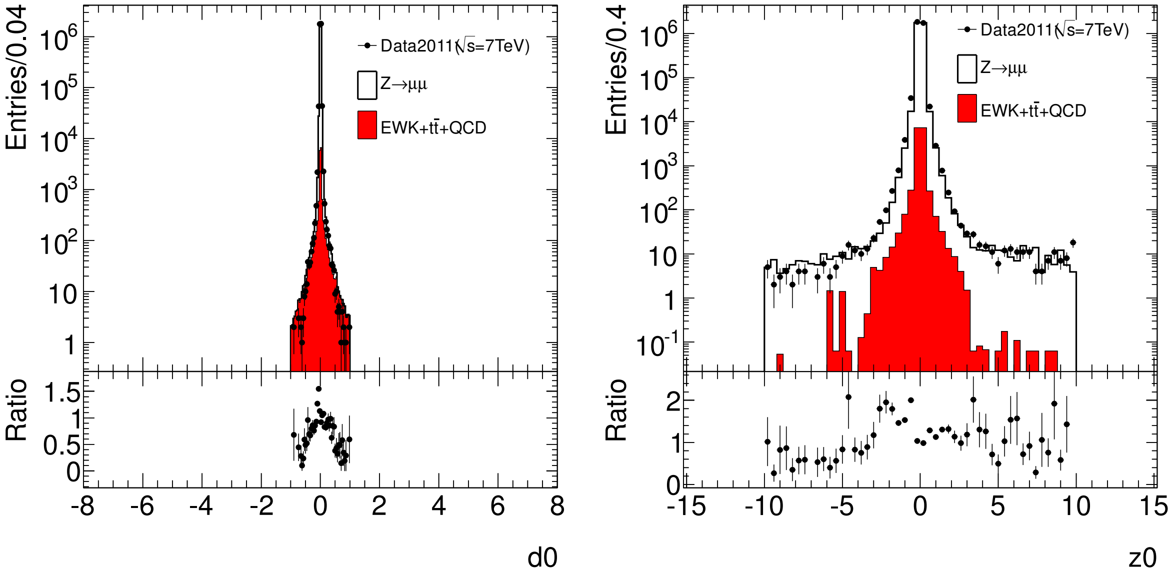

(a) d_0 of muons

(b) z_0 of muons

Figure 5.6: Impact parameter distributions of the muons in the selected $Z \to \mu^+\mu^-$ events. The background from electroweak processes ($W \to \mu\nu$, $W \to \tau\nu$, $Z \to \tau^+\tau^-$, WW, WZ, ZZ), $t\bar{t}$ production and QCD production are contained in the figures.

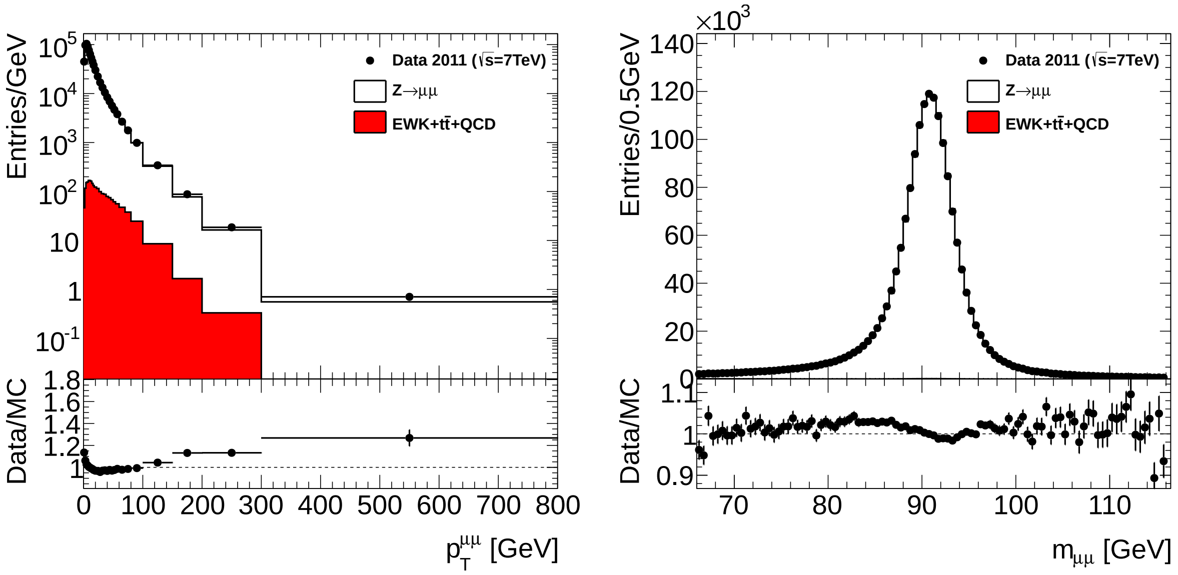

(a)

(b)

Figure 5.7: Distribution of the selected Z boson candidates in (a) transverse momentum, (b) invariant mass.

Table 5.4: Number of events in data and expected background. The electroweak background is estimated using MC samples and the QCD background using a data driven method.

Process	Number of events
Data	
1816777	
Expected Signal	
$Z \rightarrow \mu^+\mu^-$	1783196
Expected background	
$W \rightarrow \mu\nu$	131
$W \rightarrow \tau\nu$	16
$Z \rightarrow \tau^+\tau^-$	1230
$t\bar{t}$	1949
WW	474
ZZ	907
WZ	1273
QCD	1950
Total background	7931
Total expected	1791127

5.4.1 Estimation of the QCD background

Compared with the cross section of Z boson production, the cross section of inclusive jet production is about 4 orders of magnitude larger, while the total inelastic proton-proton cross section is even 9 orders of magnitude larger. Fortunately the selection of two high p_{T} muons significantly reduces this type of background since the thickness of the calorimeter efficiently shields the muon system from particles other than muons. The source of real muons in QCD events are heavy flavour decays as well as pion and kaon decays [62, 63]. The hadrons do not necessarily decay close to the primary vertex, but the impact parameters may still satisfy the requirements listed in Section 5.3.

The contribution of this background is not sufficiently well modelled in the simulation, because not all sources are included, but also because of a considerable uncertainty on the production cross sections. Furthermore, a large fraction of these events are rejected by the reconstruction and selection cuts, which means that very large simulated samples would be needed to obtain statistical precision. Therefore this background is estimated using control regions in data. Two ways of defining the control regions are studied to estimate the systematic uncertainty, similar to the procedure used in Ref. [1].

2-dimensional side-band method

The normalisation of the QCD background is determined from the number of events in three control regions and the signal region which are defined as:

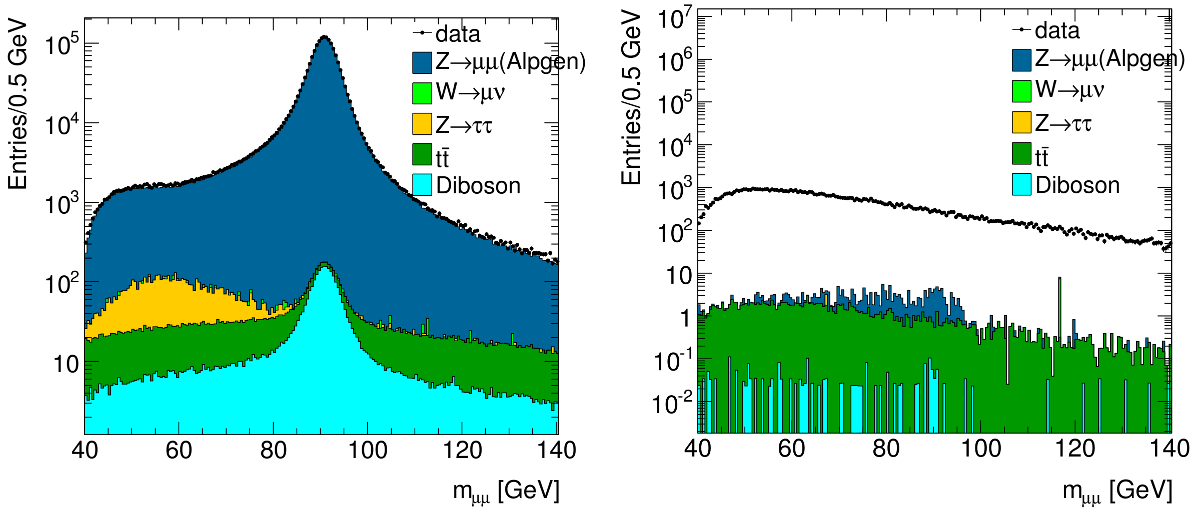

(a) (b)

Figure 5.8: Invariant mass distribution for a) isolated and b) non-isolated muon pairs.

Region A (signal region): $66\,\text{GeV} < m_{\mu\mu} < 116\,\text{GeV}$, isolated
Region B : $47\,\text{GeV} < m_{\mu\mu} < 60\,\text{GeV}$, isolated
Region C : $66\,\text{GeV} < m_{\mu\mu} < 116\,\text{GeV}$, non-isolated
Region D : $47\,\text{GeV} < m_{\mu\mu} < 60\,\text{GeV}$, non-isolated

where non isolated means the inversion of the track based muon isolation cut defined in Section 5.3, $\sum p_{\mathrm{T}}/p_{\mathrm{T}}^{\mu} > 0.1$ in a cone of $\Delta R < 0.2$ around the muon. Regions C and D are largely dominated by the QCD background and only suffer a tiny contamination from other background and signal events (see Fig. 5.8). To first order, the properties of the QCD background, other than the isolation variable itself, do not depend on the isolation variable. Therefore, the relative number of QCD events, n_{QCD}, in regions A over B and C over D are identical, and can be used to extract the number of events in the signal region:

$$n_{\mathrm{QCD}}^{\mathrm{A}} = n_{\mathrm{QCD}}^{\mathrm{B}} \times n_{\mathrm{QCD}}^{\mathrm{C}} / n_{\mathrm{QCD}}^{\mathrm{D}} \,. \tag{5.1}$$

The number of QCD events in regions B, C, D is obtained from the observed number of events by correcting for the expected contribution of the other backgrounds and the signal events. The normalisation of the $Z \rightarrow \mu^+\mu^-$ signal and the other backgrounds is taken from the signal region, A, taking into account the QCD contribution and extrapolated to the other regions using relative efficiencies which are taken from simulation. The number of QCD events in the signal region is:

$$n_{\mathrm{QCD}}^{i} = n^{i} - c^{i}(n^{\mathrm{A}} - n_{\mathrm{QCD}}^{\mathrm{A}}) \,,\; i = \mathrm{B}, \mathrm{C}, \mathrm{D} \,, \tag{5.2}$$

Table 5.5: Number of observed events in regions A, B, C and D of the 2-dimensional side-band method.

Region	Data	Signal	Electroweak	c_i
A	1821455	1731652	5803	
B	41327	35073	2673	0.0217
C	31101	110	80	1.1×10^{-4}
D	22284	15	48	3.5×10^{-5}

where n^i is the number of events observed in region i, and c^i is the relative efficiency for the signal and the other backgrounds:

$$c^i = n^i_{\text{signal+EWK}} / n^{\text{A}}_{\text{signal+EWK}}, i = \text{B}, \text{C}, \text{D} \ . \tag{5.3}$$

The resulting equation can be solved for the number of QCD events in region A, in terms of the observed number of events, which are given in Table 5.5. The number of QCD events was estimated as 2500 ± 370 events, or $0.14 \pm 0.02\%$, where the uncertainty is the statistical uncertainty only.

Same sign method

The production of same sign muon pairs is dominated by QCD production, and can be used to normalise this background in the signal region. As was shown in Ref. [62], most of the high p_{T} muon background originates from heavy flavor decays. The ratio of same-sign to opposite-sign muon pairs in the QCD background can be therefore taken from the PYTHIA heavy flavor samples. The value for the ratio is 4.1 ± 0.5, where the uncertainty is the statistical uncertainty only. The number of same sign muon pairs observed in data is 446, keeping all other selection requirements, compared with 106 events which are expected from the signal and electroweak background processes. This resulting estimate for QCD events in the signal region is thus 1400 ± 180 events.

Summary QCD background

The QCD background contribution is found to be 2500 ± 370 events with the 2-dimensional side-band method, and 1400 ± 180 events with the same sign method. No systematic uncertainties are explicitly assigned to the two methods, but the average is taken as the QCD background normalisation and the difference is considered as systematic uncertainty. Given the small relative size of this background, this is a sufficiently good estimation. The shape of the QCD background was obtained from the non isolated control region. Figure 5.9 shows the invariant mass and p_{T} distributions after the $Z \rightarrow \mu^+\mu^-$ selection, including the contribution from the QCD background.

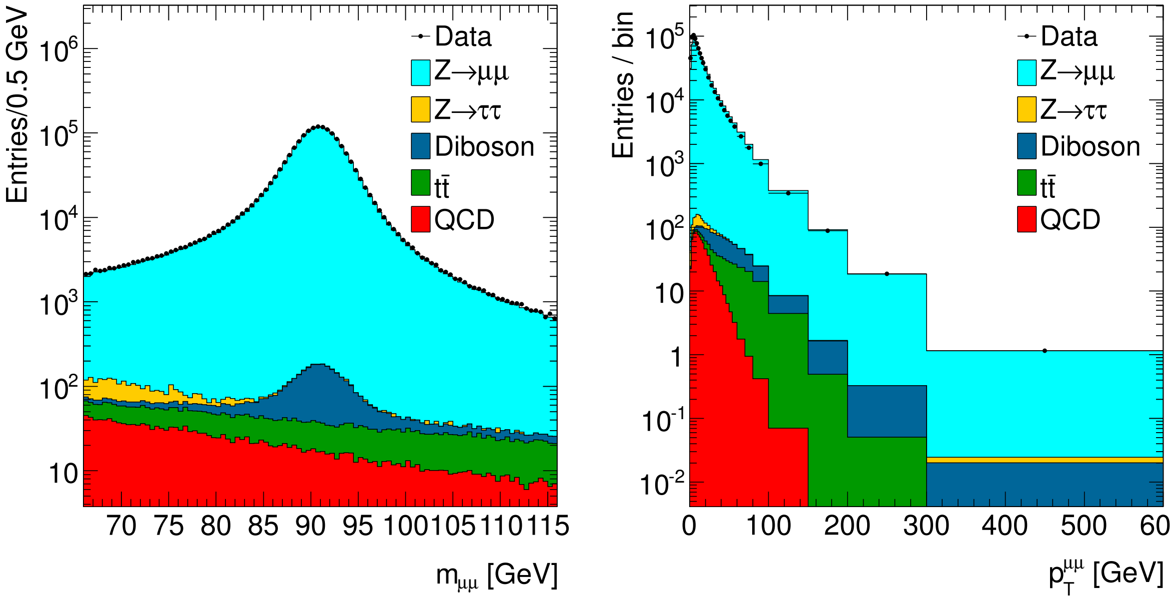

(a) Invariant mass $m_{\mu\mu}$

(b) Transverse momentum $p_{\mathrm{T}}^{\mu\mu}$

Figure 5.9: Z candidate distributions showing data, simulated signal and backgrounds. The QCD background, labelled 'QCD' is the red filled histogram.

Chapter 6

Measurement of the differential cross section

This chapter describes the measurement of the normalised differential cross sections of the Z boson production using the sample of $Z \rightarrow \mu^+\mu^-$ events which was obtained as described in the previous chapter (Chapter 5).

6.1 Measurement strategy

The normalised transverse momentum distribution of Z bosons is measured, which is defined here as

$$\frac{1}{\sigma_{\text{fid}}} \times \frac{d\sigma_{\text{fid}}}{dp_{\text{T}}}, \tag{6.1}$$

where σ_{fid} is the measured inclusive cross section for $pp \rightarrow Z/\gamma^* + X$ multiplied by the branching fraction of $Z \rightarrow \mu^+\mu^-$. Furthermore, the transverse momentum distribution is measured in three regions of Z rapidity

$$\frac{1}{\sigma_{\text{fid},y}} \times \frac{d\sigma_{\text{fid}}}{dp_{\text{T}}dy}, \tag{6.2}$$

where $\sigma_{\text{fid},y}$ is the measured cross section in the respective rapidity region inclusive in transverse momentum.

In the normalised measurement, large contributions related to the absolute value of the cross section cancel in the systematic uncertainty. The luminosity uncertainty cancels completely, while efficiency uncertainties cancel partly. Further, the cross section is measured in the phase space region defined by the detector acceptance and the kinematic cuts of the experimental selection needed to suppress backgrounds. It is therefore free from the theoretical uncertainties that would be caused by the extrapolation to the full phase space. The phase space is defined by the muon pseudorapidity and transverse momentum and the dimuon invariant mass: $\eta_\mu < 2.4$, $p_{\text{T}}^{\mu} > 20\,\text{GeV}$, $66\,\text{GeV} < m_{\mu\mu} < 116\,\text{GeV}$.

The transverse momentum of the Z boson candidates is reconstructed from the sum of the 4-vectors of the decay muons. The measured p_{T} distribution is therefore distorted by resolution effects, inefficiencies in the muon reconstruction and by QED final state

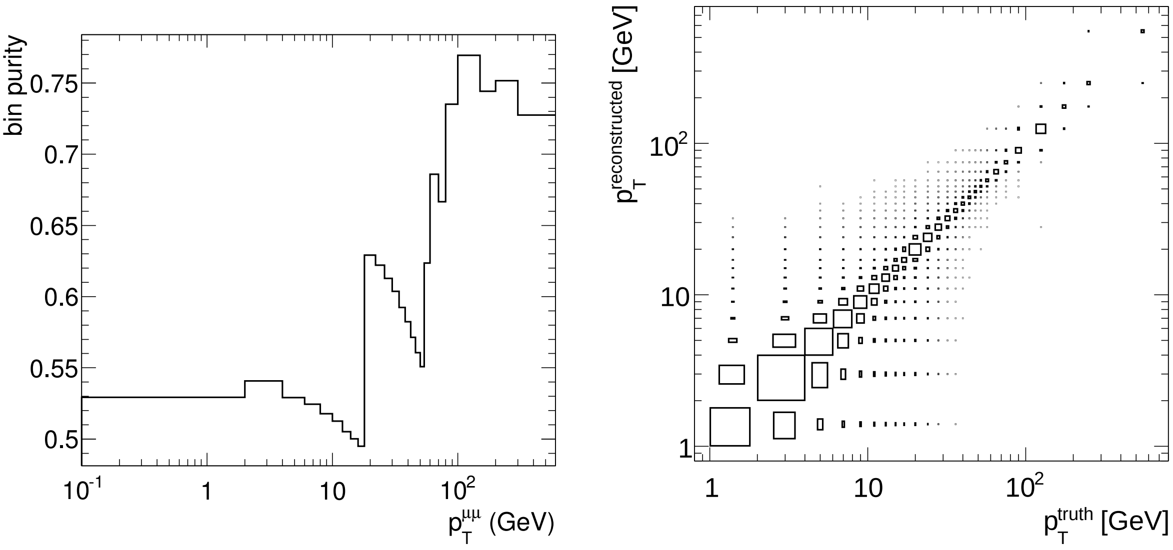

(a) (b)

Figure 6.1: Migration effects in the binned Z boson p_{T} distribution obtained from $Z \to \mu^+\mu^-$ MC simulation. (a) Bin purity, the fraction of events in a measurement bin that were generated in the same bin. (b) Response matrix, showing the distribution of measured versus the true p_{T} values obtained from the Powheg $Z \to \mu^+\mu^-$ sample. The size of the boxes reflects the number of events in each region.

radiation. To correct for these effects, an unfolding procedure is applied, which is described in Section 6.3.

6.2 Binning

The transverse momentum distribution is measured up to 800 GeV divided into 26 bins. Due to the limited experimental resolution on p_{T}^{Z} the bin-to-bin migrations are important and can significantly distort the measured distribution with respect to the true distribution. If the migration effects are too dominant it is not possible to revert them and extract the underlying distribution. Therefore the bin sizes are chosen so that at least 50% of the events measured in each bin where generated in the same bin, as shown in Fig. 6.1a. The migrations between bins are shown in Fig. 6.1b. For $p_{\mathrm{T}} > 150$ GeV the bin size is limited by the available statistics. The chosen bins have width of 2 GeV up to 18 GeV, then 4 GeV from 18 GeV to 54 GeV, and further increasing up to 800 GeV. The small bin size at low p_{T} allows to resolve the shape of the peak of the p_{T} distribution. At low p_{T} the bin size also reflects the typical resolution of the detector. The binning allows a statistical precision of better than 1% up to 150 GeV.

The three regions in Z rapidity chosen are $0 < |y| < 1$, $1 < |y| < 2$ and $2 < |y| < 2.4$. The rapidity is limited to 2.4 due to the muon acceptance of the ATLAS detector. The different rapidity regions correspond to events with different values of momentum fraction of the original parton. Since the most significant change in the shape of the cross section is expected at large rapidity, the binning is chosen to isolate this bin. The measurement is repeated in each of the rapidity regions independently, meaning that no migrations between the y bins are considered.

6.3 Unfolding

As stated before, the measured p_{T} distribution is different from the *true* distribution due to the influence of finite detector resolution, inefficiencies in the reconstruction as well as of QED final state radiation. In order to be able to compare the measurement with theoretical predictions and other measurements these effects need to be corrected for. The process of estimating the *true* distribution of a physical quantity from a measured distribution is commonly referred to as 'unfolding'. Due to the random nature of the measurement process, unfolding presents a complex statistical problem. An overview of unfolding methods used in particle physics is given in Refs. [64, 65]. The following mathematical description of the unfolding problem uses the notation found in Ref. [65].

The measurement process that transforms a true value y into a measured value x, can be described by the response function $R(x|y)$, which gives the probability to measure value x for a given true value y. The response function depends only on the measurement process, but is independent of the true distribution. It is obtained in general from simulated event samples using a detailed simulation of the detector. The relation between a measured distribution $f_{\mathrm{meas}}(x)$ and a true distribution $f_{\mathrm{true}}(y)$ can be stated as

$$f_{\mathrm{meas}}(x) = \int R(x|y) f_{\mathrm{true}}(y) dy \quad . \tag{6.3}$$

Here the measured and true distributions are approximated by histograms $\mathbf{t} = (t_1, \ldots, t_M)$ and $\mathbf{m} = (m_1, \ldots, m_M)$, where each bin contains the expectation value of $f_{\mathrm{meas}}(x)$ and $f_{\mathrm{true}}(y)$ in the range of the bin. For this application, the bins are chosen according to Section 6.2. The response function R is approximated by a matrix R_{ij}. With these approximations Equation 6.3 becomes:

$$m_i = \sum_{j=1}^{N} R_{ij} t_j \quad . \tag{6.4}$$

where the sum runs over the number of bins, N. The response matrix is not anymore independent of the true distribution used to create it because the distribution of events inside the bin has some influence on the number of events that migrate across bin boundaries.

The most straightforward solution to the problem of unfolding would be to invert the response matrix and apply the inverse to the measurement histogram:

$$\mathbf{t} = R^{-1} \mathbf{m} \quad . \tag{6.5}$$

This requires that the inverse of the matrix exists and in order to get stable results, the numerical inversion has to be stable as well. Since the actual measurement, $\mathbf{n} = (n_1, \ldots, n_N)$

is subject to random fluctuations, the expectation values **m** can only be estimated with some error. That is the true distribution, **t** is estimated by

$$\hat{\mathbf{t}} = R^{-1}\mathbf{n} \quad . \tag{6.6}$$

This solution is the unbiased result with the smallest possible variance for $\hat{\mathbf{t}}$. However, if the migration effects between bins are large, the inverse of the response matrix has large off-diagonal elements, which leads to large negative correlations between neighbouring bins. As a result, the estimated true distribution has very large variances and oscillates from bin to bin. In effect the variances in estimating **m** from **n** are amplified when moving from **m** to **t**. This is the case even if the response matrix is known with absolute precision and can be inverted numerically. This behaviour is illustrated in Fig. 6.2, which shows the attempt at unfolding a flat distribution. The response matrix shown was constructed by assuming a Gaussian resolution. The bin size in this case is about twice the resolution, resulting in a bin purity of about 55%. A test sample is drawn from the uniform distribution, and submitted to the same smearing used to construct the response matrix. The unfolded distribution, which is the result of applying the inverted response matrix to the test sample smeared distribution, oscillates around the expected true distribution. Thus, although the solution is unbiased, it is not very useful.

Modifications of the matrix inversion method define regularisation procedures, that introduce a small bias into the solution in order to reduce the variances. One approach is to numerically limit the first or second derivatives of the distributions. Another approach is to enforce a smoothing by decomposing the response matrix, and ignoring the contributions responsible for fine structure. The choices of regularisation type and strength are however somewhat arbitrary and may bias the result. The different regularisation approaches were tested for a measurement of the W boson transverse momentum distribution at the LHC, but were rejected due to the difficulty in choosing the appropriate regularisation [66].

A very basic and much simpler approach, called bin-by-bin unfolding, reduces the response matrix to simple correction factors for each bin. Migration effects are therefore taken into account only indirectly. The method gives good results if migrations between bins are small, and if the simulated MC sample used to define the correction factors is close to the data, as is illustrated using the same toy model as before in Fig. 6.2c. The method is very stable by definition but its results are strongly biased towards the simulated distribution, unless the bin purity is close to 100%.

The unfolding problem can also be solved without explicit matrix inversion using iterative methods. The next section describes the iterative Bayesian unfolding which suffers less from the instabilities which may occur in the matrix inversion method.

6.3.1 Iterative unfolding using Bayes theorem

The unfolding problem can be solved also without explicit matrix inversion, through the use of Bayes theorem and iteration. The method is described in detail in Refs. [67, 68]. The method is implemented in the RooUnfold software package [69, 70] which is used in this

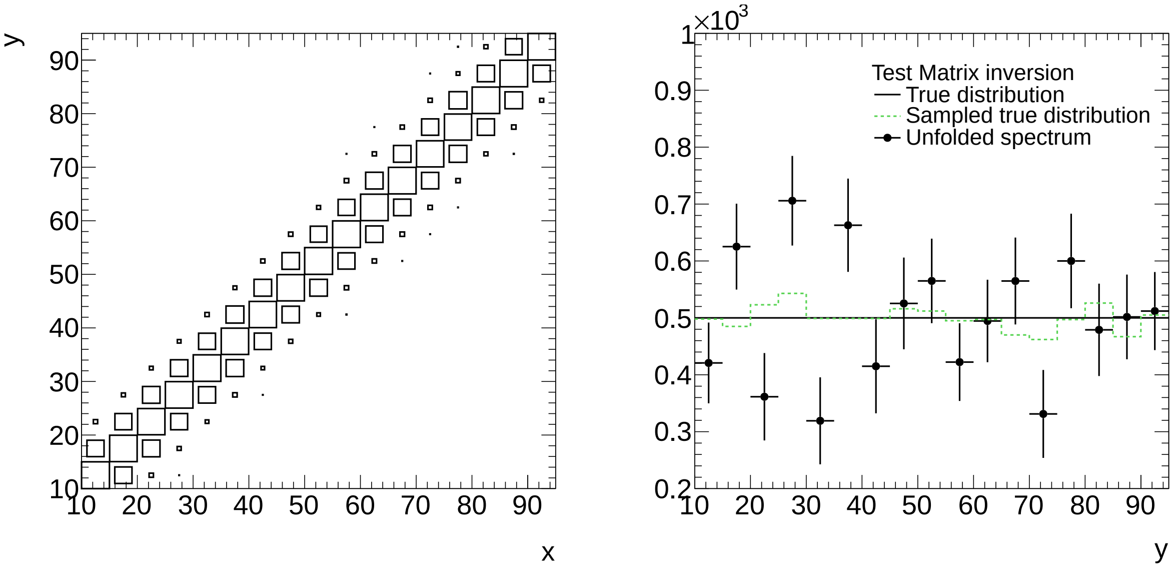

(a) Response matrix

(b) Unfolding by matrix inversion

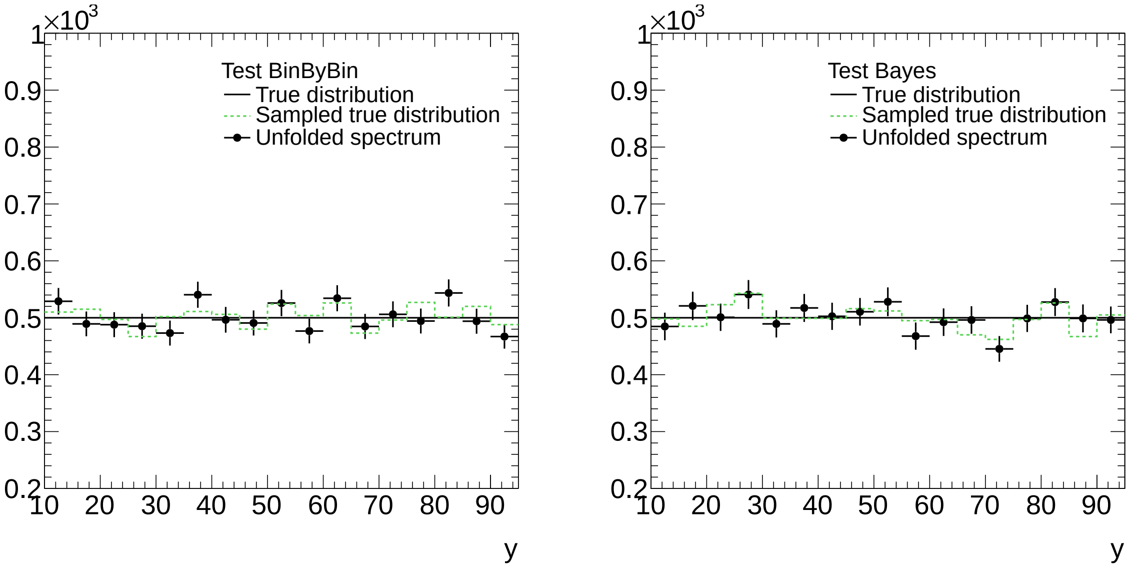

(c) Bin-by-bin correction

(d) Iterative Bayesian

Figure 6.2: Comparison of unfolding methods with a toy model. (a) Response matrix, from Gaussian smearing with $\sigma = 3$. (b) - (d) Comparison of the unfolded distribution (points) with the sampled true distribution (dashed line) and the underlying true distribution (solid line)

measurement. In the iterative unfolding equation 6.4 is considered in terms of probabilities:

$$m_i = \sum_{j=1}^{N} P(\text{meas in bin } i \mid \text{truth in bin } j)\, t_j \quad , \tag{6.7}$$

where the response matrix is interpreted as the probability $P(\text{meas in bin } i \mid \text{truth in bin } j)$. The expected true distribution can be expressed as:

$$\hat{t}_i = \sum_{j=1}^{N} P(\text{truth in bin } i \mid \text{meas in bin } j)\, m_j \quad . \tag{6.8}$$

The conditional probability $P(\text{truth in bin } i \,|\, \text{meas in bin } j)$, can be inverted using Bayes theorem:

$$P(\text{truth in bin } i \,|\, \text{meas in bin } j) = \frac{P(\text{meas in bin } j \,|\, \text{truth in bin } i)\, P_0(\text{truth in bin } i)}{\sum_{l=1}^{n_T} P(\text{meas in bin } j \,|\, \text{truth in bin } l)\, P_0(\text{truth in bin } l)} \quad ,$$

where the probabilities $P(\text{reconstructed in bin } j \,|\, \text{truth in bin } i)$ are equivalent to the response matrix, and $P_0(\text{truth in bin } i)$ is an initial probability, the prior. This means, that an initial assumption about the true spectrum is required. This initial assumption is updated by the measurement, and in successive iterations $P_0(\text{truth in bin } i)$ is replaced by the true spectrum which results from Eq. 6.8. This method usually is reasonably close to the true spectrum after a few iterations and mostly independent of the initial assumption for the true distribution. Since the statistical uncertainty increases with each iteration, there is a trade-off between the bias of the result and the statistical uncertainty. The optimum number of iterations depends on the problem and needs to be determined with toy experiments. A good prior to get fast convergence is to use a predicted spectrum, for example the prediction from a MC generator which is in good agreement with the data. The bias after n-iterations is not known a priori and needs to estimated. In the iterative method regularisation is achieved by stopping the procedure after a few iterations. To confirm that the choice of the initial assumption for the true distribution does not bias the unfolded result, different distributions can be chosen as a starting point. In the toy model test, the iterative Bayesian unfolding delivers an good result, as shown in Fig. 6.2d.

6.3.2 Closure test

The correctness of the implementation of the Bayesian unfolding in the RooUnfold package is tested as follows. Pseudo measurements are created from the default signal MC sample. The prior is set to the true Z boson p_{T} spectrum of this sample, and this sample is also used to determine the response matrix. The relative difference between the true distribution and the unfolded distribution is smaller than 10^{-12} in each bin and independent of the number of iterations.

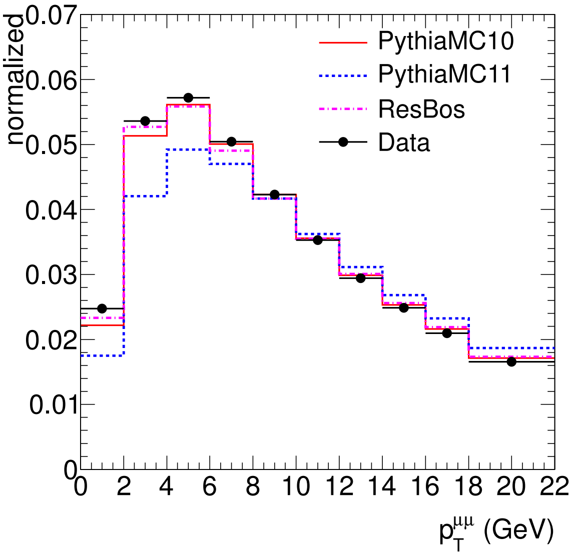

Figure 6.3: Shape of the p_{T} distribution of different MC generators compared with data at detector level.

6.3.3 Convergence of the iterative unfolding

While the closure test is a trivial check, it needs to be shown that the iterative unfolding converges when the measured distribution is different to the one used to define the response matrix and the initial assumption on the true distribution. This test is performed with pseudo data samples where the unfolded distributions can be compared with the truth distributions. The pseudo data samples are created by applying p_{T} dependent weights to the original MC simulation, with weights chosen to model the true p_{T} spectrum from Resbos and from a different Pythia tune (MC11). The resulting distributions are shown in Fig. 6.3. These distributions are unfolded, where the response matrix and initial true distribution are always the default Pythia MC10. The convergence of the unfolded result towards the true values is shown in Fig. 6.4. As can be seen, the unfolded distributions approach the true distributions after a small number of iterations, but they do not become identical. The largest differences are observed for the unfolding of the Pythia MC11 pseudo data sample, where the unfolded result converges to values different from the true values by 2σ in the first bins. The result is better for the pseudo data test with the shape taken from Resbos. This indicates the amount of bias inherent in the method, when the initial assumption of a true distribution is very different from the distribution to be unfolded, as it is the case here. The bias is however not as large as it seems. The difference between Pythia MC10 and Pythia MC11 is 30% is in the first bin. The difference between the unfolded pseudo data with shape taken from Pythia MC11 to its true distribution using the response matrix and initial true distribution from Pythia MC10 is smaller then 0.3%. This bias will be considered as systematic uncertainty on the measurement, and is comparable in size to other systematic uncertainties.

Since the observed differences between the unfolded and true distributions are a combin-

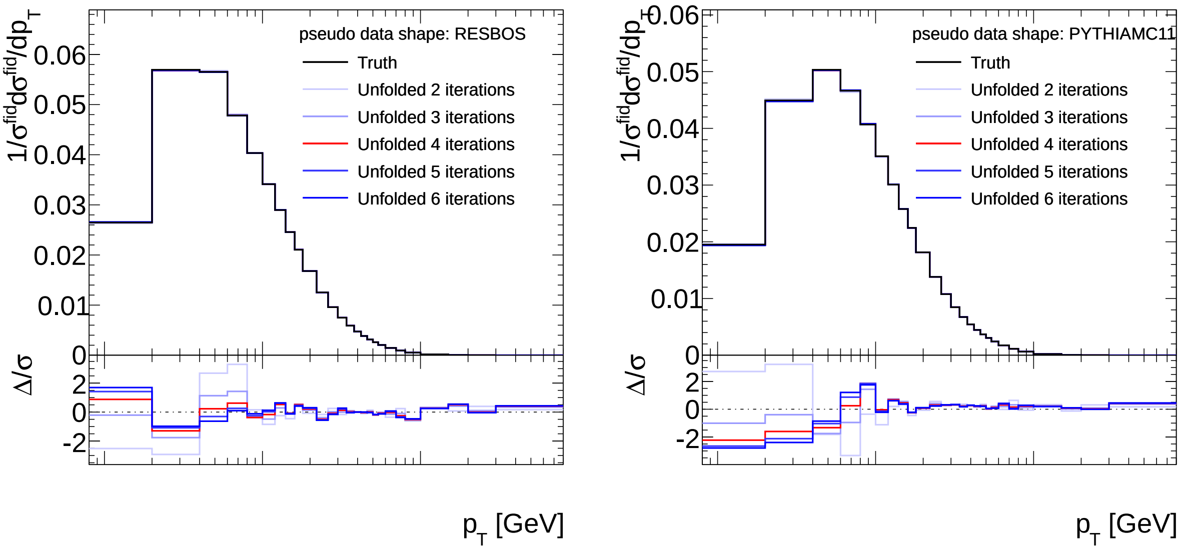

(a) Pseudo data shape is taken from Resbos (b) Pseudo data shape is taken from Pythia MC11

Figure 6.4: Comparison of the unfolded pseudo data distributions after 1 to 5 iterations with the true distributions.

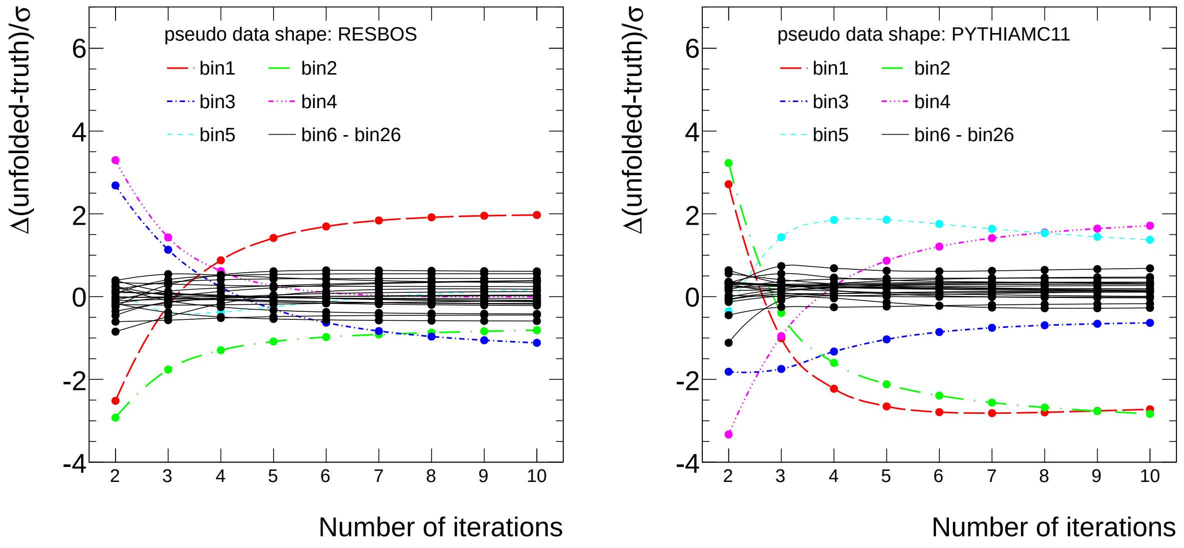

(a) Pseudo data shape is taken from Resbos (b) Pseudo data shape is taken from Pythia MC11

Figure 6.5: Reduced difference between pseudo data unfolded and truth distributions as a function of the number of unfolding iterations.

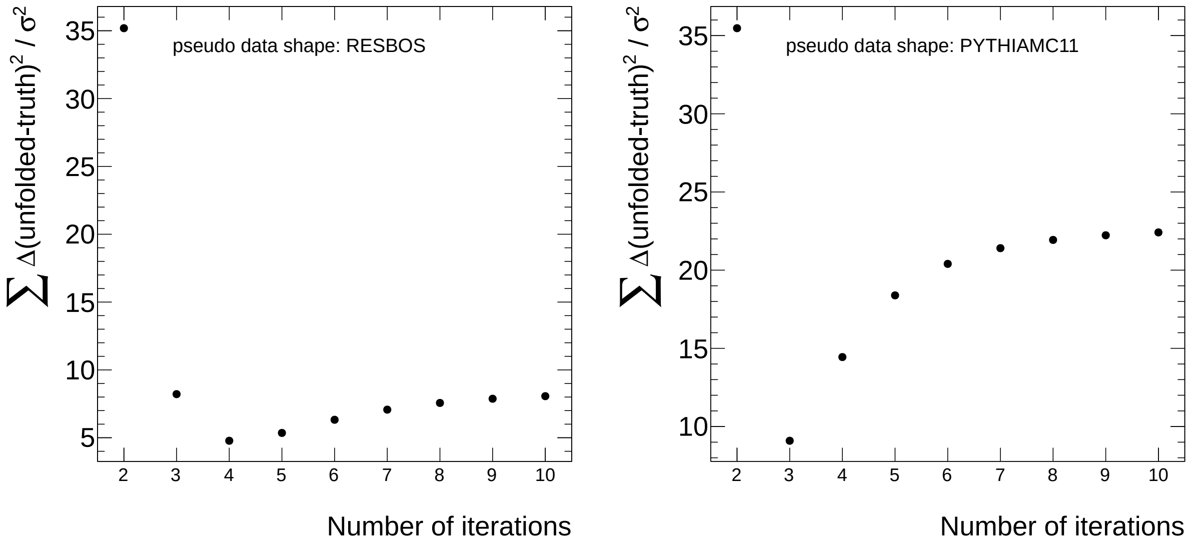

(a) Pseudo data shape is taken from Resbos (b) Pseudo data shape is taken from Pythia MC11

Figure 6.6: Convergence of pseudo data unfolded distributions to their true distributions with the number of iterations. The convergence criterion is the sum of the squared difference between unfolded and truth value divided by the statistical uncertainty in each bin.

ation of unfolding bias (which is expected to decrease with the number of iterations) and variance (which increases with the number of iterations), this test is used to determine the optimal number of iterations. Naturally the variance is expected to be larger in bins with less entries. For this reason, to judge the unfolding convergence the difference between the true and unfolded distribution in each bin is divided by the statistical uncertainty of the raw distribution before unfolding. This i call the reduced difference Δ/σ, with

$$\Delta/\sigma = (\text{unfolded} - \text{truth})/\sigma \quad . \tag{6.9}$$

It is shown as a function of the number of iterations in Fig. 6.5. As can be seen only the first 5 bins show significant differences between the unfolded and the true values, and after the fourth iteration the differences between successive unfolding results are small. The unfolding bias is at most twice the size of the statistical uncertainty, which has to be accepted. In bins 6 to 26, the difference between unfolded and true distribution is smaller than the statistical uncertainty in those bins.

To determine the optimal number of iterations, a global convergence criterion is defined by the squared sum of Δ/σ over all bins. As shown in Fig. 6.6, it is minimal after 3 iterations for the test with the pseudo data shape taken from Pythia MC11 and after 4 iterations for the test with Resbos. The convergence for unfolding the transverse momentum distribution binned in y is shown in Fig. 6.7. As can be seen the convergence is very similar in this case, which is expected since the migrations are similar in these distributions. The difference in the sample size for the double differential measurement has no strong effect. In the following 3 iterations are used to unfold the Z boson p_{T} distribution.

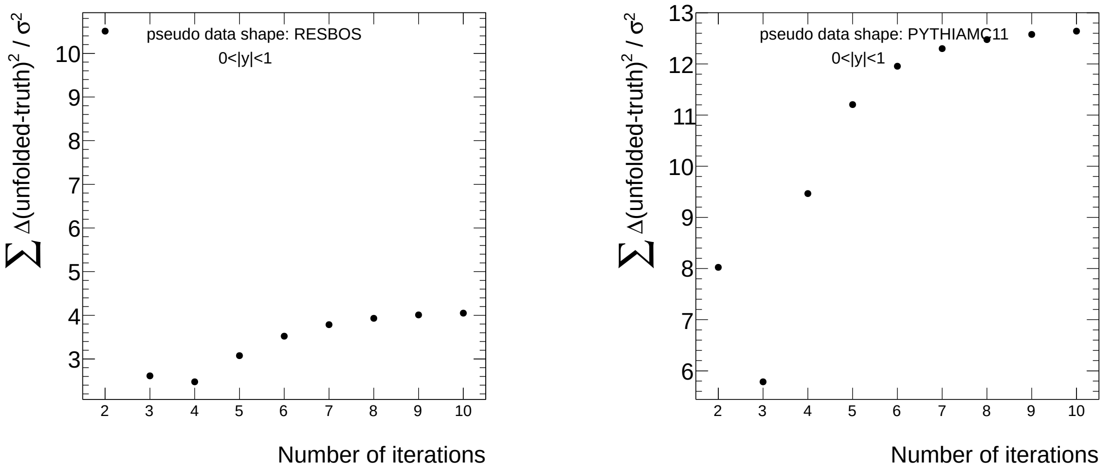

(a) Pseudo data shape is taken from Resbos (b) Pseudo data shape is taken from Pythia MC11

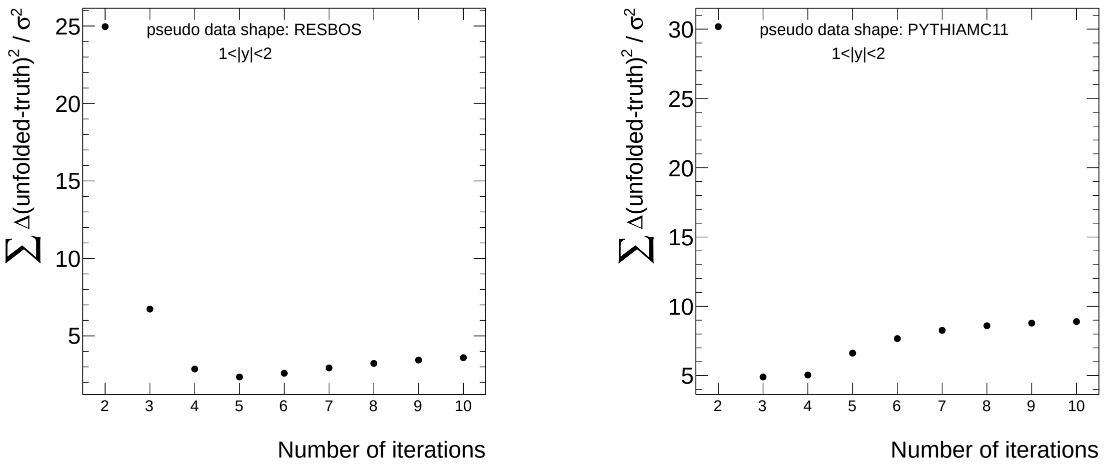

(c) Pseudo data shape is taken from Resbos (d) Pseudo data shape is taken from Pythia MC11

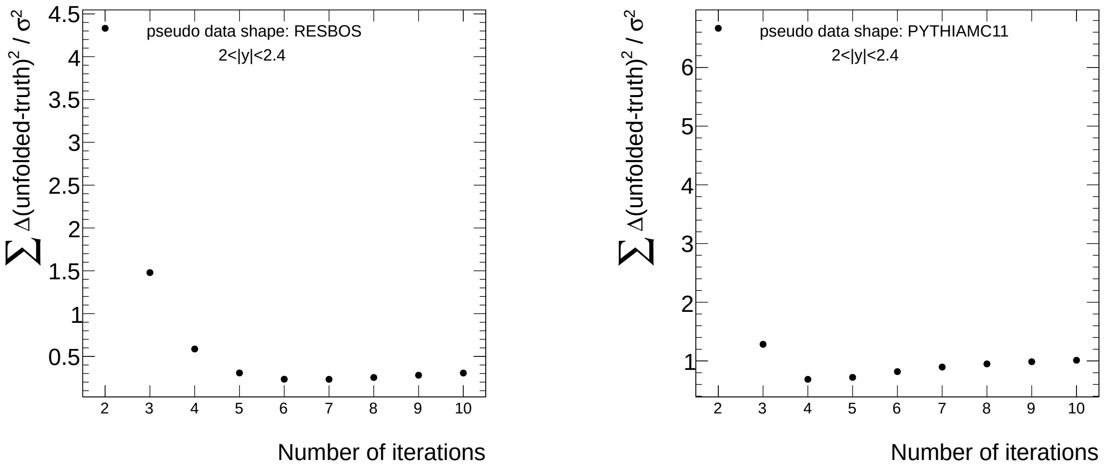

(e) Pseudo data shape is taken from Resbos (f) Pseudo data shape is taken from Pythia MC11

Figure 6.7: Convergence of pseudo data unfolded distributions to their true distributions with the number of iterations. The convergence criterion is the sum of the squared difference between unfolded and truth value divided by the statistical uncertainty in each bin.

Chapter 7

Uncertainties

Uncertainties in the measurement are introduced for one by the limited size of the data and MC samples, and by experimental and theoretical uncertainties in the modelling of the signal and background processes. The evaluation of the statistical uncertainties is described in Sections 7.1 and 7.2. Experimental sources of uncertainty are the muon reconstruction efficiency, trigger efficiency (Section 7.3), muon momentum resolution (Section 7.4) and the background subtraction (Section 7.5). The definition of the response matrix from simulated samples has theoretical uncertainties, which are described in Section 7.6.

The calculation of the normalised cross section $1/\sigma d\sigma/dp_{\mathrm{T}}$ involves three steps: the measurement of the uncorrected spectrum, subtraction of the expected background contribution, and unfolding. The systematic uncertainties in the measurement enter in the background subtraction, and in the definition of the response matrix used to unfold the data. The evaluation of the different sources of uncertainties involves propagating the related variation to the normalised cross section. Each variation is performed independently resulting in the normalised cross section $\sigma_x(p_T)$. The uncertainty due to source x is taken from the difference between the values of the resulting normalised cross section and the nominal cross section:

$$\delta_x(p_{\mathrm{T}}) = |\sigma_x(p_{\mathrm{T}}) - \sigma(p_{\mathrm{T}})| \quad . \tag{7.1}$$

Since the unfolding and normalisation procedures introduce correlations between bins, the covariance matrix for each variation is computed as:

$$C_{ij} = \left[(\sigma_x(p_{\mathrm{T}})_i - \sigma(p_{\mathrm{T}})_i)(\sigma_x(p_{\mathrm{T}})_j - \sigma(p_{\mathrm{T}})_j)\right], \tag{7.2}$$

where $\sigma_{i,j}$ and $\sigma_{x,i,j}$ are the values of the nominal and varied cross sections in bins i, j.

7.1 Data statistical uncertainty

Since the unfolding introduces non-trivial correlations between bins, the statistical uncertainty is determined with the help of pseudo-experiments. The bin contents of the data distribution before background subtraction and unfolding are considered independent variables distributed according to Poisson statistics with mean given by the nominal content of the bin. From the measured p_{T} distribution an ensemble of distributions is obtained by fluctuating the bin contents in each bin according to a Poisson distribution. The normalised cross section is calculated for each resulting distribution by subtracting the background and unfolding. From the set of unfolded distributions the covariance matrix is calculated according to:

$$C_{ij}^{stat} = \frac{1}{M} \sum_{k=1}^{M} \left[(U_i^k - U_i^{nom})(U_j^k - U_j^{nom}) \right] , \tag{7.3}$$

where M is the number of samples and U_i^{nom} and U_i^k are the contents of bin i of the nominal and fluctuated distributions. Neglecting correlations, the uncertainty in each bin calculated as:

$$\delta_i^{stat} = \sqrt{C_{ii}^{stat}} \quad . \tag{7.4}$$

The statistical uncertainty is 0.2% to 1% for the bins with $p_{\mathrm{T}} < 150\mathrm{GeV}$, and increasing for the last bin up to 6%.

7.2 Statistical uncertainty from simulated samples

A systematic uncertainty is introduced by the limited size of the simulated sample used to define the response matrix. The uncertainty is estimated by producing an ensemble of response objects and using these to unfold the data. The response matrix is constituted by three parts, the migration matrix, and two histograms which contain the events present at truth level which are not measured or the events which do not fall inside the truth acceptance but are reconstructed inside the acceptance. Each bin in these distributions is considered as independent, and therefore collections of response objects are obtained by fluctuating the bin contents in each bin according to a Poisson distribution. The fluctuation procedure is done separately for each part of the response object. For each set of variations the covariance matrices are computed according to Equation 7.3. The related uncertainty is 0.05% to 1%.

7.3 Efficiency

A correction for the event selection efficiency is performed implicitly in the unfolding procedure. The efficiency correction values are obtained from the simulated signal sample that defines the response object. The selection efficiency as a function of Z boson p_{T} is shown in Figure 7.1 for the default signal sample. Since the trigger and offline selection is based on muons, their trigger and reconstruction efficiencies are studied in detail. To be able to study the selection efficiency in data, it is factorised into the muon reconstruction efficiency, ϵ_{reco}, the muon trigger efficiency, ϵ_{trig}, the efficiency of the muon isolation cut, ϵ_{iso}, and the efficiency of all other event selection cuts, $\epsilon_{\mathrm{other}}$. The event efficiency can be written as:

$$\epsilon_{\mathrm{event}} = \epsilon_{\mathrm{reco}}^2 \cdot \epsilon_{\mathrm{iso}}^2 \cdot (1 - (1 - \epsilon_{\mathrm{trig}})^2) \cdot \epsilon_{\mathrm{other}} \quad . \tag{7.5}$$

The correct modelling of the selection efficiency is tested by measuring the muon related efficiencies in data and comparing with the simulation. The only other event selection requirements, which are described by $\epsilon_{\mathrm{other}}$, are basic event cleaning requirements on the

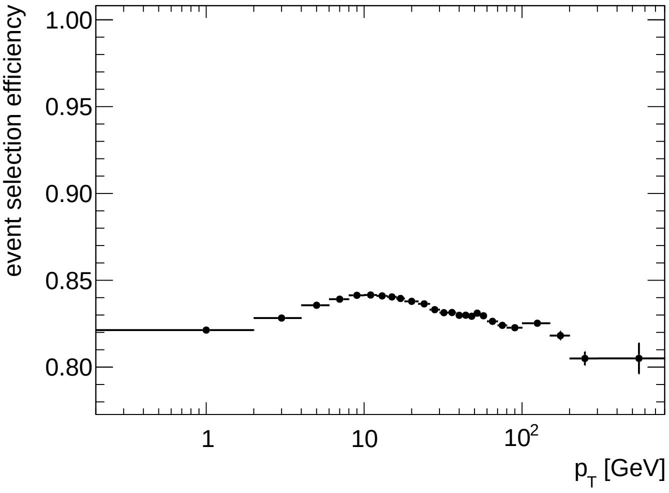

Figure 7.1: Event selection efficiency as a function of Z boson p_T in the POWHEG sample.

presence and position of the primary vertex. These are independent of the specifics of the hard process, and are assumed to be flat with respect to Z boson p_T.

The muon reconstruction efficiencies for the 2011 data sample have been measured before as a function of muon p_T, η and ϕ (see Section 4.5.2). The muon trigger and reconstruction efficiencies have been measured to be essentially constant as a function of muon p_T above 20 GeV. Inefficiencies are mainly due to holes in the detector coverage, therefore the efficiency varies with η and ϕ. As there is no strong correlation between these and Z boson p_T, the influence of these inefficiencies on Z boson p_T is expected to be flat. One aspect not taken into account by the studies, which are dominated by the peak in the Z boson p_T distribution at low p_T, is the changing event topology with increasing p_T. At higher p_T the event contains more likely contributions from hard jets, and the angular separation between jets and the decay muons changes with p_T. An overlap of hadronic activity with the muon can have an influence on the reconstruction, and in particular on the isolation efficiency. In addition the pileup dependence of the efficiencies is studied.

7.3.1 Tag-And-Probe method

The Tag-And-Probe method allows to measure muon efficiencies directly from the measured data itself, by selecting a clean, unbiased sample of muon probes. An event sample is selected in the phase space region corresponding to $Z \rightarrow \mu^+\mu^-$ production, by requiring two tracks with an invariant mass in the region around the Z mass. To reduce combinatorial background, tight requirements are placed on one of the tracks to identify it as a real muon, which is then called the *tag muon*. The other track is deduced to be a real muon as well. It is then used to probe the efficiency of the trigger, reconstruction or isolation. To avoid a bias coming from the event recording, the tag muon is in all cases required to be matched to a trigger. The correlation between tag and probe muons is sufficiently weak, so that an inefficiency of the tag muon selection does not affect the uniformity of the probe coverage for differential measurements. An unbiased efficiency measurement requires that all possible tag and probe combinations are counted. Since the efficiency for the tight muon cuts are around 90%, most events contribute twice. The event selection can be summarised by the following requirements:

- the tag, probe muons must fulfil $p_{\mathrm{T}} > 20\,\mathrm{GeV}, |\eta| < 2.4$,
- the invariant mass is in 10 GeV around the Z mass,
- the tag and probe muons must have opposite charge,
- the tag muon is *tight*,
- the tag muon is matched to the trigger.

A smaller mass window is used here in comparison with the default selection to reduce the relative background fraction. This is intended to counterbalance the increase in background due to the looser selection requirements on the probe muon, whose exact definition depends on the efficiency to be measured.

7.3.2 Muon reconstruction efficiency

Muons in this analysis are reconstructed by the combined muon algorithm or the segment tagged muon algorithm. Both match an inner detector track with a track or track segments in the muon spectrometer to form a combined muon object (see Section 4.4). The single muon reconstruction efficiency can therefore be factorised into the efficiency of the track reconstruction in the inner detector, and the combined reconstruction efficiency,

$$\epsilon_{\mathrm{reco}} = \epsilon_{\mathrm{ID}} \cdot \epsilon_{\mathrm{combined}} \quad . \tag{7.6}$$

The efficiency measurement of the combined muon reconstruction, given the reconstruction if the inner detector track, is described first. The selected probes are inner detector tracks with the same requirements on hits on track and the isolation variable as in the main analysis cuts, described in Section 5.3. The rest of the event selection follows the requirements listed above.

The so selected probe tracks are used to test the reconstruction, by looking for muons within a cone of $\Delta R < 0.05$ around the probe track. The efficiency is calculated from the ratio of the number of probe tracks for which a matching muon was found, to the total number of probe tracks:

$$\epsilon_{\mathrm{TP}} = \frac{n_{\mathrm{matched}}}{n_{\mathrm{all}}} \quad . \tag{7.7}$$

In the same way, the efficiency is determined in the simulation. The backgrounds taken into account are the same as in the main analysis, with the QCD background being estimated by the PYTHIA heavy flavor samples, listed in Table 5.1. Some of the background contributions lead to a lower measured efficiency in data, most notably the $W \rightarrow \mu\nu$ process. Since the aim here is to compare the efficiency modelling in the simulation with the data, the

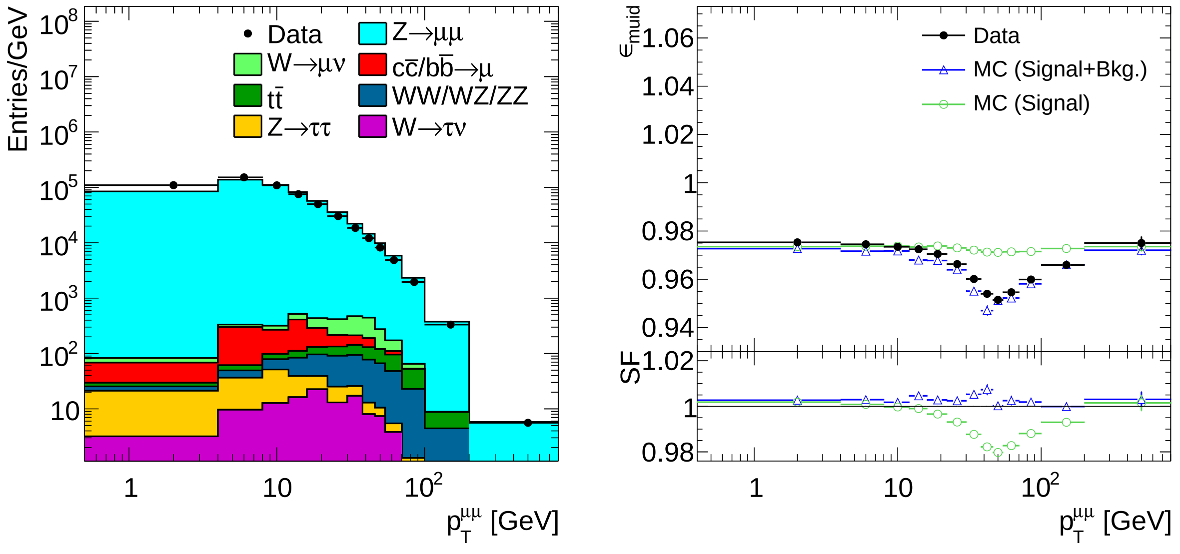

(a)

(b)

Figure 7.2: Tag-and-probe efficiency determination for Muid *tight* reconstruction. (a) Reconstructed transverse momentum $p_T^{\mu\mu}$ of the tag and probe pairs. (b) Reconstruction efficiency for Muid *tight* muons as a function of the dimuon transverse momentum. The data, shown with full dots, are compared with the efficiency measured in the simulation. The efficiency for the signal is shown with open circles, and the efficiency for signal plus backgrounds is shown with open triangles.

measured data efficiency is not corrected for these backgrounds but instead they are included in the simulated efficiency. This means that the actual muon efficiencies are higher than the ones shown here.

The $p_T^{\mu\mu}$ reconstructed from the tag and probe tracks is shown in Fig. 7.2a. An increased contribution from $W \to \mu\nu$ events can be observed at intermediate values of the reconstructed transverse momentum. This is expected, since the muon from the W decay passes the tag requirements. There is a small chance to have another track in the event that fulfils the probe requirements, which is most likely not a muon. The background contribution in the intermediate p_T range has a sizeable effect on the efficiency determination. The reconstruction efficiency as a function of the transverse momentum reconstructed from the tag and probe pair is shown in Fig. 7.2b. The efficiency determined in data is compared with the efficiency obtained from simulation, considering the signal only, as well as the signal plus backgrounds. The W boson background leads to a lower efficiency in the region 20 . . . 100 GeV, which is very well modelled by the simulation when including background.

To test the influence of additional pileup events on the reconstruction efficiency, the reconstruction efficiency is determined as a function of the number of primary vertices present in the events. The muon reconstruction efficiency for isolated muons is not affected by pileup, as is illustrated in Fig. 7.3.

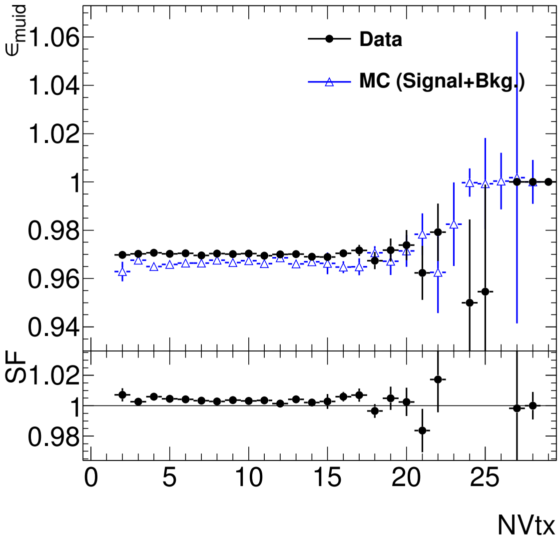

Figure 7.3: Reconstruction efficiency for Muid *tight* muons as a function of the number of pileup vertices in the event.

7.3.3 Inner Detector track reconstruction efficiency

This section describes the measurement of the inner detector track reconstruction, given the presence of a muon spectrometer track. The probe selection requires a muon spectrometer standalone track, while the tag selection and the event selection is unchanged to above.

The $p_{\mathrm{T}}^{\mu\mu}$ reconstructed from the tag and probe track pairs is shown in Fig. 7.4a. In this selection the background is negligible for the efficiency determination. The reconstruction efficiency as a function of the transverse momentum reconstructed from the tag and probe pair is shown in Fig. 7.4b. It is flat up to 100 GeV, and decreasing by 5% at the highest p_{T} values. The track reconstruction efficiency is very well modelled by the simulation. The tracking efficiency for isolated muons is not affected by pileup, as is illustrated in Fig. 7.5.

7.3.4 Muon isolation efficiency

Muons in the analysis are required to be isolated from other tracks. The efficiency of this cut on the muon tracks can be studies by selecting events according to the Tag-and-Probe selection described above, where the probe muon fulfils the same requirements as the tag muon with the exception of the isolation requirement. The efficiency is calculated from the ratio of the number of probe muons that fulfil the isolation requirement to the total number of probe muons.

The $p_{\mathrm{T}}^{\mu\mu}$ reconstructed from the tag and probe track pairs is shown in Fig. 7.6a. The isolation efficiency as a function of the transverse momentum reconstructed from the tag and probe pair is shown in Fig. 7.6b. It is about 99.5% at low p_{T} and decreases to 98.5% at intermediate values of p_{T}. The isolation efficiency is well modelled by the simulation, but a slight trend to overestimate the efficiency by 0.5% at the highest p_{T} can be observed. This

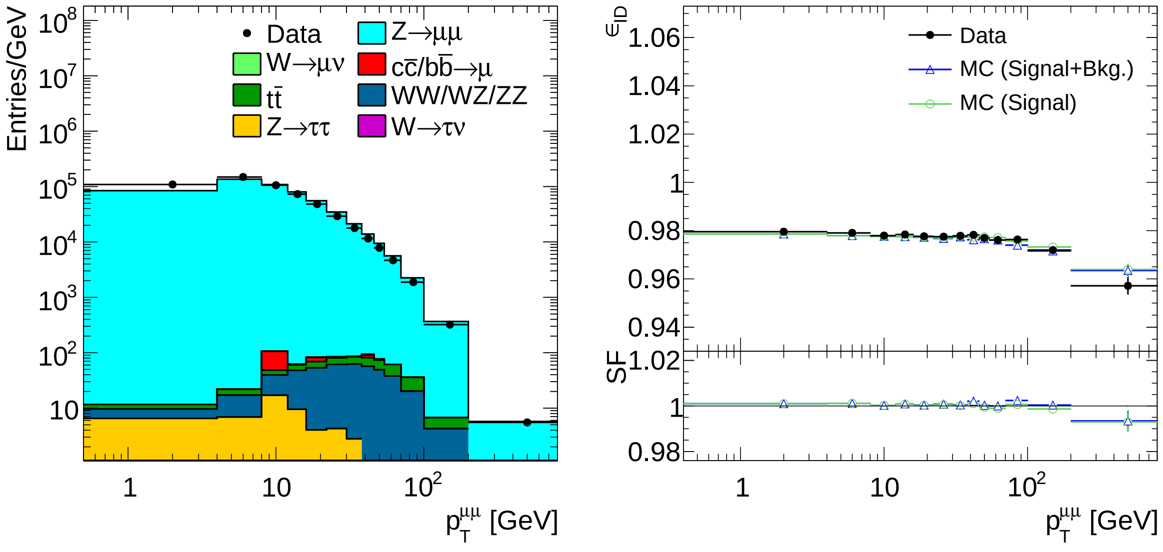

(a)

(b)

Figure 7.4: Tag-and-probe efficiency determination for inner detector track reconstruction. (a) Reconstructed transverse momentum $p_T^{\mu\mu}$ of the tag and probe pairs. (b) Inner detector track reconstruction efficiency for muons as a function of the dimuon transverse momentum. The data, shown with full dots, are compared with the efficiency measured in the simulation. The efficiency for the signal is shown with open circles, and the efficiency for signal plus backgrounds is shown with open triangles.

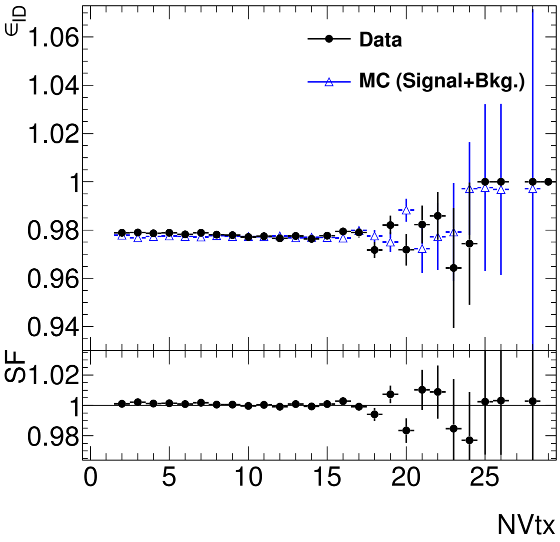

Figure 7.5: Reconstruction efficiency for ID tracks for muons as a function of the number of pileup vertices in the event.

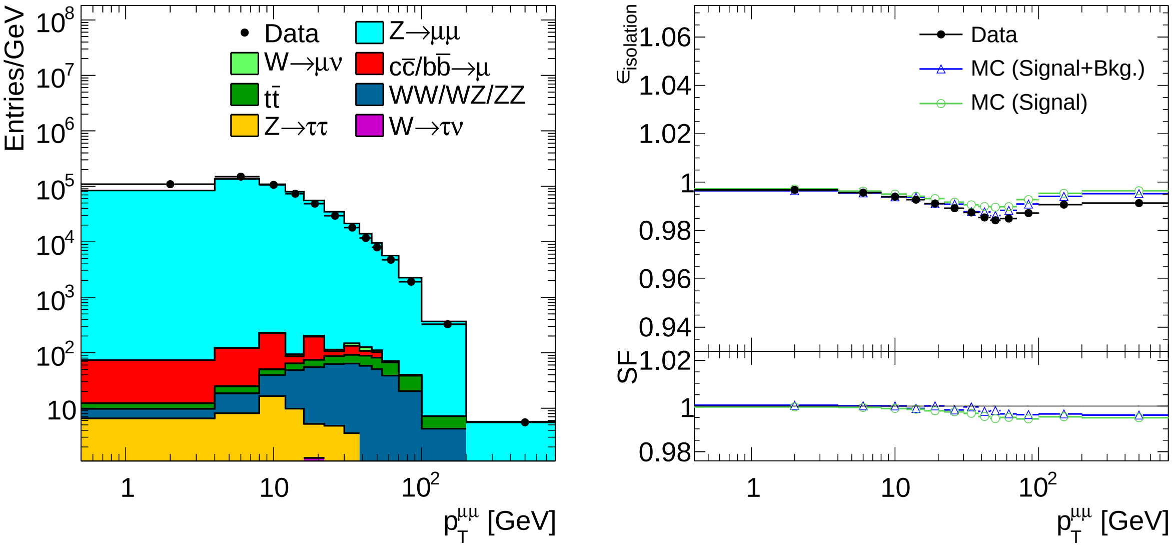

(a)

(b)

Figure 7.6: Tag-and-probe isolation efficiency determination for muons. (a) Reconstructed transverse momentum $p_{\mathrm{T}}^{\mu\mu}$ of the tag and probe pairs. (b) Isolation efficiency for muons as a function of the dimuon transverse momentum. The data, shown with full dots, are compared with the efficiency measured in the simulation. The efficiency for the signal is shown with open circles, and the efficiency for signal plus backgrounds is shown with open triangles.

hints at differences in the event topology (track multiplicity, jet structure) between data and simulation in the high p_{T} region. The isolation efficiency for muons is not affected by pileup, as is illustrated in Fig. 7.7.

7.3.5 Trigger efficiency

The muon trigger efficiency is measured using the Tag-and-Probe selection as described in Section 7.3.1 for the muon reconstruction efficiency. The probe muon must fulfil all the requirements of the tag muon with the exception of the requirement to be matched to a trigger object. The trigger efficiency is tested by looking for a muon trigger object in a cone of $\Delta R < 0.18$ around the probe muon. The efficiency is calculated from the ratio of the number of probe muons, that could be matched to a trigger object, to the total number of probe muons. The $p_{\mathrm{T}}^{\mu\mu}$ reconstructed from the tag and probe track pairs is shown in Fig. 7.8a. The trigger efficiency as a function of the transverse momentum reconstructed from the tag and probe pair is shown in Fig. 7.8b. It is observed to be constant as a function of p_{T}, and well modelled by the simulation, except for an offset of about 1.5%.

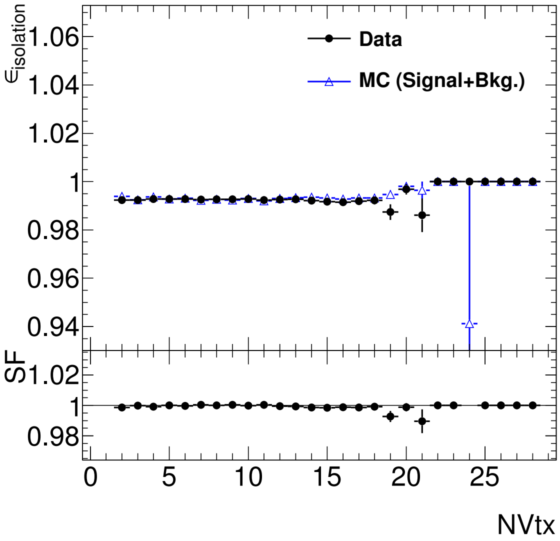

Figure 7.7: Isolation efficiency for muons as a function of the number of pileup vertices in the event.

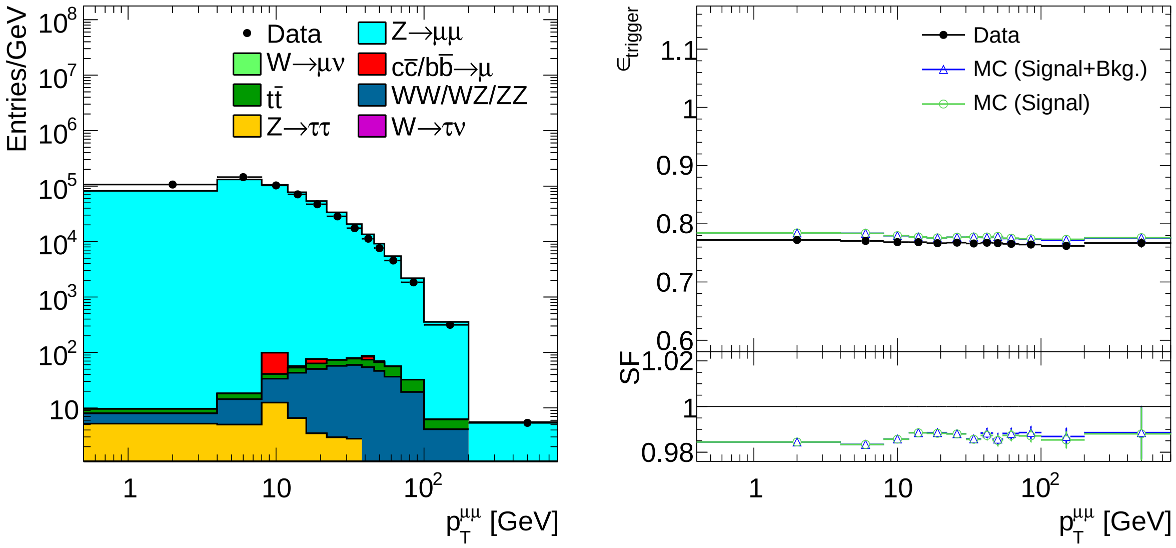

(a) (b)

Figure 7.8: Tag-and-probe trigger efficiency determination. (a) Reconstructed transverse momentum $p_T^{\mu\mu}$ of the tag and probe pairs. (b) Trigger efficiency for muons as a function of the dimuon transverse momentum. The data, shown with full dots, are compared with the efficiency measured in the simulation. The efficiency for the signal is shown with open circles, and the efficiency for signal plus backgrounds is shown with open triangles.

7.3.6 Uncertainty from the modelling of muon efficiencies

In the normalised measurement the global efficiencies cancel, but not so efficiencies that change with $p_{\mathrm{T}}^{\mu\mu}$. The efficiency correction is part of the unfolding procedure, where the correction is taken from simulation. To account for a possible mis-modelling in the simulation, the difference between the efficiency measured in data from the efficiency in the simulation is described by scale factors, defined as:

$$\mathrm{SF} = \frac{\epsilon_{\mathrm{data}}}{\epsilon_{\mathrm{MC}}}. \tag{7.8}$$

As was shown in the previous sections, the scale factors are very close to unity, and almost flat with respect to $p_{\mathrm{T}}^{\mu\mu}$. Variations in these scale factors as a function $p_{\mathrm{T}}^{\mu\mu}$ introduce an uncertainty on the measurement. Using the factorisation into the sub efficiencies measured in data the event efficiency is:

$$\epsilon_{\mathrm{event}} = \epsilon_{\mathrm{ID}}^2 \cdot \epsilon_{\mathrm{Muid}}^2 \cdot \epsilon_{\mathrm{iso}}^2 \cdot (1-(1-\epsilon_{\mathrm{trig}})^2) \cdot \epsilon_{\mathrm{other}} \quad . \tag{7.9}$$

The $p_{\mathrm{T}}^{\mu\mu}$ dependence of the scale factors for the dimuon (event) efficiency for Muid, ID, isolation and trigger are shown in Fig. 7.9. Since the scale factors factorise in the same way as the efficiencies, the deviation from the average scale factor in each bin is treated as a systematic uncertainty due to the modelling of the muon efficiencies in the simulation. The deviations of the event scale factor in p_{T} bins from the average SF are summarised in Table 7.1. In bins where the statistical uncertainty on the scale factor is larger than the deviation from the average, the systematic uncertainty is increased to the size of the statistical uncertainty. The largest deviations from the average scale factor are observed for the Muid *tight* reconstruction and the isolation requirement, with up to 1% difference.

7.4 Muon momentum resolution

As described in Section 5.2.1, the momentum scale and the momentum resolution of muons in simulated events is corrected to match the observation obtained in $Z \to \mu^+\mu^-$ data. Since the correction influences the migration between $p_{\mathrm{T}}^{\mu\mu}$ bins, the uncertainties on the scale and resolution parameters lead to an uncertainty in the response matrix. This uncertainty is evaluated by building modified response matrices using up/down variations of the scale/smearing parameters, where the variations follow the recommendations of the ATLAS muon combined performance group [38]. The uncertainty is then propagated to the final result by repeating the unfolding with these modified response objects. For the momentum resolution, the contributions from the Muon Spectrometer and Inner Detector measurement are independently varied. The resulting difference in the normalised cross section with respect to the nominal result is shown in Fig. 7.10. For the momentum scale, charge independent and charge dependent contributions are varied, the effect on the normalised cross section is shown in Fig 7.11. The level of accuracy in the description of the muon resolution can be observed in the dimuon invariant mass distribution, which is

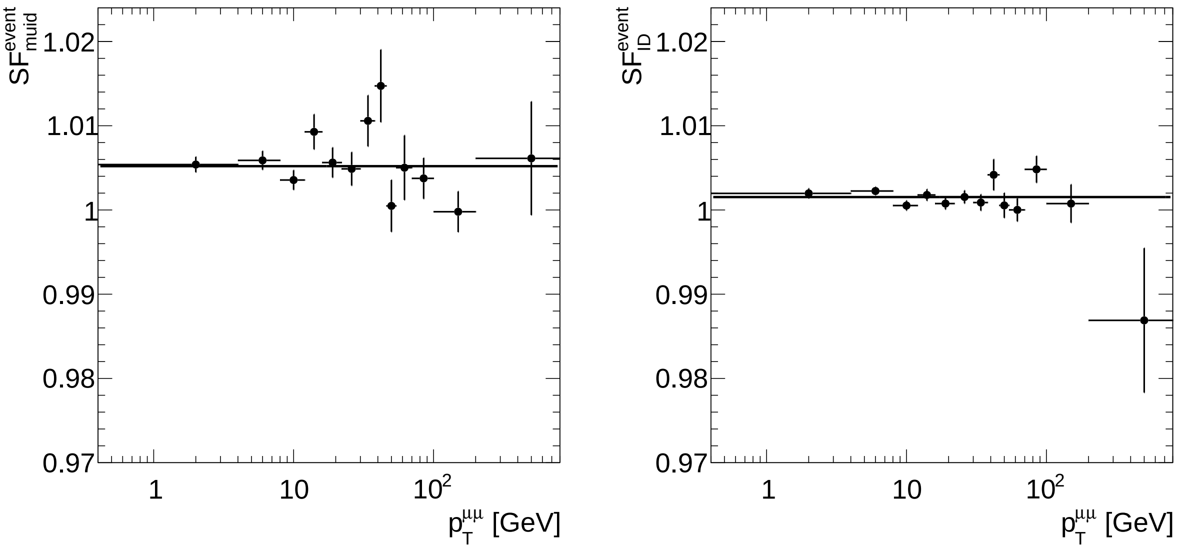

(a) Muon reconstruction efficiency (Muid part)

(b) Muon reconstruction efficiency (ID part)

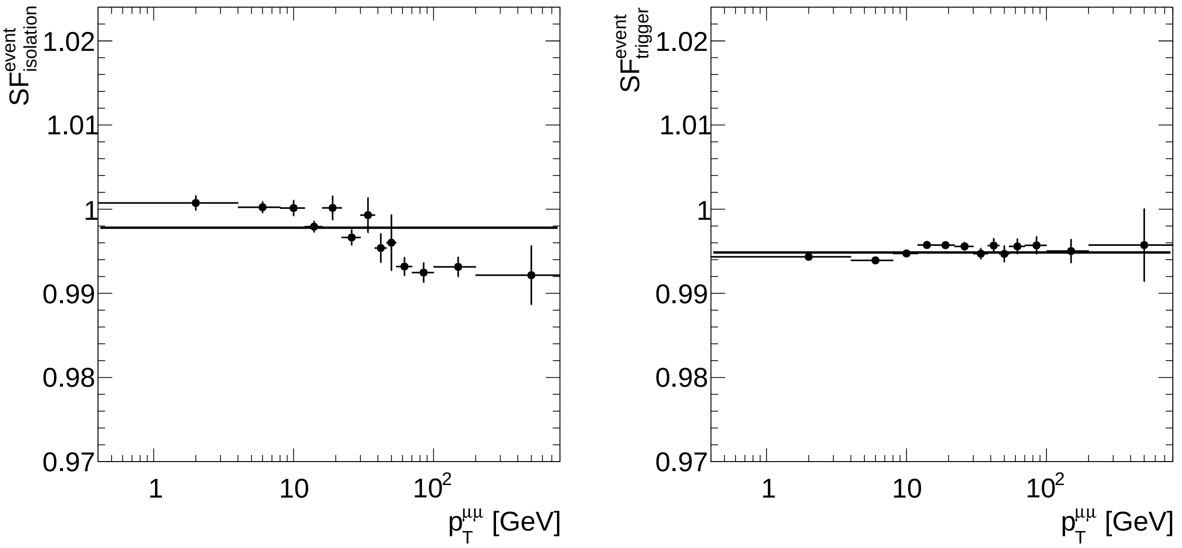

(c) Isolation efficiency

(d) Trigger efficiency

Figure 7.9: Ratio of the dimuon efficiencies measured in data and the simulation. The solid line indicates the extracted average scale factors (SF). The deviations from the average SF are treated as a systematic uncertainty.

Table 7.1: Difference between the event efficiency scale factors in $p_{\mathrm{T}}^{\mu\mu}$ bins from the average scale factors as well as the statistical uncertainty on the efficiency scale factors.

	Muid *tight*		Inner Detector		Isolation		Trigger	
p_{T} (GeV)	$\mathrm{SF}-\overline{\mathrm{SF}}$ (%)	$\delta_{\mathrm{stat}}(\mathrm{SF})$ (%)	$\mathrm{SF}-\overline{\mathrm{SF}}$ (%)	$\delta_{\mathrm{stat}}(\mathrm{SF})$ (%)	$\mathrm{SF}-\overline{\mathrm{SF}}$ (%)	$\delta_{\mathrm{stat}}(\mathrm{SF})$ (%)	$\mathrm{SF}-\overline{\mathrm{SF}}$ (%)	$\delta_{\mathrm{stat}}(\mathrm{SF})$ (%)
0 - 4	0.02	0.09	0.04	0.06	0.33	0.09	-0.05	0.04
4 - 8	0.07	0.11	0.07	0.05	0.28	0.07	-0.09	0.03
8 - 12	-0.16	0.12	-0.10	0.06	0.27	0.09	-0.01	0.04
12 - 16	0.41	0.21	0.03	0.07	0.05	0.07	0.09	0.05
16 - 22	0.04	0.18	-0.08	0.07	0.27	0.14	0.09	0.05
22 - 30	-0.03	0.20	0.00	0.08	-0.08	0.09	0.07	0.05
30 - 38	0.54	0.30	-0.06	0.10	0.18	0.21	-0.01	0.06
38 - 46	0.95	0.43	0.27	0.18	-0.21	0.17	0.08	0.08
46 - 54	-0.47	0.31	-0.10	0.15	-0.14	0.33	-0.02	0.10
54 - 70	-0.02	0.38	-0.15	0.14	-0.43	0.11	0.07	0.09
70 - 100	-0.14	0.24	0.33	0.16	-0.50	0.12	0.09	0.10
100 - 200	-0.54	0.24	-0.08	0.23	-0.43	0.12	0.02	0.14
200 - 800	0.09	0.67	-1.46	0.86	-0.53	0.35	0.09	0.43

shown in Appendix A binned in p_{T} and y.

7.5 Background uncertainty

The uncertainty due to the background contributions is evaluated by changing the normalisation of each background contribution separately, then subtracting the background distribution from data and repeating the unfolding procedure. The QCD background uncertainty is 30%, and the combined uncertainty on the other backgrounds is 13%. The contribution to the overall uncertainty on the normalised cross section is negligible. It is less than 0.2% for all measurement bins.

7.6 Theoretical uncertainties

7.6.1 Modelling of the true p_{T} shape

The imperfect modelling of the true Z boson p_{T} distribution in the simulated sample may lead to a bias in the unfolded distribution, as described in Section 6.3. To evaluate this uncertainty, the nominal simulated sample is reweighted in p_{T} to different shapes. The unfolding is repeated using the response object and initial assumption of the truth distribution produced from these alternative samples.

A comparison of different p_{T} shapes is shown in Fig. 7.12a, including the baseline MC (POWHEG-PYTHIA (MC11 tune) reweighted to PYTHIA (MC10 tune), the PYTHIA MC11 shape,

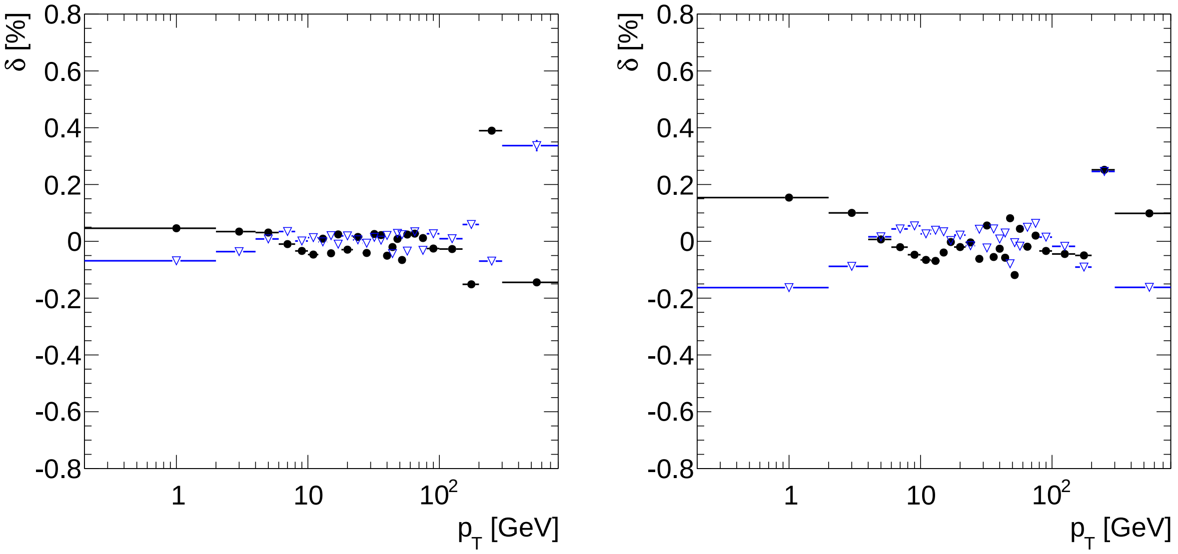

(a)

(b)

Figure 7.10: Systematic uncertainties arising from the muon momentum resolution uncertainty. (a) Difference to the nominal result due to variation of the inner detector resolution parameter. (b) Difference to the nominal result due to variation of the muon spectrometer resolution parameter. Up variations are shown as solid circles, down variations as open triangles.

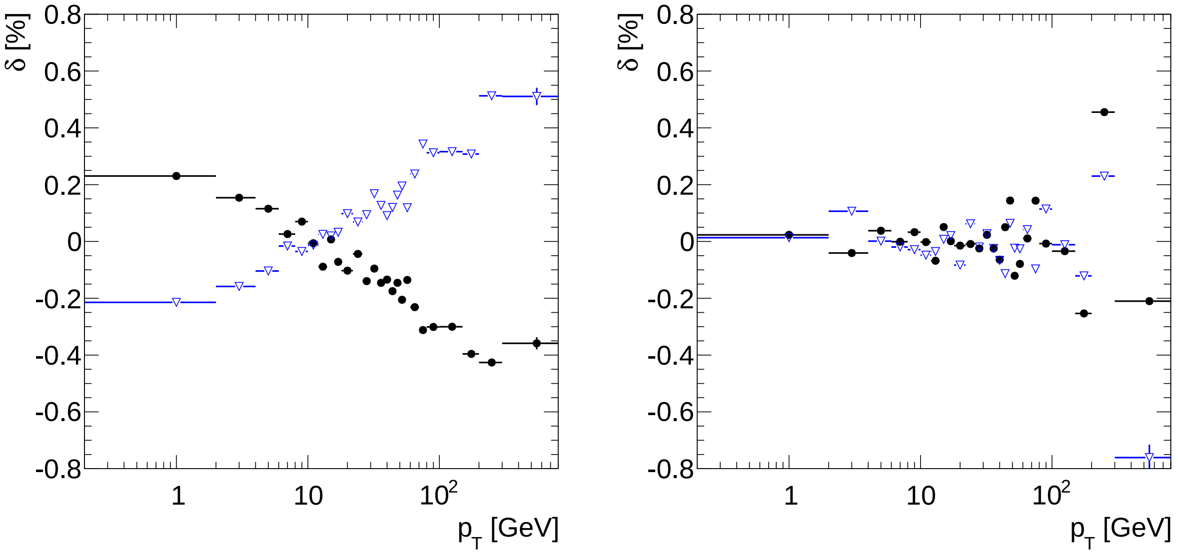

(a)

(b)

Figure 7.11: Systematic uncertainties arising from the muon momentum scale uncertainty. (a) Difference to the nominal result due to variation of the charge independent parameter. (b) Difference to the nominal result due to variation of charge dependent scale parameter. Up variations are shown as solid circles, down variations as open triangles.

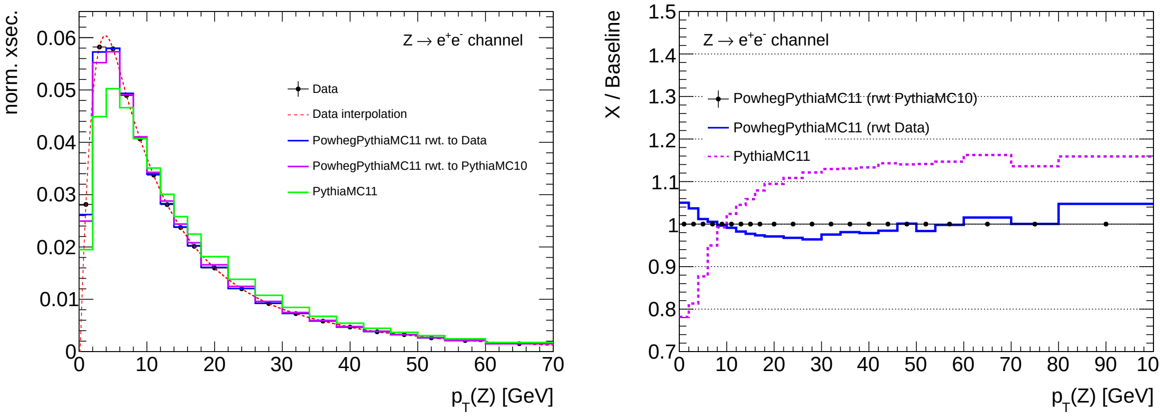

(a) (b)

Figure 7.12: Comparison of different p_T shapes used to estimate the p_T modelling unfolding systematic. (a) Different shapes, including MC baseline and data, (b) Comparison of two variations with respect to the baseline. [71]

the data points (measurement), an extrapolation made from $Z \rightarrow e^+e^-$ data points (using splines), and the shape obtained by reweighting the Powheg-Pythia sample to the data shape (weights computed using the extrapolation) [71].

The alternative shape of the Pythia (MC11) sample is very far from the observed data. In order to avoid an overestimation of the systematic uncertainty, the shape obtained from the data extrapolation is chosen to reweight the baseline simulation, and to repeat the unfolding. The resulting difference to the nominal result is shown in Fig. 7.13a. The difference shows large fluctuations between bins, due to statistical fluctuations. Since the two distributions are obtained from the same samples, they are largely correlated but the exact correlations are not easy to determine. As there is no reason to suspect such large changes from bin to bin, an attempt to smoothen the uncertainty estimate is made by combining neighbouring bins. The resulting uncertainty estimate is shown in Fig. 7.13b. Since the uncertainty due to the limited MC sample statistics is already accounted for, the smoothed values are assigned as systematic uncertainty. The size of this uncertainty is 0.1% to 1.5% which is negligible compared with the statistical uncertainty.

7.6.2 MC generator model dependence

Here the uncertainty from the theoretical modelling apart from the p_T shape is evaluated. The dependence on the hard matrix element calculation, the parton shower model and the hadronisation model is tested by comparing the nominal result with the result obtained using the response object defined by Mc@nlo (Table 5.1). Mc@nlo implements an alternative NLO matrix element calculation and uses Herwig for the parton shower. The Mc@nlo sample is reweighted to the same p_T shape as the nominal sample, in order to separate the effect of the p_T shape modelling from other model uncertainties.

The resulting difference in the normalised unfolded distribution to the nominal result

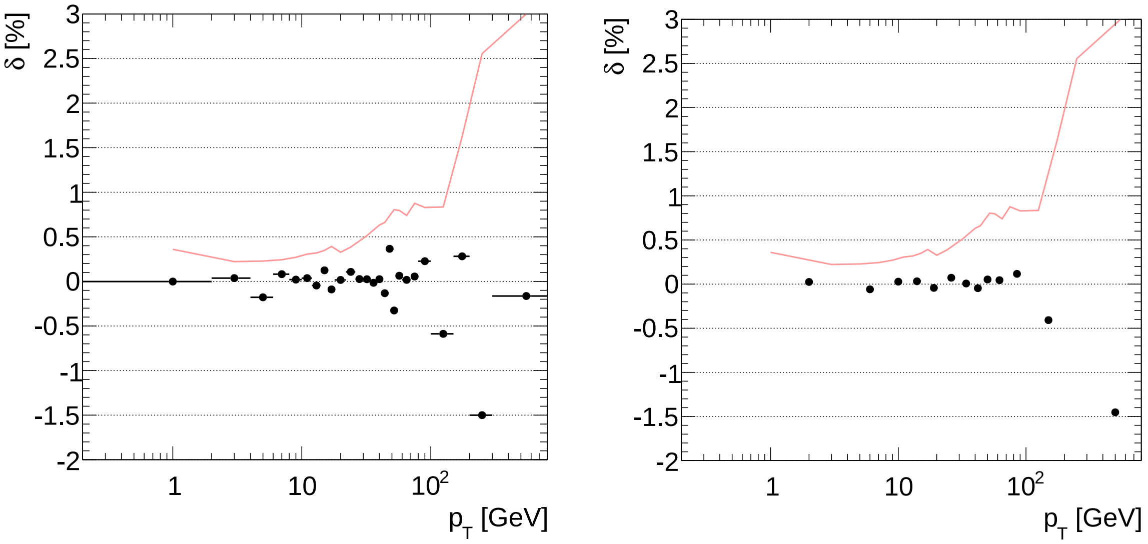

(a)

(b)

Figure 7.13: Systematic uncertainty associated with the modelling of the Z boson p_{T} shape in simulation. a) Relative difference between the unfolded distribution obtained using the response object reweighted to data, and the nominal result. (b) smoothed uncertainty obtained by dividing the number of bins by 2. The data statistical uncertainty is shown for reference by the red line.

is shown in Fig. 7.14a. As can be seen, the difference shows large statistical fluctuations between bins. Since the samples used to define the response matrices are statistically independent, the error bars on the difference are computed from the MC statistic error estimations for each sample, according to the procedure explained in Section 7.2. The error is dominated by the statistical uncertainty of the very small MC@NLO sample. Given that the error bars cover the range of the fluctuations between bins and the absence of a slope or trend, the difference is compatible with zero. A conservative estimate of an uncertainty due to a generator dependence is given by the statistical uncertainty on the difference, shown in Fig. 7.14b. The resulting uncertainty on the normalised cross section is 0.3% to 8%, which is an important contribution to the overall uncertainty of the same size as the data statistical uncertainty.

7.7 Summary of uncertainties

All uncertainties are summarised in Fig. 7.15 and in Table 7.2. The total uncertainty is below 1% for $p_{\mathrm{T}} < 34$GeV and below 2% for p_{T} up to 150GeV. The experimental and theoretical systematic uncertainties and the data statistical uncertainty contribute with about the same size. The dominant experimental uncertainties are the muon momentum scale modelling and the isolation efficiency. The theoretical uncertainty is dominated by the MC model dependence. The estimation of this uncertainty suffers from the limited size of the simulated MC@NLO sample, especially at high p_{T} where this uncertainty dominates

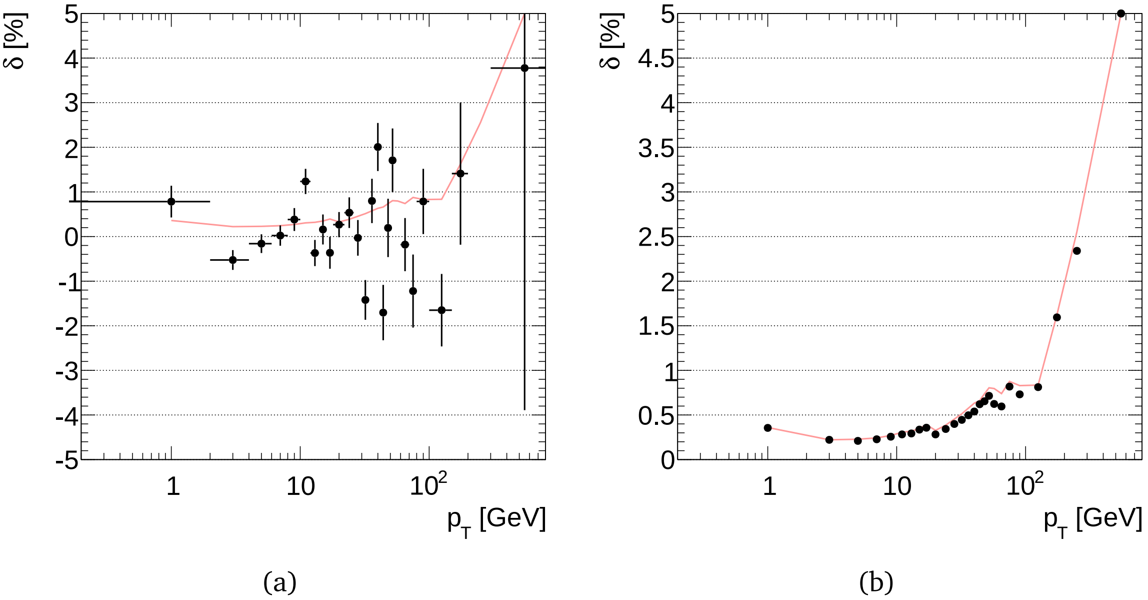

(a)

(b)

Figure 7.14: Systematic uncertainty associated with MC generator model dependence. (a) Relative difference between the unfolded distribution obtained using Mc@nlo and the nominal result. (b) Uncertainty assigned, using the size of the error bars in (a). The data statistical uncertainty is shown for reference by the red line.

the measurement. The uncertainties for the measurement of the transverse momentum distribution in rapidity bins are listed in Appendix B

	Momentum		Efficiency						Theory				
p_{T} (GeV)	Resol. (%)	Scale (%)	ϵ_{muid} (%)	ϵ_{ID} (%)	ϵ_{iso} (%)	ϵ_{trig} (%)	Bkg. (%)	p_{T} shape (%)	Generator (%)	MC stat. (%)	Sys. (%)	Stat. (%)	Total (%)
0.0-2.0	0.20	0.22	0.09	0.06	0.33	0.05	0.02	0.02	0.36	0.06	0.58	0.36	0.68
2.0-4.0	0.10	0.18	0.09	0.06	0.33	0.05	0.02	0.02	0.22	0.04	0.47	0.22	0.52
4.0-6.0	0.03	0.08	0.11	0.07	0.28	0.09	0.01	0.05	0.21	0.04	0.40	0.23	0.46
6.0-8.0	0.04	0.06	0.11	0.07	0.28	0.09	0.01	0.05	0.23	0.04	0.40	0.24	0.47
8.0-10.0	0.07	0.06	0.16	0.10	0.27	0.04	0.01	0.03	0.26	0.04	0.43	0.27	0.51
10.0-12.0	0.06	0.04	0.16	0.10	0.27	0.04	0.01	0.03	0.28	0.05	0.45	0.31	0.54
12.0-14.0	0.06	0.05	0.41	0.07	0.07	0.09	0.01	0.04	0.29	0.06	0.53	0.32	0.62
14.0-16.0	0.03	0.03	0.41	0.07	0.07	0.09	0.01	0.04	0.34	0.06	0.55	0.35	0.65
16.0-18.0	0.03	0.06	0.18	0.08	0.27	0.09	0.01	0.04	0.36	0.07	0.51	0.39	0.64
18.0-22.0	0.05	0.07	0.18	0.08	0.27	0.09	0.01	0.04	0.28	0.05	0.46	0.33	0.56
22.0-26.0	0.05	0.10	0.20	0.08	0.09	0.07	0.02	0.07	0.34	0.06	0.45	0.39	0.59
26.0-30.0	0.06	0.15	0.20	0.08	0.09	0.07	0.01	0.07	0.40	0.07	0.50	0.45	0.68
30.0-34.0	0.07	0.11	0.54	0.10	0.21	0.06	0.01	0.00	0.45	0.08	0.75	0.51	0.91
34.0-38.0	0.07	0.17	0.54	0.10	0.21	0.06	0.01	0.00	0.50	0.09	0.80	0.58	0.98
38.0-42.0	0.05	0.10	0.95	0.27	0.21	0.08	0.02	0.06	0.54	0.10	1.16	0.63	1.32
42.0-46.0	0.05	0.21	0.95	0.27	0.21	0.08	0.02	0.06	0.62	0.11	1.22	0.66	1.38
46.0-50.0	0.05	0.21	0.47	0.15	0.33	0.10	0.03	0.02	0.65	0.12	0.92	0.74	1.18
50.0-54.0	0.05	0.17	0.47	0.15	0.33	0.10	0.04	0.02	0.71	0.13	0.96	0.80	1.25
54.0-60.0	0.05	0.13	0.38	0.15	0.43	0.09	0.04	0.04	0.62	0.13	0.89	0.80	1.19
60.0-70.0	0.06	0.31	0.38	0.15	0.43	0.09	0.06	0.04	0.60	0.12	0.91	0.74	1.17
70.0-80.0	0.05	0.23	0.24	0.33	0.50	0.10	0.08	0.15	0.82	0.14	1.10	0.88	1.40
80.0-100.0	0.06	0.35	0.24	0.33	0.50	0.10	0.11	0.15	0.73	0.14	1.07	0.83	1.35
100.0-150.0	0.03	0.30	0.54	0.23	0.43	0.14	0.10	0.15	0.81	0.15	1.16	0.84	1.43
150.0-200.0	0.08	0.37	0.54	0.23	0.43	0.14	0.07	0.15	1.59	0.31	1.83	1.62	2.45
200.0-300.0	0.13	0.49	0.67	1.46	0.53	0.43	0.08	0.81	2.34	0.49	3.11	2.55	4.03
300.0-800.0	0.61	1.42	0.67	1.46	0.53	0.43	0.09	0.81	7.67	1.42	8.18	5.84	10.05

Table 7.2: Uncertainties on $1/\sigma d\sigma/dp_{\mathrm{T}}$

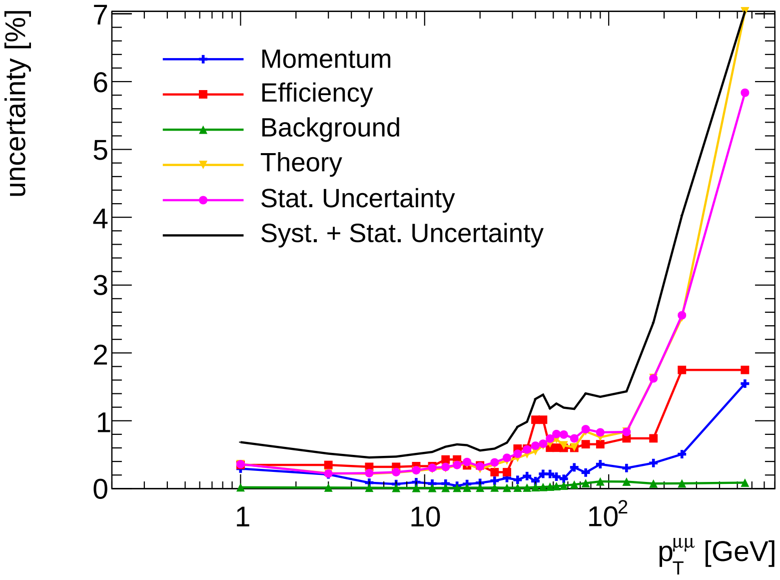

Figure 7.15: Uncertainties on the measurement of $1/\sigma d\sigma/dp_{\mathrm{T}}$, given in percent of the central value of the bin.

Chapter 8

Results

In this chapter the results are reported for the differential cross section of Z boson production in bins of p_{T}^{Z}. From the distribution of all selected $Z \to \mu^{+}\mu^{-}$ candidate events the estimated backgrounds are subtracted, as described in Chapter 5. The resulting distribution is unfolded to particle level as described in Chapter 6 and normalised to the inclusive cross section. The estimation of uncertainties is described in Chapter 7.

8.1 $1/\sigma d\sigma/dp_{\mathrm{T}}$

The normalised differential cross section measured in the $Z \to \mu^{+}\mu^{-}$ production within the fiducial volume is listed in Table 8.1 together with the statistical and systematic uncertainties in each p_{T}^{Z} bin. The measurement is reported at Born level, that is fully corrected for the effect of QED final state radiation (FSR), where the measurement can be combined with a measurement in the $Z \to e^{+}e^{-}$ decay channel. Correction factors to different reference points regarding QED FSR are included in the table: "bare" level means the true p_{T}^{Z} is defined by the final state leptons after QED FSR, and "dressed" level means the true p_{T}^{Z} is defined by the final state leptons recombined with radiated photons within a cone of $\Delta R = \sqrt{(\Delta\eta)^2 + (\Delta\phi)^2} = 0.1$. The "bare" level corresponds closely to what is measured for muons, while the "dressed" level is closer to the measurement of electrons. The QED FSR corrections have been calculated with Photos [59]. The measured cross section at Born level is shown in Fig. 8.1. The cross section is dominated by the range 0 to 30 GeV, with a peak in the bins 2 to 6 GeV and a tail extending up to 800 GeV. The total uncertainty is on average 0.6% from 0 to 30 GeV, and 1.4% over the total range, rising to 10% in the highest bin.

In the following the measured cross section will be compared with different types of QCD predictions for the Z boson transverse momentum distribution. Theoretical predictions for the entire p_{T}^{Z}-range covered by this measurement are available from MC event generators that employ the parton shower (PS) mechanism, for example Pythia [47], Alpgen [54], Powheg [46] and Mc@nlo [49]. A comparison of the predictions from various event generators with the normalised cross section is shown in Fig. 8.2.

Event generators that only include the leading order of the matrix element calculation for the process $pp \to Z$ without any radiation of (hard) gluons produce the Z-boson with a momentum parallel to the beam line and any transverse boost is generated only by the parton shower acting on initial state partons. A pure parton shower prediction is provided

Table 8.1: The normalised differential cross section $1/\sigma d\sigma/dp_{\mathrm{T}}$ in bins of p_{T}^{Z} for $Z \to \mu^{+}\mu^{-}$ events. The cross section is given at Born level, with correction factors for the cross section at the level of bare and dressed final state muons given in addition. The statistical (δ_{stat}) and total systematic (δ_{sys}) uncertainties, as well as their combination (δ_{total}), are given in percent.

p_{T}^{Z} (GeV)	$\frac{1}{\sigma^{\mathrm{fid}}}\frac{d\sigma^{\mathrm{fid}}}{dp_{\mathrm{T}}}$ (1/GeV) Born	k_{bare}	k_{dressed}	δ_{stat} (%)	δ_{sys} (%)	δ_{total} (%)
0 - 2	0.0285	0.968	0.981	0.36	0.58	0.68
2 - 4	0.0584	0.974	0.985	0.22	0.47	0.52
4 - 6	0.0580	0.986	0.991	0.23	0.40	0.46
6 - 8	0.0493	1.002	0.999	0.24	0.40	0.47
8 - 10	0.0409	1.015	1.007	0.27	0.43	0.51
10 - 12	0.0338	1.027	1.013	0.31	0.45	0.54
12 - 14	0.0282	1.036	1.018	0.32	0.53	0.62
14 - 16	0.0238	1.040	1.020	0.35	0.55	0.65
16 - 18	0.0201	1.041	1.021	0.39	0.51	0.64
18 - 22	0.0159	1.037	1.020	0.33	0.46	0.56
22 - 26	0.0120	1.027	1.014	0.39	0.45	0.59
26 - 30	0.00915	1.017	1.009	0.45	0.50	0.68
30 - 34	0.00724	1.013	1.007	0.51	0.75	0.91
34 - 38	0.00579	1.005	1.004	0.58	0.80	0.98
38 - 42	0.00461	1.004	1.003	0.63	1.16	1.32
42 - 46	0.00379	1.000	1.002	0.66	1.22	1.38
46 - 50	0.00313	0.998	0.999	0.74	0.92	1.18
50 - 54	0.00258	0.994	0.999	0.80	0.96	1.25
54 - 60	0.00210	0.994	0.998	0.80	0.89	1.19
60 - 70	0.00147	0.990	0.998	0.74	0.91	1.17
70 - 80	0.000983	0.985	0.993	0.88	1.10	1.40
80 - 100	0.000542	0.984	0.993	0.83	1.07	1.35
100 - 150	0.000191	0.977	0.987	0.84	1.16	1.43
150 - 200	4.95e-05	0.970	0.985	1.62	1.83	2.45
200 - 300	1.07e-05	0.965	0.984	2.55	3.11	4.03
300 - 800	4.02e-07	0.947	0.978	5.84	8.18	10.05

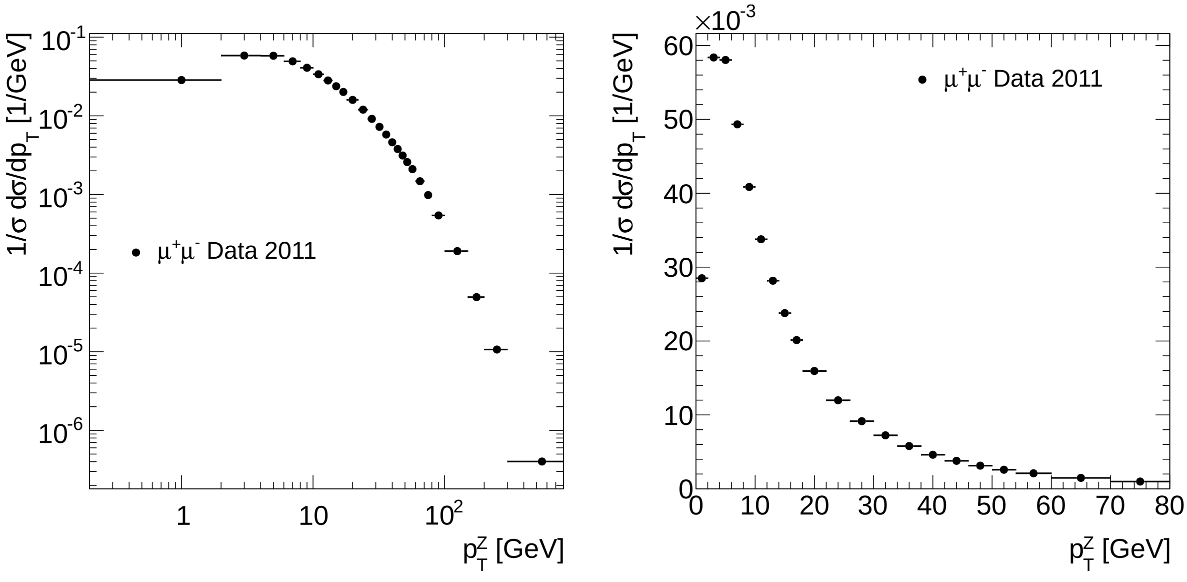

(a) (b)

Figure 8.1: The normalised differential cross section $1/\sigma d\sigma/dp_{\mathrm{T}}$ in bins of p_{T}^{Z} for $Z \to \mu^{+}\mu^{-}$ events, (a) for the full p_{T}^{Z} range; (b) for the region $p_{\mathrm{T}}^{Z} < 80\,\mathrm{GeV}$. The combined statistical and systematic uncertainty is smaller than the markers showing the data points.

by the leading order event generator PYTHIA 6.4. PYTHIA is used here with MRST LO* parton distributions [48] and with a p_{T} ordered parton shower using two different settings. The MC10 set was tuned to the p_{T}^{Z} distribution from the Tevatron [72], while the MC11 version includes a first tuning to ATLAS jet data [73]. A difference of 15% at low p_{T}^{Z} and 20% at high p_{T}^{Z} to the data can be observed for PYTHIA MC10. The newer tuning of PYTHIA MC11 shows a worse agreement with the data.

Another class of generators adds tree level diagrams with a fixed number of additional outgoing partons. The ALPGEN generator provides a prediction from the calculation of tree level matrix elements for the production of Z bosons with up to 5 additional outgoing partons. It is interfaced to HERWIG [50] for the parton shower, and uses CTEQ6L1 parton distributions [19]. The ALPGEN prediction shows a 10-30% difference to the data.

The generators POWHEG and MC@NLO use matrix element calculations at next-to-leading order and match these to parton shower algorithms. These NLO event generators include the matrix elements for the processes $pp \to Zg$ and $pp \to Zq$, which should describe accurately hard radiations, while the region of soft and collinear radiations is described by the parton shower. The POWHEG generator is used with the parton shower provided by PYTHIA, and MC@NLO is used with the parton shower from HERWIG [50]. Both generators were used with the CT10 parton distributions [18]. The POWHEG prediction underestimates the data by up to 25% at low and high p_{T}^{Z}. MC@NLO agrees with the data at low p_{T}^{Z} but is significantly lower than the data for $p_{\mathrm{T}} > 30\,\mathrm{GeV}$.

The state-of-the art in the calculation of the perturbative corrections for the $pp \to Z$ process is NNLO precision, that is up to $\mathcal{O}(\alpha_s^2)$. For the moment these predictions have

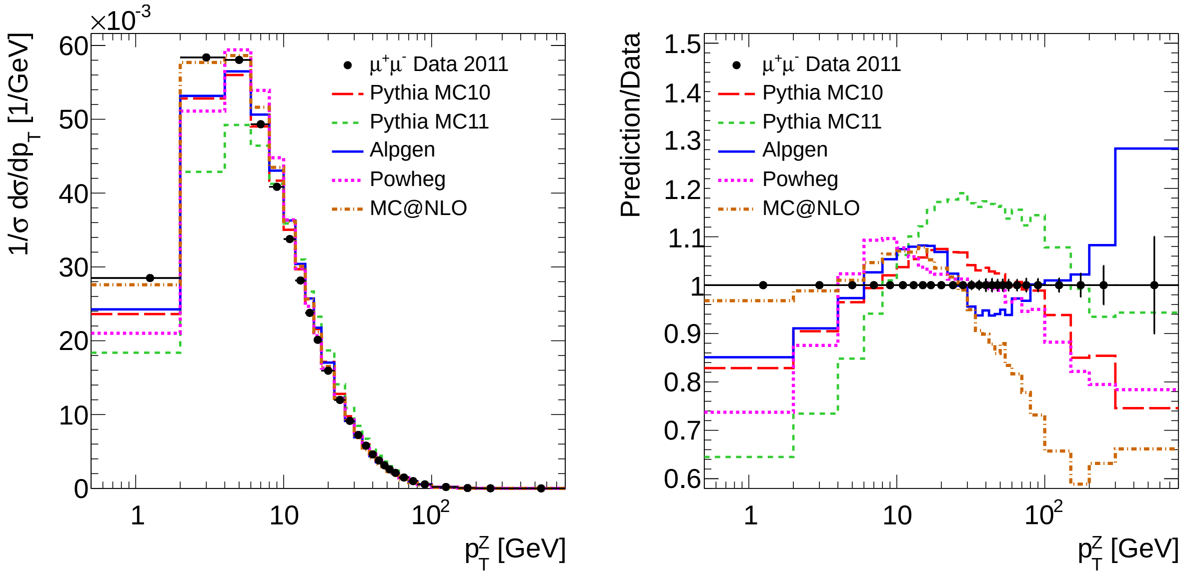

Figure 8.2: Comparison between common MC generators used in hadron collisions using either LO plus PS (Pythia), NLO plus PS (Mc@nlo and Powheg) or multi leg LO + PS predictions (Alpgen) and data at Born level. (a) $1/\sigma d\sigma/dp_{\mathrm{T}}$ (b) Ratio of the predictions to data. The error bars indicate the size of the combined statistical and systematic uncertainty of the measurement.

not yet been matched to parton shower algorithms, but comparisons can be carried out at parton level. However, these fixed order perturbative predictions are not valid for $p_{\mathrm{T}}^{Z} \rightarrow 0$, because of terms proportional to $\alpha_S^n \ln^m(M^2/p_{\mathrm{T}}^2)$, with $m \leq 2n-1$ appearing at each order n of α_S in the perturbative expansion, which cause the fixed order prediction to diverge at each individual order [24]. An implementation of a fixed order prediction at $\mathcal{O}(\alpha_s^2)$ is given by the Fewz 2.1 program [74]. The Fewz predictions were obtained with various PDF sets: CT10, HERAPDF 1.5, JR09, MSTW2008, NNPDF 2.3 and ABM11. The ratio of the Fewz prediction for each PDF set to the measured normalised cross section is shown in Fig. 8.3a. At the lowest p_{T}^{Z} the fixed order prediction is not valid, therefore the Fewz prediction is shown only for $p_{\mathrm{T}}^{Z} > 8\,\mathrm{GeV}$. An uncertainty on the prediction was calculated from the 68% confidence interval of the PDF uncertainties and from the strong coupling uncertainty. Scale uncertainties have not been evaluated for this particular calculation, but are known to be around 7% [1]. The Fewz predictions underestimate the data by about 8%.

Perturbative QCD predictions that are valid for the region of $p_{\mathrm{T}}^{Z} \ll M$ are obtained by resummation of the leading logarithmic terms $\alpha_S^n \ln^m(M^2/p_{\mathrm{T}}^2)$ in the perturbative expansion. Predictions are available based on the Collins-Soper-Sterman formalism where the cross section is expanded in the Fourier space of p_{T}^{Z} space and all leading logarithmic contributions are resummed into a form factor [25]. The QCD prediction by A. Banfi *et al.* [75] performs the resummation of the leading contributions up to next-to-next-to-leading logarithms (NNLL) and matches the calculation with the next-to-leading order QCD calculation from MCFM [76]. This result uses the CTEQ6m parton density functions. The uncertainty on the prediction was evaluated by varying the resummation, renormalisation and factorisation scales μ_Q, μ_R, μ_F between $m_Z/2$ and $2m_Z$, with the constraints $1/2 \leq \mu_i/\mu_j \leq 2$ and

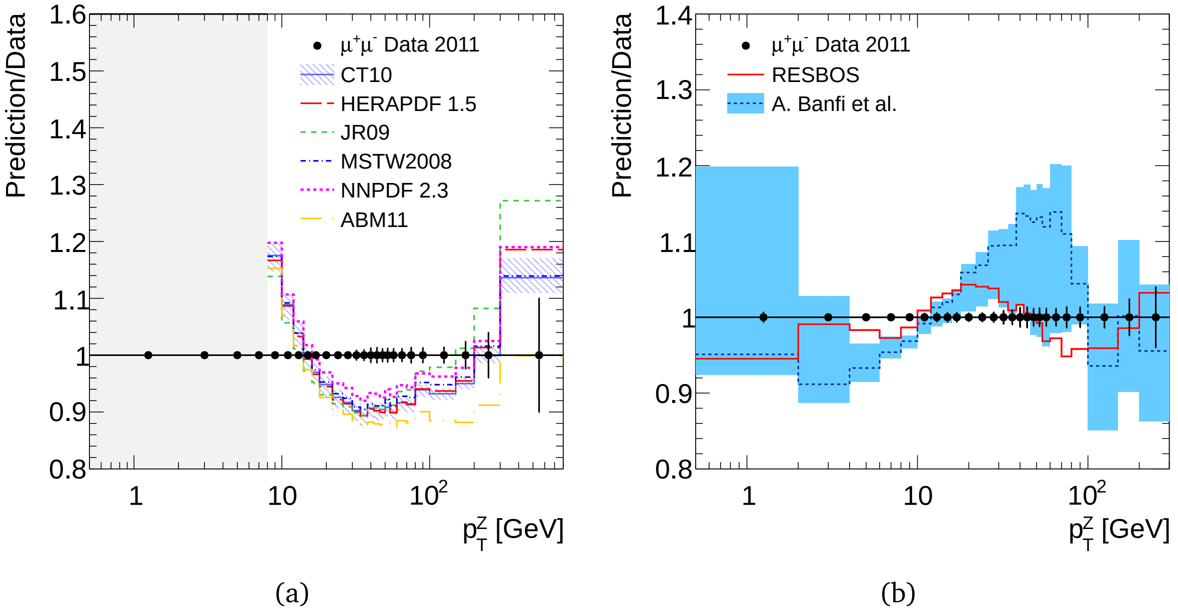

(a) (b)

Figure 8.3: Comparison of QCD predictions which use (a) $\mathcal{O}(\alpha_S^2)$ calculations (Fewz) and (b) p_{T}-resummed predictions with a non-perturbative form factor (Resbos) and without (Banfi *et al.*) with the measured normalised cross section $1/\sigma d\sigma/dp_{\mathrm{T}}$ in bins of p_{T}^{Z}. The Fewz prediction is shown for several PDFs. For the prediction using the CT10 PDF the uncertainty due to PDF variations is shown by the dashed band. The diverging part for $p_{\mathrm{T}}^{Z} < 8$ GeV is not shown. The Resbos prediction (solid line) and the prediction by Banfi *et al.*, for which the theoretical uncertainty is shown as a shaded band, were both produced with an upper limit on p_{T}^{Z} that does not include the last measured bin, which is therefore not shown. The error bars indicate the size of the combined statistical and systematic uncertainty of the measurement.

$\mu_F/\mu_Q \geq 1$, where $i,j \in F,Q,R$. The Resbos program also provides predictions using resummation at NNLL accuracy which are matched to fixed order calculation at $\mathcal{O}(\alpha_s)$ [77–79]. Resbos includes a non-perturbative correction, with parameters fitted to Drell-Yan and Z production data [80]. The ratio of the prediction from Resbos as well as the Banfi *et al.* prediction to the measured normalised differential cross section as a function of p_{T}^{Z} is shown in Fig. 8.3b. Resbos describes the data within 5% over the measured p_{T}^{Z} range. The prediction from A. Banfi *et al.* provides a worse description than Resbos, underestimating the data by 5-8% for $p_{\mathrm{T}}^{Z} < 10$ GeV and overestimating the data by up to 15% for $p_{\mathrm{T}}^{Z} > 10$ GeV. The agreement at values of $p_{\mathrm{T}}^{Z} > 100$ GeV is good.

The measured cross section is about one order more precise than the theoretical predictions, thus presenting a stringent test of perturbative QCD, perturbative QCD with non-perturbative form factors (Resbos) and of perturbative QCD coupled with the parton shower approach. The perturbative QCD calculations need to include resummation to be able to describe the low p_{T}^{Z} region. The theoretical uncertainty evaluated via scale variations are large, however significant differences between the measurement and prediction are observed. The Resbos prediction, which includes a non-perturbative contribution provides the best description of the cross section. The NNLO prediction from Fewz underestimates the data by about the same amount as the uncertainty due to scale variations. The scale uncertainties dominate effects from different parton distributions. Unlike the total cross section and the differential cross section in rapidity of Z production, the transverse momentum distribution is not directly sensitive to the parton distributions.

Different strategies for MC generators can be tested against the measurement, none are able to describe the cross section as well as RESBOS. A good description over the largest p_{T}^{Z} range is provided by the multi leg generator ALPGEN. The NLO generators MC@NLO and POWHEG do not describe the cross section better than PYTHIA, but there are substantial differences between their predictions at high/low p_{T}^{Z}. The behaviour of the prediction of the LO generator PYTHIA shows that by careful tuning of shower parameters it is in principle possible to describe the p_{T}^{Z} distribution with the parton shower approach. Such an attempt is described in Ref. [81] based on the published ATLAS measurement of the Z-transverse momentum spectrum using lower statistics ($35\,\mathrm{pb}^{-1}$) [1].

8.2 $1/\sigma d\sigma/dp_{\mathrm{T}}$ in $|y_Z|$ regions

The measurement of the normalised differential cross section $1/\sigma d\sigma/dp_{\mathrm{T}}$ was repeated in three rapidity regions, $|y_Z| < 1$, $1 < |y_Z| < 2$ and $2 < |y_Z| < 2.4$. In each region, the cross section is normalised to the inclusive cross section in this respective y_Z bin, in order to facilitate a comparison of the shapes. The normalised differential cross section at Born level in bins of p_{T}^{Z} and in three $|y_Z|$ regions is listed in Table 8.2, together with the statistical and systematic uncertainties in each p_{T}^{Z} bin. The uncertainties in the two central y_Z regions are similar to the uncertainties of the inclusive measurement. In the forward region the statistical precision decreases significantly. In addition, the uncertainty estimation for the MC generator dependence is dominated by the lack of statistics in the alternative MC sample, which more than doubles the uncertainty in most bins. Figure 8.4 shows a comparison between the cross sections in the three y_Z bins as well as the ratio to the cross section inclusive in y_Z. Only a small change can be observed between the two central y_Z regions, while in the region $2 < |y_Z| < 2.4$ the p_{T}^{Z} distribution is significantly broadened.

The amount of broadening of the p_{T}^{Z} distribution with increasing y_Z can be correctly described by the RESBOS prediction, as is shown in Fig. 8.5. The RESBOS prediction employs a non-perturbative form-factor, which is obtained from a fit to the transverse momentum distributions in Drell-Yan and Z production data [80]. In the prediction shown here, the form factor used does not depend on parton x, therefore it is the same for the prediction in all y bins. It was suggested in Ref. [82] that this form factor needs to be changed for low x values, following the observation that the transverse momentum distribution of hadrons produced in deep-inelastic scattering at HERA could be described by resummed QCD predictions with a broadening of the non-perturbative form factor for low x processes [83]. In contrast, this measurement allows the conclusion that the non-perturbative form factor used in RESBOS does not need to be adapted for low x values. This conclusion agrees with the conclusion drawn from the measurement of the transverse momentum distribution of Z bosons at the Tevatron [84]. Further, the measurement of $1/\sigma d\sigma/dp_{\mathrm{T}}$ in y_Z regions

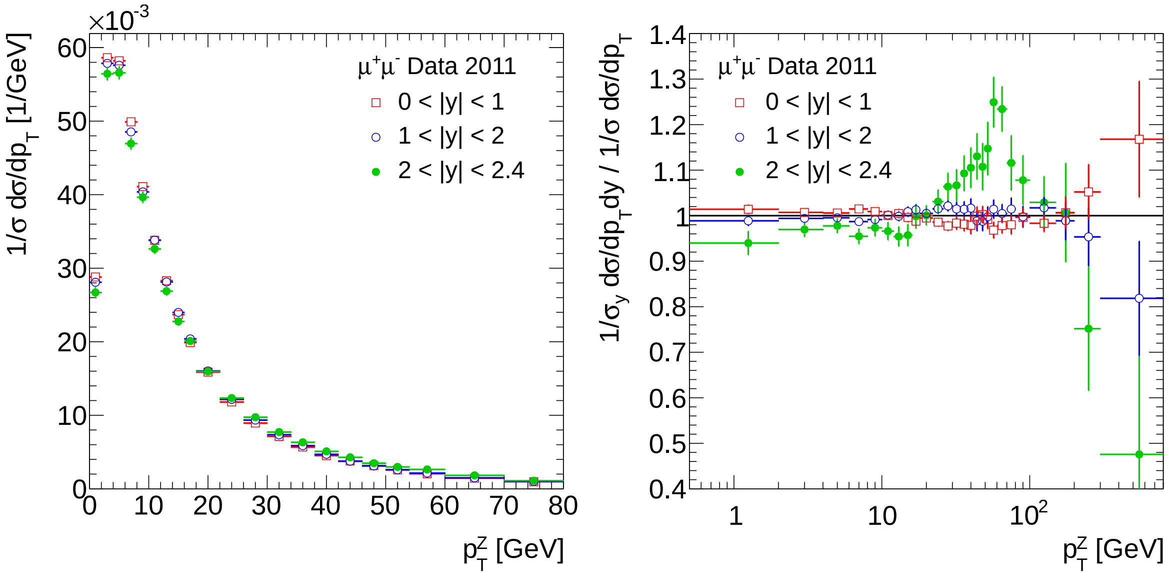

(a) (b)

Figure 8.4: Normalised differential cross section $1/\sigma d\sigma/dp_{\mathrm{T}}$ at Born level in bins of p_{T}^{Z} and in three $|y_Z|$ regions for $Z \rightarrow \mu^+\mu^-$ events. (a) Comparison of the normalised cross sections in the rapidity bins $|y_Z| < 1$, $1 < |y_Z| < 2$ and $2 < |y_Z| < 2.4$ for the region $p_{\mathrm{T}}^{Z} < 80\,\mathrm{GeV}$. (b) Ratio of the normalised cross section in y_Z bins to the normalised cross section inclusive in y_Z.

provides an important input to parton shower tuning efforts for MC event generators.

Table 8.2: The normalised differential cross section $1/\sigma d\sigma/dp_{\mathrm{T}}$ at Born level in bins of p_{T}^{Z} and in three $\lvert y_Z \rvert$ regions for $Z \rightarrow \mu^{+}\mu^{-}$ events. Correction factors for the cross section at the level of bare and dressed final state muons are given. The statistical (δ_{stat}) and total systematic (δ_{sys}) uncertainties are given in percent.

	$0 < \lvert y_{\mathrm{Z}} \rvert < 1$			$1 < \lvert y_{\mathrm{Z}} \rvert < 2$			$2 < \lvert y_{\mathrm{Z}} \rvert < 2.4$		
p_{T}^{Z} (GeV)	$\frac{1}{\sigma^{\mathrm{fid}}}\frac{d\sigma^{\mathrm{fid}}}{dp_{\mathrm{T}}}$ (1/GeV)	δ_{stat} (%)	δ_{sys} (%)	$\frac{1}{\sigma^{\mathrm{fid}}}\frac{d\sigma^{\mathrm{fid}}}{dp_{\mathrm{T}}}$ (1/GeV)	δ_{stat} (%)	δ_{sys} (%)	$\frac{1}{\sigma^{\mathrm{fid}}}\frac{d\sigma^{\mathrm{fid}}}{dp_{\mathrm{T}}}$ (1/GeV)	δ_{stat} (%)	δ_{sys} (%)
0 - 2	0.0289	0.49	0.66	0.0282	0.52	1.2	0.0268	1.7	7.8
2 - 4	0.0588	0.31	0.51	0.0580	0.32	0.61	0.0566	0.98	3.9
4 - 6	0.0584	0.31	0.47	0.0578	0.33	0.56	0.0567	0.99	3.0
6 - 8	0.0501	0.36	0.48	0.0487	0.35	0.61	0.0471	1.1	3.5
8 - 10	0.0412	0.38	0.51	0.0405	0.38	0.54	0.0398	1.2	2.8
10 - 12	0.0338	0.42	0.59	0.0338	0.42	0.56	0.0326	1.3	2.5
12 - 14	0.0283	0.48	0.63	0.0281	0.48	0.72	0.0269	1.4	4.1
14 - 16	0.0237	0.50	0.68	0.0240	0.52	0.77	0.0228	1.6	2.5
16 - 18	0.0199	0.56	0.64	0.0204	0.58	0.75	0.0201	1.7	3.2
18 - 22	0.0159	0.46	0.57	0.0160	0.50	0.63	0.0160	1.5	10
22 - 26	0.0118	0.56	0.58	0.0122	0.57	0.62	0.0123	1.8	2.9
26 - 30	0.00894	0.62	0.67	0.00935	0.65	0.79	0.00973	2.0	3.7
30 - 34	0.00712	0.73	0.90	0.00735	0.76	1.0	0.00772	2.3	4.7
34 - 38	0.00568	0.79	0.97	0.00587	0.80	1.1	0.00633	2.5	6.0
38 - 42	0.00451	0.90	1.4	0.00468	0.91	1.4	0.00509	2.6	5.1
42 - 46	0.00378	0.95	1.4	0.00374	1.0	1.5	0.00428	2.9	5.3
46 - 50	0.00314	1.0	1.3	0.00309	1.1	1.4	0.00347	3.1	5.8
50 - 54	0.00256	1.2	1.3	0.00257	1.2	1.8	0.00296	3.5	4.7
54 - 60	0.00203	1.1	1.2	0.00213	1.1	1.4	0.00262	3.2	5.2
60 - 70	0.00144	0.98	1.2	0.00148	1.1	1.2	0.00182	3.0	5.6
70 - 80	0.000963	1.2	1.4	0.000997	1.4	1.7	0.00110	4.1	6.8
80 - 100	0.00054	1.1	1.4	0.00054	1.3	1.5	0.000584	3.9	6.4
100 - 150	0.000187	1.1	1.4	0.000194	1.3	1.6	0.000196	4.2	7.4
150 - 200	4.98e-05	2.3	2.7	4.9e-05	2.7	3.3	4.99e-05	8.8	9.4
200 - 300	1.12e-05	3.5	3.6	1.02e-05	4.1	9.5	8.03e-06	14	15
300 - 800	4.7e-07	7.4	12	3.29e-07	11	19	1.91e-07	48	21

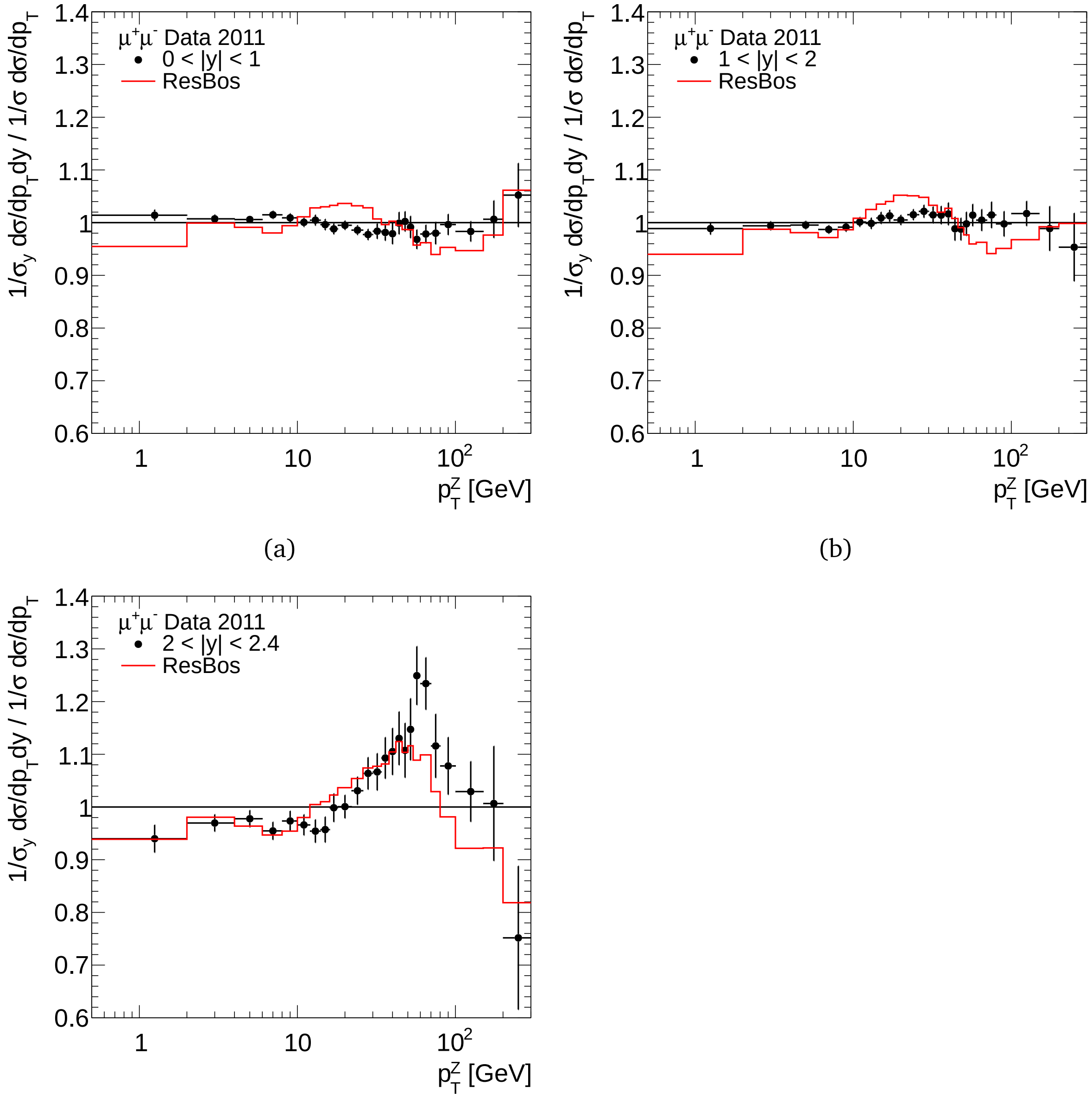

(a)

(b)

(c)

Figure 8.5: Ratio of the normalised differential cross section $1/\sigma d\sigma/dp_{\mathrm{T}}$ at Born level in bins of p_{T}^Z for each of the three $|y_Z|$ regions to the normalised differential cross section in bins of p_{T}^Z and inclusive in y_Z and comparison with the same ratio using the RESBOS prediction. (a) $|y_Z| < 1$; (b) $1 < |y_Z| < 2$; (c) $2 < |y_Z| < 2.4$.

Chapter 9

Summary and conclusions

This thesis presents a measurement of the transverse momentum distribution of Z bosons produced in pp collisions at $\sqrt{s} = 7\,\text{TeV}$. A total of 1.8 million events with Z boson candidates decaying to two muons are selected in the data recorded with the ATLAS detector in 2011 with a corresponding integrated luminosity of $4.7\,\text{fb}^{-1}$. The large data set allows to measure the normalised differential cross section $1/\sigma d\sigma/dp_\text{T}$ in bins of p_T^Z with good precision up to 800 GeV. It is also possible to subdivide the data in three $|y_Z|$-intervals. The uncertainty on $1/\sigma d\sigma/dp_\text{T}$ is smaller than 1.5% for the range of $p_\text{T}^Z < 150\,\text{GeV}$. Thanks to the excellent performance of the ATLAS detector the experimental sources of systematic uncertainty are very well under control. The very good knowledge of the muon momentum scale and resolution in particular reduce the related uncertainty. The largest remaining experimental source of systematic uncertainty is the modelling of the reconstruction and isolation efficiencies as a function p_T^Z. The largest contribution to the systematic uncertainty comes from the theoretical modelling of events needed to unfold the data to parton level.

The measured cross section $1/\sigma d\sigma/dp_\text{T}$ is compared with the predictions of common event generators for hadron collisions: PYTHIA, ALPGEN, MC@NLO and POWHEG. It is found that none of the generators are able to describe the spectrum over the entire p_T^Z range. The multi leg generator ALPGEN, which includes the tree level matrix elements for the production of Z bosons accompanied by up to 5 partons, provides a good description over the largest p_T^Z range of the tested generators. The NLO generators MC@NLO, used with the HERWIG parton shower and POWHEG, used with the PYTHIA parton shower, exhibit substantial differences between their predictions at high/low p_T^Z and the data. The prediction of the lowest order using the PYTHIA parton shower is not worse compared with the NLO generators.

The fixed order result at $\mathcal{O}(\alpha_s^2)$ of FEWZ 2.1 is found to provide a reliable prediction for $p_\text{T}^Z > 10\,\text{GeV}$, but it underestimates the data by about 8% in the region $14\ldots150\,\text{GeV}$.

A good description of the data is provided by two predictions that use resummation of the leading contributions $\alpha_s^n \ln^m(M^2/p_\text{T}^2)$ up to next-to-next-to-leading logarithms (NNLL) to describe the low p_T^Z region and match the result to NLO calculations for the high p_T^Z region. The purely perturbative prediction of Ref. [75] comes with a theoretical uncertainty originating from variations of the factorisation, renormalisation and resummation scales that is about one order of magnitude larger than the measurement uncertainty. Given that the techniques employed in this prediction are state-of-the-art, the presented measurement provides a good challenge to further improve the theoretical description. The best description of the data is provided by the RESBOS generator, which includes an additional non-perturbative form factor in the description.

The transverse momentum distribution $1/\sigma d\sigma/dp_{\mathrm{T}}$ is also presented in three $|y_Z|$-intervals. It is observed that the p_{T} distribution is shifted to higher values with increasing rapidity. The effect can be described by the RESBOS prediction using the same non-perturbative form factor for all y_Z-intervals. The large effect of additional low x broadening of the form factor predicted in Ref. [82] was not observed.

The obtained results will be combined with the equivalent measurement in the $Z \rightarrow e^+e^-$ decay channel, allowing to further reduce the uncertainty to better than 1% for $p_{\mathrm{T}}^Z < 150\,\mathrm{GeV}$. The measured cross sections provide an important input to the tuning of parton shower event generators. The improved description of the event kinematics in Z production, which also relates to the description of W production, will help precision measurements of W and Z properties at the LHC, as well as for new physics searches, where W and Z boson production are background processes. One direct application of the result is in the W mass measurement, where the transverse momentum distribution of W bosons can be modelled more precisely using the results measured in this thesis.

Appendix A

Dimuon invariant mass distributions

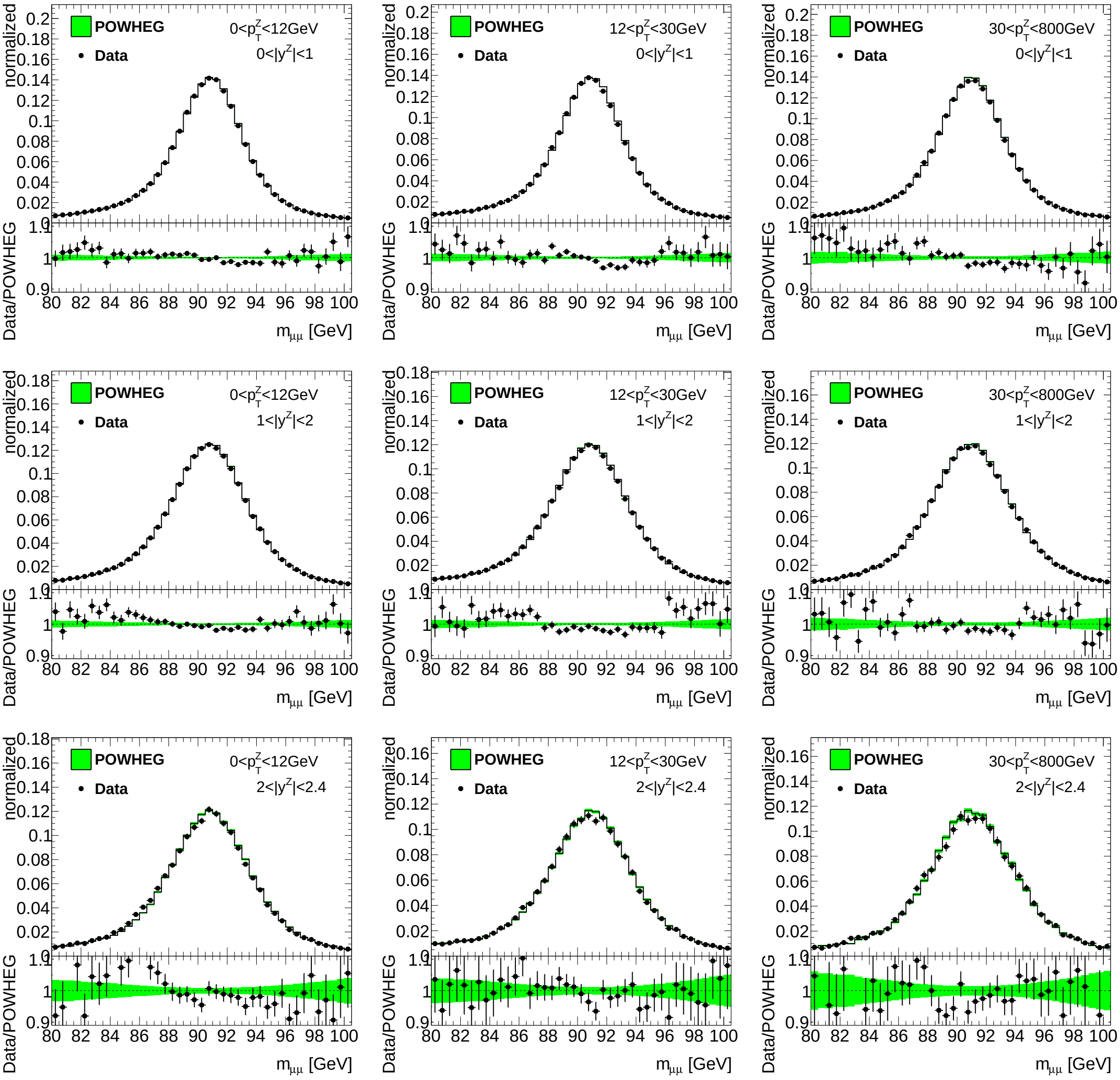

Figure A.1: Comparison of the dimuon invariant mass distribution in data with simulation. Data are shown as solid points, simulation as solid line. The green band shows the uncertainty on the simulation, due to uncertainty on the muon scale and resolution.

Appendix B

Uncertainties of the measurement in rapidity regions

This appendix lists the uncertainties for the measurement of $1/\sigma d\sigma/dp_{\mathrm{T}}dy$. The calculation of the uncertainties is equivalent to the description in Chapter 7 for $1/\sigma d\sigma/dp_{\mathrm{T}}$. For the bin $|y| < 1$ the uncertainties are listed in Table B.1, for $1 < |y| < 2$ in Table B.2, and for $2 < |y| < 2.4$ in Table B.3. The size of the relative uncertainties is illustrated in Figures B.1, B.2 and B.3.

	Momentum			Efficiency					Theory				
p_{T} (GeV)	Resol. (%)	Scale (%)	ϵ_{muid} (%)	ϵ_{ID} (%)	ϵ_{iso} (%)	ϵ_{trig} (%)	Bkg. (%)	p_{T} shape (%)	Generator (%)	MC stat. (%)	Sys. (%)	Stat. (%)	Total (%)
0.0-2.0	0.07	0.16	0.09	0.06	0.33	0.05	0.02	0.03	0.52	0.09	0.66	0.49	0.83
2.0-4.0	0.03	0.17	0.09	0.06	0.33	0.05	0.02	0.03	0.33	0.06	0.51	0.31	0.60
4.0-6.0	0.02	0.11	0.11	0.07	0.28	0.09	0.02	0.01	0.32	0.06	0.47	0.31	0.57
6.0-8.0	0.02	0.02	0.11	0.07	0.28	0.09	0.01	0.01	0.35	0.06	0.48	0.36	0.60
8.0-10.0	0.03	0.05	0.16	0.10	0.27	0.04	0.01	0.01	0.38	0.07	0.51	0.38	0.64
10.0-12.0	0.04	0.03	0.16	0.10	0.27	0.04	0.01	0.01	0.48	0.08	0.59	0.42	0.73
12.0-14.0	0.05	0.07	0.41	0.07	0.07	0.09	0.01	0.04	0.44	0.08	0.63	0.48	0.79
14.0-16.0	0.03	0.03	0.41	0.07	0.07	0.09	0.01	0.04	0.52	0.08	0.68	0.50	0.85
16.0-18.0	0.03	0.04	0.18	0.08	0.27	0.09	0.02	0.03	0.53	0.10	0.64	0.56	0.85
18.0-22.0	0.01	0.09	0.18	0.08	0.27	0.09	0.02	0.03	0.44	0.08	0.57	0.46	0.73
22.0-26.0	0.03	0.10	0.20	0.08	0.09	0.07	0.02	0.08	0.50	0.09	0.58	0.56	0.80
26.0-30.0	0.04	0.09	0.20	0.08	0.09	0.07	0.02	0.08	0.60	0.10	0.67	0.62	0.91
30.0-34.0	0.05	0.13	0.54	0.10	0.21	0.06	0.02	0.02	0.65	0.13	0.90	0.73	1.16
34.0-38.0	0.05	0.14	0.54	0.10	0.21	0.06	0.02	0.02	0.75	0.14	0.97	0.79	1.25
38.0-42.0	0.06	0.22	0.95	0.27	0.21	0.08	0.03	0.01	0.86	0.16	1.36	0.90	1.63
42.0-46.0	0.06	0.21	0.95	0.27	0.21	0.08	0.03	0.01	0.91	0.16	1.39	0.95	1.68
46.0-50.0	0.10	0.19	0.47	0.15	0.33	0.10	0.04	0.00	1.09	0.19	1.28	1.02	1.64
50.0-54.0	0.10	0.15	0.47	0.15	0.33	0.10	0.04	0.00	1.09	0.20	1.28	1.19	1.74
54.0-60.0	0.03	0.19	0.38	0.15	0.43	0.09	0.05	0.02	0.99	0.20	1.19	1.09	1.61
60.0-70.0	0.07	0.26	0.38	0.15	0.43	0.09	0.08	0.02	0.96	0.18	1.18	0.98	1.53
70.0-80.0	0.14	0.17	0.24	0.33	0.50	0.10	0.11	0.15	1.14	0.21	1.36	1.24	1.84
80.0-100.0	0.05	0.27	0.24	0.33	0.50	0.10	0.14	0.15	1.13	0.20	1.37	1.11	1.76
100.0-150.0	0.03	0.23	0.54	0.23	0.43	0.14	0.13	0.14	1.14	0.21	1.41	1.07	1.77
150.0-200.0	0.21	0.28	0.54	0.23	0.43	0.14	0.09	0.14	2.57	0.47	2.74	2.33	3.60
200.0-300.0	0.27	0.20	0.67	1.46	0.53	0.43	0.08	0.65	3.02	0.70	3.63	3.47	5.03
300.0-800.0	0.52	0.84	0.67	1.46	0.53	0.43	0.10	0.65	11.18	1.78	11.51	7.36	13.66

Table B.1: Systematic uncertainties on $1/\sigma d\sigma/dp_{\mathrm{T}}dy$ for $0 < |y| < 1$.

	Momentum		Efficiency					Theory					
p_{T} (GeV)	Resol. (%)	Scale (%)	ϵ_{muid} (%)	ϵ_{ID} (%)	ϵ_{iso} (%)	ϵ_{trig} (%)	Bkg. (%)	p_{T} shape (%)	Generator (%)	MC stat. (%)	Sys. (%)	Stat. (%)	Total (%)
0.0-2.0	0.28	0.30	0.09	0.06	0.33	0.05	0.01	0.08	1.02	0.09	1.16	0.52	1.27
2.0-4.0	0.16	0.23	0.09	0.06	0.33	0.05	0.01	0.08	0.41	0.05	0.61	0.32	0.69
4.0-6.0	0.07	0.11	0.11	0.07	0.28	0.09	0.01	0.10	0.42	0.05	0.56	0.33	0.65
6.0-8.0	0.05	0.11	0.11	0.07	0.28	0.09	0.01	0.10	0.49	0.05	0.61	0.35	0.71
8.0-10.0	0.10	0.10	0.16	0.10	0.27	0.04	0.01	0.04	0.40	0.06	0.54	0.38	0.67
10.0-12.0	0.11	0.08	0.16	0.10	0.27	0.04	0.01	0.04	0.42	0.06	0.56	0.42	0.70
12.0-14.0	0.08	0.04	0.41	0.07	0.07	0.09	0.01	0.03	0.57	0.07	0.72	0.48	0.86
14.0-16.0	0.07	0.05	0.41	0.07	0.07	0.09	0.01	0.03	0.63	0.08	0.77	0.52	0.93
16.0-18.0	0.02	0.08	0.18	0.08	0.27	0.09	0.01	0.05	0.65	0.09	0.75	0.58	0.95
18.0-22.0	0.07	0.08	0.18	0.08	0.27	0.09	0.01	0.05	0.51	0.07	0.63	0.50	0.80
22.0-26.0	0.06	0.10	0.20	0.08	0.09	0.07	0.01	0.05	0.55	0.08	0.62	0.57	0.84
26.0-30.0	0.09	0.21	0.20	0.08	0.09	0.07	0.01	0.05	0.71	0.09	0.79	0.65	1.02
30.0-34.0	0.13	0.17	0.54	0.10	0.21	0.06	0.01	0.03	0.77	0.10	1.00	0.76	1.26
34.0-38.0	0.08	0.24	0.54	0.10	0.21	0.06	0.01	0.03	0.83	0.11	1.05	0.80	1.32
38.0-42.0	0.06	0.11	0.95	0.27	0.21	0.08	0.02	0.11	0.97	0.13	1.42	0.91	1.68
42.0-46.0	0.09	0.25	0.95	0.27	0.21	0.08	0.02	0.11	1.12	0.14	1.54	1.01	1.84
46.0-50.0	0.20	0.30	0.47	0.15	0.33	0.10	0.02	0.04	1.15	0.17	1.36	1.06	1.73
50.0-54.0	0.14	0.24	0.47	0.15	0.33	0.10	0.03	0.04	1.61	0.18	1.75	1.19	2.12
54.0-60.0	0.07	0.13	0.38	0.15	0.43	0.09	0.04	0.06	1.22	0.16	1.38	1.12	1.77
60.0-70.0	0.06	0.37	0.38	0.15	0.43	0.09	0.04	0.06	1.00	0.15	1.24	1.09	1.65
70.0-80.0	0.08	0.40	0.24	0.33	0.50	0.10	0.06	0.14	1.51	0.19	1.71	1.37	2.19
80.0-100.0	0.09	0.47	0.24	0.33	0.50	0.10	0.08	0.14	1.29	0.19	1.54	1.33	2.04
100.0-150.0	0.07	0.43	0.54	0.23	0.43	0.14	0.08	0.13	1.38	0.19	1.65	1.26	2.07
150.0-200.0	0.13	0.64	0.54	0.23	0.43	0.14	0.07	0.13	3.16	0.41	3.34	2.72	4.31
200.0-300.0	0.39	0.83	0.67	1.46	0.53	0.43	0.07	1.37	9.16	0.64	9.49	4.15	10.36
300.0-800.0	1.43	2.80	0.67	1.46	0.53	0.43	0.08	1.37	18.47	2.17	18.99	10.58	21.74

Table B.2: Systematic uncertainties on $1/\sigma d\sigma/dp_{\mathrm{T}}dy$ for $1 < |y| < 2$.

	Momentum			Efficiency				Theory					
p_{T} (GeV)	Resol. (%)	Scale (%)	ϵ_{muid} (%)	ϵ_{ID} (%)	ϵ_{iso} (%)	ϵ_{trig} (%)	Bkg. (%)	p_{T} shape (%)	Generator (%)	MC stat. (%)	Sys. (%)	Stat. (%)	Total (%)
0.0-2.0	0.95	0.17	0.09	0.06	0.33	0.05	0.01	0.16	7.68	0.26	7.75	1.68	7.93
2.0-4.0	0.36	0.15	0.09	0.06	0.33	0.05	0.01	0.16	3.90	0.16	3.94	0.98	4.06
4.0-6.0	0.12	0.10	0.11	0.07	0.28	0.09	0.01	0.18	3.02	0.15	3.05	0.99	3.21
6.0-8.0	0.20	0.05	0.11	0.07	0.28	0.09	0.01	0.18	3.51	0.17	3.54	1.07	3.69
8.0-10.0	0.31	0.06	0.16	0.10	0.27	0.04	0.01	0.07	2.75	0.18	2.79	1.16	3.02
10.0-12.0	0.22	0.05	0.16	0.10	0.27	0.04	0.01	0.07	2.50	0.20	2.54	1.28	2.84
12.0-14.0	0.12	0.17	0.41	0.07	0.07	0.09	0.00	0.04	4.11	0.23	4.14	1.39	4.37
14.0-16.0	0.15	0.18	0.41	0.07	0.07	0.09	0.01	0.04	2.43	0.26	2.49	1.60	2.96
16.0-18.0	0.23	0.14	0.18	0.08	0.27	0.09	0.00	0.04	3.13	0.28	3.17	1.71	3.60
18.0-22.0	0.16	0.11	0.18	0.08	0.27	0.09	0.00	0.04	10.44	0.20	10.45	1.53	10.56
22.0-26.0	0.29	0.21	0.20	0.08	0.09	0.07	0.01	0.05	2.88	0.24	2.93	1.81	3.44
26.0-30.0	0.16	0.09	0.20	0.08	0.09	0.07	0.00	0.05	3.70	0.28	3.73	2.04	4.25
30.0-34.0	0.20	0.17	0.54	0.10	0.21	0.06	0.01	0.09	4.69	0.32	4.74	2.32	5.28
34.0-38.0	0.40	0.18	0.54	0.10	0.21	0.06	0.01	0.09	5.97	0.34	6.02	2.55	6.54
38.0-42.0	0.25	0.20	0.95	0.27	0.21	0.08	0.01	0.14	4.97	0.42	5.10	2.61	5.73
42.0-46.0	0.23	0.17	0.95	0.27	0.21	0.08	0.01	0.14	5.22	0.45	5.35	2.90	6.08
46.0-50.0	0.22	0.28	0.47	0.15	0.33	0.10	0.02	0.08	5.74	0.47	5.80	3.05	6.55
50.0-54.0	0.25	0.24	0.47	0.15	0.33	0.10	0.02	0.08	4.57	0.54	4.66	3.47	5.81
54.0-60.0	0.71	0.17	0.38	0.15	0.43	0.09	0.02	0.08	5.05	0.51	5.16	3.23	6.09
60.0-70.0	0.44	0.42	0.38	0.15	0.43	0.09	0.02	0.08	5.53	0.48	5.62	2.95	6.35
70.0-80.0	0.30	0.29	0.24	0.33	0.50	0.10	0.04	0.09	6.74	0.64	6.82	4.09	7.95
80.0-100.0	0.47	0.51	0.24	0.33	0.50	0.10	0.04	0.09	6.35	0.60	6.45	3.94	7.56
100.0-150.0	0.22	0.29	0.54	0.23	0.43	0.14	0.06	0.63	7.28	0.66	7.39	4.19	8.49
150.0-200.0	0.87	0.72	0.54	0.23	0.43	0.14	0.05	0.63	9.12	1.55	9.37	8.77	12.84
200.0-300.0	1.39	1.07	0.67	1.46	0.53	0.43	0.09	0.88	14.96	2.22	15.35	13.78	20.63
300.0-800.0	7.84	3.17	0.67	1.46	0.53	0.43	0.23	0.88	0.00	19.15	21.03	47.86	52.27

Table B.3: Systematic uncertainties on $1/\sigma d\sigma/dp_{\mathrm{T}}dy$ for $2 < |y| < 2.4$.

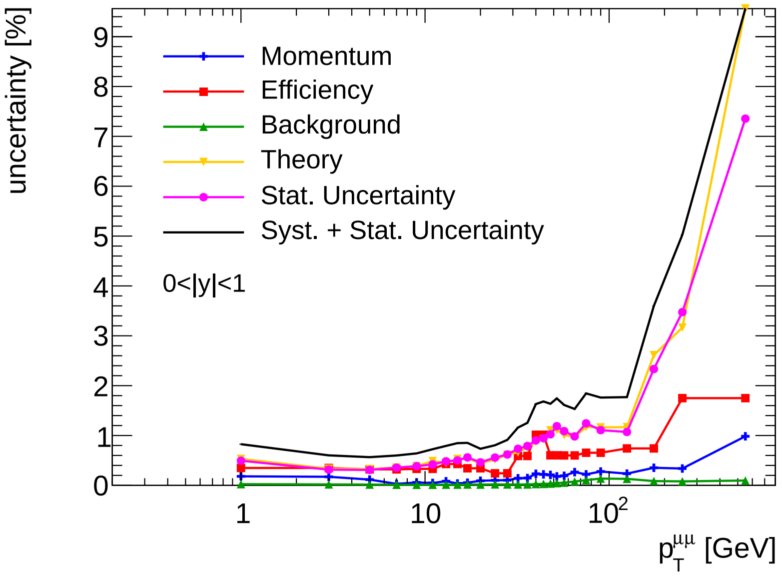

Figure B.1: Systematic uncertainties on $1/\sigma d\sigma/dp_{\mathrm{T}}dy$ for $0 < |y| < 1$, given in percent of the central value of the bin.

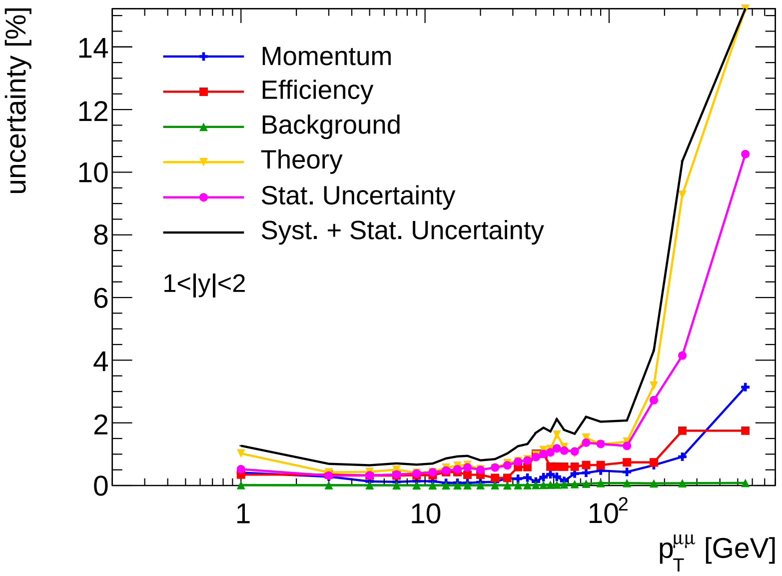

Figure B.2: Systematic uncertainties on $1/\sigma d\sigma/dp_{\mathrm{T}}dy$ for $1 < |y| < 2$, given in percent of the central value of the bin.

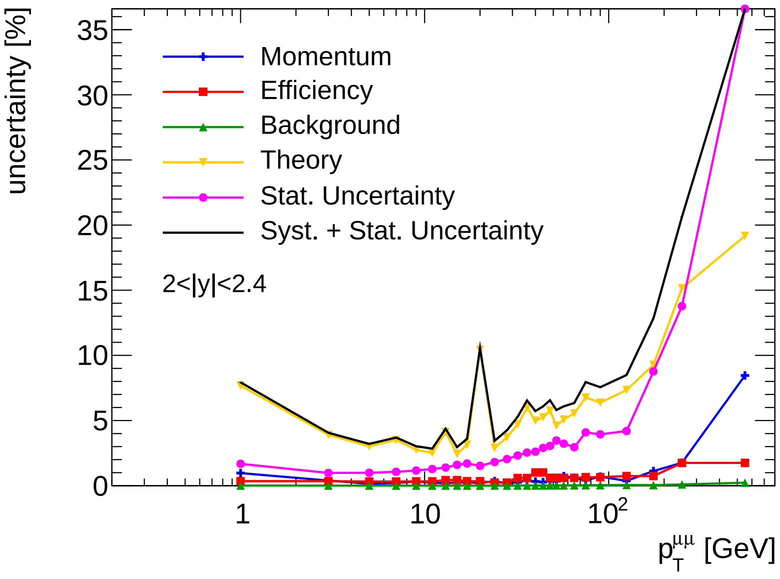

Figure B.3: Systematic uncertainties on $1/\sigma d\sigma/dp_{\mathrm{T}}dy$ for $2 < |y| < 2.4$, given in percent of the central value of the bin.

Bibliography

[1] ATLAS Collaboration, G. Aad et al., 'Measurement of the transverse momentum distribution of Z/γ^* bosons in proton-proton collisions at $\sqrt{s} = 7$ TeV with the ATLAS detector', *Phys.Lett.* B705 (2011) 415–434, arXiv: `1107.2381 [hep-ex]`.

[2] *Standard model of elementary particles*, Wikimedia Commons.

[3] F. Englert and R. Brout, 'Broken Symmetry and the Mass of Gauge Vector Mesons', *Phys.Rev.Lett.* 13 (1964) 321–323, DOI: `10.1103/PhysRevLett.13.321`.

[4] G. Guralnik, C. Hagen and T. Kibble, 'Global Conservation Laws and Massless Particles', *Phys.Rev.Lett.* 13 (1964) 585–587, DOI: `10.1103/PhysRevLett.13.585`.

[5] P. W. Higgs, 'Broken symmetries, massless particles and gauge fields', *Phys.Lett.* 12 (1964) 132–133, DOI: `10.1016/0031-9163(64)91136-9`.

[6] P. W. Higgs, 'Broken Symmetries and the Masses of Gauge Bosons', *Phys.Rev.Lett.* 13 (1964) 508–509, DOI: `10.1103/PhysRevLett.13.508`.

[7] LEP Working Group for Higgs boson searches, R. Barate et al., 'Search for the standard model Higgs boson at LEP', *Phys.Lett.* B565 (2003) 61–75, DOI: `10.1016/S0370-2693(03)00614-2`, arXiv: `hep-ex/0306033`.

[8] ALEPH Collaboration et al., 'Precision Electroweak Measurements and Constraints on the Standard Model' (2010), arXiv: `1012.2367 [hep-ex]`.

[9] ATLAS Collaboration, G. Aad et al., 'Observation of a new particle in the search for the Standard Model Higgs boson with the ATLAS detector at the LHC', *Phys.Lett.* B716 (2012) 1–29, arXiv: `1207.7214 [hep-ex]`.

[10] CMS Collaboration, S. Chatrchyan et al., 'Observation of a new boson at a mass of 125 GeV with the CMS experiment at the LHC', *Phys.Lett.* B716 (2012) 30–61, arXiv: `1207.7235 [hep-ex]`.

[11] ATLAS Collaboration, 'Updated ATLAS results on the signal strength of the Higgs-like boson for decays into WW and heavy fermion final states', ATLAS-CONF-2012-162 (2012).

[12] CMS Collaboration, 'Evidence for a particle decaying to W^+W^- in the fully leptonic final state in a standard model Higgs boson search in pp collisions at the LHC', CMS-PAS-HIG-12-042 (2012).

[13] L. Landau, ‘On the angular momentum of a two-photon system’, *Dokl.Akad.Nauk Ser.Fiz.* 60 (1948) 207–209.

[14] C.-N. Yang, ‘Selection Rules for the Dematerialization of a Particle Into Two Photons’, *Phys.Rev.* 77 (1950) 242–245, DOI: `10.1103/PhysRev.77.242`.

[15] R. K. Ellis, W. J. Stirling and B. Webber, *QCD and Collider Physics*, Cambridge Univ. Press, 1996.

[16] J. M. Campbell, J. Huston and W. Stirling, ‘Hard Interactions of Quarks and Gluons: A Primer for LHC Physics’, *Rept.Prog.Phys.* 70 (2007) 89, arXiv: `hep-ph/0611148`.

[17] D. J. Griffiths, *Introduction to Elementary Particles*, Wiley-VCH, 2008.

[18] H.-L. Lai et al., ‘New parton distributions for collider physics’, *Phys.Rev.* D82 (2010) 074024, DOI: `10.1103/PhysRevD.82.074024`, arXiv: `1007.2241 [hep-ph]`.

[19] J. Pumplin et al., ‘New generation of parton distributions with uncertainties from global QCD analysis’, *JHEP* 0207 (2002) 012, arXiv: `hep-ph/0201195`.

[20] A. Martin et al., ‘Parton distributions for the LHC’, *Eur.Phys.J.* C63 (2009) 189–285, arXiv: `0901.0002 [hep-ph]`.

[21] J. C. Collins, D. E. Soper and G. F. Sterman, ‘Factorization of Hard Processes in QCD’, *Adv.Ser.Direct.High Energy Phys.* 5 (1988) 1–91, arXiv: `hep-ph/0409313`.

[22] S. Drell and T.-M. Yan, ‘Massive Lepton Pair Production in Hadron-Hadron Collisions at High-Energies’, *Phys.Rev.Lett.* 25 (1970) 316–320.

[23] P. B. Arnold and M. H. Reno, ‘The Complete Computation of High p_{T} W and Z Production in 2nd Order QCD’, *Nucl.Phys.* B319 (1989) 37.

[24] G. Altarelli et al., ‘Vector Boson Production at Colliders: A Theoretical Reappraisal’, *Nucl.Phys.* B246 (1984) 12, DOI: `10.1016/0550-3213(84)90112-3`.

[25] J. C. Collins, D. E. Soper and G. F. Sterman, ‘Transverse Momentum Distribution in Drell-Yan Pair and W and Z Boson Production’, *Nucl.Phys.* B250 (1985) 199.

[26] G. Bozzi et al., ‘Transverse-momentum resummation and the spectrum of the Higgs boson at the LHC’, *Nucl.Phys.* B737 (2006) 73–120, DOI: `10.1016/j.nuclphysb.2005.12.022`, arXiv: `hep-ph/0508068`.

[27] G. Bozzi et al., ‘Production of Drell-Yan lepton pairs in hadron collisions: Transverse-momentum resummation at next-to-next-to-leading logarithmic accuracy’, *Phys.Lett.* B696 (2011) 207–213, arXiv: `1007.2351 [hep-ph]`.

[28] A. Buckley et al., ‘General-purpose event generators for LHC physics’, *Phys.Rept.* 504 (2011) 145–233, arXiv: `1101.2599 [hep-ph]`.

[29] L. Evans and P. Bryant (editors), 'LHC Machine', *JINST* 3 (2008) S08001, DOI: `10.1088/1748-0221/3/08/S08001`.

[30] ATLAS Collaboration, G. Aad et al., 'The ATLAS Experiment at the CERN Large Hadron Collider', *JINST* 3 (2008) S08003, DOI: `10.1088/1748-0221/3/08/S08003`.

[31] CMS Collaboration, S. Chatrchyan et al., 'The CMS experiment at the CERN LHC', *JINST* 3 (2008) S08004, DOI: `10.1088/1748-0221/3/08/S08004`.

[32] LHCb Collaboration, A. Alves et al., 'The LHCb Detector at the LHC', *JINST* 3 (2008) S08005, DOI: `10.1088/1748-0221/3/08/S08005`.

[33] ALICE Collaboration, K. Aamodt et al., 'The ALICE experiment at the CERN LHC', *JINST* 3 (2008) S08002, DOI: `10.1088/1748-0221/3/08/S08002`.

[34] ATLAS Collaboration, 'Performance of the ATLAS muon trigger in 2011', *ATLAS-CONF-2012-099* (2012).

[35] T Cornelissen et al., 'Concepts, Design and Implementation of the ATLAS New Tracking (NEWT)', ATL-SOFT-PUB-2007-007 (2007).

[36] ATLAS Collaboration, 'Performance of primary vertex reconstruction in proton-proton collisions at $\sqrt{s} = 7\,\text{TeV}$ in the ATLAS experiment', ATLAS-CONF-2010-069 (2010).

[37] ATLAS Collaboration, G. Aad et al., 'Expected Performance of the ATLAS Experiment - Detector, Trigger and Physics' (2009), arXiv: `0901.0512 [hep-ex]`.

[38] ATLAS Muon Combined Performance Group, *Guidelines for Analyses of 2011 Data in Release 17*, URL: `https://twiki.cern.ch/twiki/bin/viewauth/AtlasProtected/MCPAnalysisGuidelinesRel17MC11a`.

[39] ATLAS Muon Combined Performance Group, *Quality definitions Muid*, 2011, URL: `https://twiki.cern.ch/twiki/bin/viewauth/AtlasProtected/QualityDefinitionMuid`.

[40] J. Beringer et al. (Particle Data Group), 'Review of Particle Physics, Passage of Particles Through Matter', *Phys. Rev. D* 86 (1 2012), DOI: `10.1103/PhysRevD.86.010001`.

[41] A. Salvucci, 'Measurement of muon momentum resolution of the ATLAS detector', *EPJ Web Conf.* 28 (2012) 12039, arXiv: `1201.4704 [physics.ins-det]`.

[42] ATLAS Collaboration, 'Determination of the muon reconstruction efficiency in ATLAS at the Z resonance in proton-proton collisons at $\sqrt{s} = 7\,\text{TeV}$', ATLAS-CONF-2011-008 (2011).

[43] ATLAS Muon Combined Performance Group, 'Pile-up Dependence of the ATLAS Muon Performance', ATL-COM-PHYS-2011-1640 (2011).

[44] ATLAS Collaboration, 'Improved Luminosity Determination in pp Collisions at $\sqrt{s} = 7\,\text{TeV}$ using the ATLAS Detector at the LHC' (2012), arXiv: `1302.4393 [hep-ex]`.

[45] ATLAS W/Z Group, *W/Z and Electroweak Common Topics (2011)*, URL: `https://twiki.cern.ch/twiki/bin/viewauth/AtlasProtected/WZElectroweakCommonTopics2011`.

[46] S. Alioli et al., 'NLO vector-boson production matched with shower in POWHEG', *JHEP* 0807 (2008) 060, DOI: `10.1088/1126-6708/2008/07/060`, arXiv: `0805.4802 [hep-ph]`.

[47] T. Sjöstrand, S. Mrenna and P. Z. Skands, 'PYTHIA 6.4 Physics and Manual', *JHEP* 0605 (2006) 026, DOI: `10.1088/1126-6708/2006/05/026`, arXiv: `hep-ph/0603175`.

[48] A. Sherstnev and R. S. Thorne, 'Parton Distributions for LO Generators', *Eur. Phys. J.* C55 (2008) 553–575, DOI: `10.1140/epjc/s10052-008-0610-x`, arXiv: `0711.2473 [hep-ph]`.

[49] S. Frixione and B. R. Webber, 'Matching NLO QCD computations and parton shower simulations', *JHEP* 0206 (2002) 029, arXiv: `hep-ph/0204244`.

[50] M. Bahr et al., 'Herwig++ Physics and Manual', *Eur.Phys.J.* C58 (2008) 639–707, DOI: `10.1140/epjc/s10052-008-0798-9`, arXiv: `0803.0883 [hep-ph]`.

[51] ATLAS Collaboration, G. Aad et al., 'Measurement of the $W \to \ell\nu$ and $Z/\gamma^* \to \ell\ell$ production cross sections in proton-proton collisions at $\sqrt{s} = 7\,\text{TeV}$ with the ATLAS detector', *JHEP* 1012 (2010) 060, arXiv: `1010.2130 [hep-ex]`.

[52] S. Frixione, P. Nason and B. R. Webber, 'Matching NLO QCD and parton showers in heavy flavour production', *JHEP* 08 (2003) 007, arXiv: `hep-ph/0305252`.

[53] G. Corcella et al., 'HERWIG 6.5: An Event generator for hadron emission reactions with interfering gluons', *JHEP* 0101 (2001) 010, DOI: `10.1088/1126-6708/2001/01/010`, arXiv: `hep-ph/0011363`.

[54] M. L. Mangano et al., 'ALPGEN, a generator for hard multiparton processes in hadronic collisions', *JHEP* 0307 (2003) 001, arXiv: `hep-ph/0206293`.

[55] J. Butterworth et al., 'Single Boson and Diboson Production Cross Sections in pp Collisions at $\sqrt{s} = 7\,\text{TeV}$', ATL-COM-PHYS-2010-695 (2010).

[56] L Di Ciaccio et al., 'A measurement of the transverse momentum distribution of Drell-Yan lepton pairs at $\sqrt{s} = 7\,\text{TeV}$ using the ϕ^* variable with ATLAS.', ATL-COM-PHYS-2012-472 (2012).

[57] K. Melnikov and F. Petriello,
'Electroweak gauge boson production at hadron colliders through O(alpha(s)**2)',
Phys. Rev. D74 (2006) 114017, DOI: `10.1103/PhysRevD.74.114017`,
arXiv: `hep-ph/0609070`.

[58] R. Gavin et al.,
'FEWZ 2.0: A code for hadronic Z production at next-to-next-to-leading order',
Comput.Phys.Commun. 182 (2011) 2388–2403, arXiv: `1011.3540 [hep-ph]`.

[59] P. Golonka and Z. Was,
'PHOTOS Monte Carlo: A Precision tool for QED corrections in Z and W decays',
Eur.Phys.J. C45 (2006) 97–107, arXiv: `hep-ph/0506026`.

[60] ATLAS Collaboration, G. Aad et al., 'The ATLAS Simulation Infrastructure',
Eur. Phys. J. C70 (2010) 823–874, DOI: `10.1140/epjc/s10052-010-1429-9`,
arXiv: `1005.4568 [physics.ins-det]`.

[61] S. Agostinelli et al., 'GEANT4: A Simulation toolkit',
Nucl.Instrum.Meth. A506 (2003) 250–303.

[62] ATLAS Collaboration, 'Dimuon composition in ATLAS at 7 TeV',
ATLAS-CONF-2011-003 (2011).

[63] ATLAS Collaboration, 'Extraction of the prompt muon component in inclusive muons produced at $\sqrt{s} = 7$ TeV', ATLAS-CONF-2010-075 (2010).

[64] V. Blobel, 'Unfolding methods in high-energy physics experiments',
CERN School of Computing: proceedings,
Geneva, Switzerland: European Organization for Nuclear Research, 1984.

[65] G. Cowan, 'A survey of unfolding methods for particle physics',
Advanced statistical techniques in particle physics. Proceedings,
ed. by M. Whalley and L. Lyons,
Durham, UK: Inst. For Particle Physics Phenomenology, 2002 248–257.

[66] B. C. Smith, 'Measurement of the transverse momentum spectrum of W bosons produced at $\sqrt{s} = 7$ TeV using the ATLAS detector',
PhD thesis, Harvard University, 2011.

[67] G. D'Agostini, 'A Multidimensional unfolding method based on Bayes' theorem',
Nucl.Instrum.Meth. A362 (1995) 487–498.

[68] G. D'Agostini, 'Improved iterative Bayesian unfolding' (Oct. 2010),
arXiv: `1010.0632v1 [physics.data-an]`.

[69] T. Adye, 'Unfolding algorithms and tests using RooUnfold' (2011),
arXiv: `1105.1160 [physics.data-an]`.

[70] T. Adye, *RooUnfold: ROOT Unfolding Framework*,
http://hepunx.rl.ac.uk/ adye/software/unfold/RooUnfold.html.

[71] H. Martinez, Private communications, 2013.

[72] ATLAS Collaboration, 'ATLAS Monte Carlo tunes for MC09', ATL-PHYS-PUB-2010-002 (2010).

[73] ATLAS Collaboration, 'ATLAS tunes of PYTHIA 6 and Pythia 8 for MC11', ATL-PHYS-PUB-2011-009 (2011).

[74] R. Gavin et al., 'W Physics at the LHC with FEWZ 2.1' (2012), arXiv: `1201.5896 [hep-ph]`.

[75] A. Banfi et al., 'Predictions for Drell-Yan ϕ^* and Q_T observables at the LHC', *Phys.Lett.* B715 (2012) 152–156, DOI: `10.1016/j.physletb.2012.07.035`, arXiv: `1205.4760 [hep-ph]`.

[76] J. M. Campbell and R. K. Ellis, 'Next-to-leading order corrections to $W + 2$ jet and $Z + 2$ jet production at hadron colliders', *Phys.Rev.* D65 (2002) 113007, DOI: `10.1103/PhysRevD.65.113007`, arXiv: `hep-ph/0202176`.

[77] G. Ladinsky and C. Yuan, 'The Nonperturbative regime in QCD resummation for gauge boson production at hadron colliders', *Phys.Rev.* D50 (1994) 4239, DOI: `10.1103/PhysRevD.50.R4239`, arXiv: `hep-ph/9311341`.

[78] C. Balazs and C. Yuan, 'Soft gluon effects on lepton pairs at hadron colliders', *Phys.Rev.* D56 (1997) 5558–5583, DOI: `10.1103/PhysRevD.56.5558`, arXiv: `hep-ph/9704258`.

[79] F. Landry et al., 'Tevatron Run-1 Z boson data and Collins-Soper-Sterman resummation formalism', *Phys.Rev.* D67 (2003) 073016, DOI: `10.1103/PhysRevD.67.073016`, arXiv: `hep-ph/0212159`.

[80] A. V. Konychev and P. M. Nadolsky, 'Universality of the Collins-Soper-Sterman nonperturbative function in gauge boson production', *Phys.Lett.* B633 (2006) 710–714, DOI: `10.1016/j.physletb.2005.12.063`, arXiv: `hep-ph/0506225`.

[81] ATLAS Collaboration, 'Studies of vector boson transverse momentum simulation in Monte Carlo event generators', ATL-PHYS-PUB-2011-015 (2011).

[82] S. Berge et al., 'Transverse momentum resummation at small x for the Tevatron and CERN LHC', *Phys.Rev.* D72 (2005) 033015, DOI: `10.1103/PhysRevD.72.033015`, arXiv: `hep-ph/0410375`.

[83] P. M. Nadolsky, D. Stump and C. Yuan, 'Phenomenology of multiple parton radiation in semiinclusive deep inelastic scattering', *Phys.Rev.* D64 (2001) 114011, arXiv: `hep-ph/0012261`.

[84] V. Abazov et al., 'Measurement of the shape of the boson transverse momentum distribution in $p\bar{p} \to Z/\gamma^* \to e^+e^- + X$ events produced at $\sqrt{s} = 1.96\,\mathrm{TeV}$', *Phys.Rev.Lett.* 100 (2008) 102002, DOI: `10.1103/PhysRevLett.100.102002`, arXiv: `0712.0803 [hep-ex]`.

Acknowledgements

In the work leading up to this thesis, i have profited from the generous support by many people and i want to take this opportunity to express my gratitude to all of them.

I would like to thank Prof. Norbert Wermes for giving me the opportunity to develop my thesis within ATLAS and to stay at CERN at such an exciting time, as well as for proof-reading the complete draft of this thesis.

I want to thank Dr. Götz Gaycken for following my work closely, for his helpful advice and for answering my countless questions with patience. He also helped to improve the thesis by reading the draft and giving detailed comments.

The $Z \rightarrow \mu^+\mu^-$ analysis for the early ATLAS data and the first Z p_T measurement was developed together with Götz Gaycken, Kristof Schmieden and Jan Therhaag. Thank you for the productive collaboration!

All colleagues from the ATLAS groups in Bonn helped to create a great atmosphere and made the past years an interesting and enjoyable experience. In particular i want to thank Guilherme Hanninger, Nicolas Möser, Lucia Masetti, Marc Lehmacher, Duc Bao Ta, Serena Psoroulas, Simone Zimmermann, Stephan Hageböck, Agnieszka Leyko, Jana Kraus, Dennis Hellmich, Eckhart von Törne, Jürgen Krosebeck, Markus Cristinziani, Vadim Kostzukhin, Thomas Schwindt, Elisabeth Schopf and Ghia Khoriauli.

Most importantly i want to thank Esmeralda and my family who have shown an incredible amount of patience and provided encouragement during this time! Thank you!